Modeling and Manufacturing of Multilayer Laue Lenses for Highest Resolution X-ray Microscopy

Dissertation
zur Erlangung des Doktorgrades
an der Fakultät für Mathematik, Informatik und Naturwissenschaften
Fachbereich Physik
der Universität Hamburg

vorgelegt von
Adam Kubec
aus Prag

Hamburg
2017

Gutachter der Dissertation:	Prof. Dr. Christian Schroer Prof. Dr. Andreas Leson
Zusammensetzung der Prüfungskommission:	Prof. Dr. Daniela Pfannkuche Prof. Dr. Andreas Leson Prof. Dr. Christian Schroer Prof. Dr. Gerhard Grübel Prof. Dr. Andreas Stierle
Vorsitzende der Prüfungskommission:	Prof. Dr. Daniela Pfannkuche
Datum der Disputation:	12.01.2018
Vorsitzender des Fach-Promotionsausschusses PHYSIK:	Prof. Dr. Wolfgang Hansen
Leiter des Fachbereichs PHYSIK:	Prof. Dr. Michael Potthoff
Dekan der Fakultät MIN:	Prof. Dr. Heinrich Graener

Abstract

X-ray microscopy is a technique bridging the gap between optical and electron microscopy. It permits investigations of the structure and composition of various samples with resolutions well below 100 nm. Depending on the sample this is also possible nondestructively and together with the measurement of depth information. The focus of this doctoral project is the development and property calculations of multilayer Laue lenses (MLLs) for highest resolution X-ray measurements. MLLs are diffractive X-ray optics, which are suited for the use with hard X-ray photon energies of more than 5 keV, in particular. MLLs promise high efficiencies as well superior resolutions in this energy range.

MLLs focus X-rays according to the principle of a linear zone plate. Unlike these – generally electron-beam lithography produced – zone plates, the zone structure is formed by many thousands individually deposited thin layers. From this multilayer structure a lens segment is formed. For this purpose the multilayer is structured in order to achieve the desired geometry, which is the actual MLL. These structuring steps can be performed with a wafer saw, laser cutting and focused ion beam milling. One MLL is a one-dimensional diffractive optical element; therefore two similar segments have to be combined for two-dimensional focusing. Knowledge of the results of the individual production steps is required to locate manufacturing faults or existing potential for improvements. For the evaluation of the results scanning electron microscopy and X-ray methods, such as X-ray diffraction, have been used in particular. The intended main use of MLLs is the focusing in synchrotron radiation facilities; therefore measurements at beamlines can also be understood as a final performance test of the manufactured lenses. Focusing experiments were conducted at the synchrotron radiation sources PETRA III (Germany) and ESRF (France). The focusing properties were evaluated in terms of shape and intensity of the beam. Further experiments for measuring diffraction properties were carried out at the Advanced Photon Source (United States).

In order to understand the characteristics of the MLLs, properties of perfect and imperfect MLLs were calculated. This was done with the use of algorithms based mainly on the Beam Propagation Method and the Coupled Wave Theory. The calculation of the properties was made with emphasis on various material systems, the alignment of the lenses and possible manufacturing defects.

The essential steps of manufacturing have been done at the Fraunhofer Institute for Material and Beam Technology IWS. The manufacturing of the MLLs as well as the characterization of their focusing properties was carried out in collaboration with the Institute of Structural Physics of the Technische Universität Dresden, the X-ray nanoscience and X-ray optics group of PETRA III, Fraunhofer IKTS and AXO Dresden GmbH. The evaluation of synchrotron diffraction and part of the calculations were carried out in collaboration with the X-ray optics group of the Advanced Photon Source.

During the work on this thesis a method of measuring the bending of MLLs without a reference sample has been developed. The focal profile of the best manufactured MLLs shows a resolution below 25 nm with the largest efficiency and flux in focus yet achieved using MLLs.

Kurzfassung

Röntgenmikroskopie ist eine vielversprechende Technik, welche die Lücke zwischen optischer und Elektronenmikroskopie schließt. Sie ermöglicht es, Untersuchungen der Struktur und der Zusammensetzung verschiedenartiger Proben mit Auflösungen deutlich unter 100 nm vorzunehmen. Je nach Probenbeschaffenheit ist dies zerstörungsfrei und zusammen mit der Ermittlung von Tiefeninformationen möglich. Der Schwerpunkt des hier beschriebenen Promotionsvorhabens ist der Entwicklung und die Berechnung der Eigenschaften von Multischicht Laue Linsen (MLL) für höchstaufgelöste Röntgenmessungen. Bei MLL handelt sich dabei um diffraktive Röntgenoptiken, welche insbesondere für die Nutzung mit harter Röntgenstrahlung mit einer Energie von mehr als 5 keV geeignet sind und in diesem Bereich höhere Effizienzen sowie gegenüber anderen Röntgenoptiken bessere Auflösungen versprechen. Im Rahmen des Promotionsverfahrens wurden insbesondere die Herstellung, Charakterisierung und Berechnung der Eigenschaften von MLL durchgeführt. Hierbei steht als Ziel die Anwendung von MLL als Fokussierungsoptik für Synchrotronstrahlanwendungen im Vordergrund.

MLL fokussieren Röntgenstrahlen nach dem Prinzip einer linearen Zonenplatte. Im Unterschied zu elektronenstrahllithografisch hergestellten Zonenplatten wird die Zonenstruktur durch eine Multischicht aus vielen tausend Einzelschichten erzeugt. Aus der so hergestellten Multischicht wird anschließend ein Linsensegment geformt, wobei die Beschichtung hierfür zunächst grob und anschließend fein strukturiert wird, um die gewünschte Geometrie zu erreichen. Diese Schritte können mit Laserschneiden und durch Abtrag mit einem fokussierten Ionenstrahl durchgeführt werden. Da es sich bei einer so hergestellten MLL um ein eindimensional beugendes optisches Element handelt, müssen zwei vergleichbar hergestellte Segmente zu einer zweidimensional fokussierenden Optik kombiniert werden. Die Charakterisierung der Ergebnisse der einzelnen Produktionsschritte ist dabei notwendig, um Herstellungsfehler bzw. vorhandenes Verbesserungspotential zu ermitteln; hierbei wurden insbesondere die Rasterelektronenmikroskopie und Röntgenverfahren wie die Röntgendiffraktometrie eingesetzt. Aufgrund der geplanten Anwendung für die Fokussierung von Röntgenstrahlen an Synchrotronstrahleinrichtungen ist der Einsatz als Optik an entsprechenden Strahlrohren auch als finaler Test einer hergestellten Linse zu verstehen. Entsprechende Experimente wurden an den Röntgenstrahlungsquellen PETRA III und ESRF durchgeführt. Hierbei wurden vor allem die Fokussierungseigenschaften in Bezug auf Form und Intensität des mit den Linsen fokussierten Linsenstrahles untersucht. Experimente zur Vermessung der Beugungseigenschaften wurden auch an der Advanced Photon Source durchgeführt.

Um die Eigenschaften der Linsen zu verstehen, wurden die Fokussierungseigenschaften von MLL berechnet. Dies erfolgte unter Nutzung von Algorithmen basierend auf der Coupled Wave Theory und der Beam Propagation Method. Die Berechnung der Eigenschaften erfolgt insbesondere unter den Gesichtspunkten von verschiedenen Materialsystemen, der Einrichtung zur Fokussierung der Linsen und möglichen Herstellungsfehlern.

Die wesentlichen Arbeitsschritte der Herstellung erfolgten am Fraunhofer Institut für Werkstoff und Strahltechnik (IWS) in Dresden. Die Herstellung sowie Charakterisierung der Fokussierungseigenschaften der Linsen erfolgte in Zusammenarbeit mit dem Institut fr̈ Strukturphysik der Technischen Universität Dresden, der X-ray Nanoscience und X-ray Optics Gruppe des PETRA III, dem Fraunhofer IKTS sowie der AXO Dresden GmbH. Die Charakterisierung der Beugungseigenschaften und Teilen der Berechnungen erfolgten in Zusammenarbeit mit der X-ray Optics Group der Advanced Photon Source. Während der Arbeit an diesem Promotionsvorhaben wurde eine Referenzprobenfreie Methode zur Messung der Verbiegung von MLL entwickelt. Aus dem Strahlprofil der besten hergestellten Linse ergibt sich eine Auflösung von besser als 25 nm; diese weist die höchste bisher mit MLL erreichte Effizienz auf und es konnte der bisher größte Fluss mit MLL erreicht werden.

Contents

List of Figures

List of Tables

Acronyms

APS Advanced Photon Source

BNL Brookhaven National Laboratory

BPM Beam Propagation Method

CWT Coupled Wave Theory

EDX Energy Dispersive X-ray Spectroscopy

ESRF European Synchrotron Radiation Facility

FFT Fast Fourier Transform

FIB Focused Ion Beam

FWHM Full Width Half Maximum

FZP Fresnel Zone Plate

LTP Long Term Project

MLL Multilayer Laue Lens

MSD Magnetron Sputter Deposition

MZP Multilayer Zone Plate

OA Optical Axis

OSA Order Sorting Aperture

PCO PCO-4000; OptiquePeter

PETRA Positron-Elektron-Tandem-Ring-Anlage

RESOLFT Reversible Saturable Optical Linear (Fluorescence) Transitions

SEM Scanning Electron Microscopy

STED Stimulated Emission Depletion

STXM Scanning Transmission X-ray Microscopy

XRR X-ray reflectometry

Symbols

$a_{[XX]}$	fitting parameter with XX $\in$ {Si, Mo}
α	angular displacement
A	Amplitude
$b_{[XX]}$	fitting parameter with XX $\in$ {Si, Mo}
β	see refractive index n
$\bar{\beta}$	weighted β
$\Delta\beta$	β difference $\lvert\beta_2 - \beta_1\rvert$
c	Speed of light
d	resolution
dr	zone width
dr_{min}	smallest zone width
dr_{max}	largest zone width
d_{prop}	propagation distance
d_{layer}	deposition thickness
$d_{[XX]}$	single layer thickness, XX $\in$ {Si, $MoSi_2$, Mo}
δ	see refractive index n
$\bar{\delta}$	weighted δ
$\Delta\delta$	δ difference $\lvert\delta_2 - \delta_1\rvert$
ΔD	thickness difference
δ_{pix}	resolution
D	physical aperture; for partial lenses is equivalent to $r_{out} - r_{in}$
ΔD	relative lens distance
E	photon energy
E_s	Youngs Modulus
η / η^2	efficiency / crossed lens efficiency
f	focal length
f_Ω	angular substrate frequency
f_S	substrate spin frequency
g	grating constant
γ	relative angle between to lenses
Γ	ratio absorber material thickness/ period thickness
h_s	substrate thickness
$\hbar$	Planck constant
i	imaginary number
I	Intensity
k	k-factor
kc	deposition rate
λ	wavelength
m	diffraction order
M	number of individual refractive lenses
n	zone number, or
	index of refraction: $n = 1 - \delta + \mathrm{i}\beta$
n_{min}	smallest zone number
n_{max}	largest zone number
NA	numerical aperture
ν	Poisson's ratio
π	Ludolph's constant
r	radius according to zone plate law

r_n	radius of n$^{\text{th}}$ zone
r_{in}	inner radius according to zone plate law
r_{out}	outer radius according to zone plate law
Δs	path difference for focusing
σ	residual stress
t	section thickness
t_{opt}	optimum section thickness
θ	diffraction angle
Θ	refraction angle
Θ_C	critical angle
Φ	phase difference for focusing
k	wavenumber $= \frac{2\pi}{\lambda}$
R	curvature radius of refractive lens
R_0 / R_1	measured curvature radii of before / after the deposition
w	gaussian beam size
w_0	beam waist
wd	working distance; distance from OSA entrance to focal plane
x	calculation position along the radius of the lens
z	propagation position along OA
z_0	focus position along OA
z_R	Rayleigh length

1 Introduction

Optical systems capable of capture far flung and tiny objects likewise, which cannot by the naked eye have fascinated people for a long time. They have changed the course of how mankind thinks about and understands the scale and size of the universe, as well as objects such as viruses, bacteria or the composition of materials. Optical telescopes are widely in use since they became popular as Galileo Galilei discovered four moons of the planet Saturn, which led to scientific discussions and finally led to a changed world view from geocentric to heliocentric [GB65]. Philosophical discussion about atoms – originaly considered as not dividable parts of matter – have already been present in ancient times [Ber08]. Today we are able to *see* and detect smallest particles and largely understand how matter forms.
Although much more complex instruments and methods exists today this path started with optical microscopy (from greek μικρός = small and from greek σκοπεῖν = view [EP02]). Some of the first telescopes have been said to be built by Zacharias Janssen in the early 17th century [The17]. Ernst Abbe developed the diffraction limited lenses in the end of the 19th century. Resolution of the optical systems has been limited by the aberrations caused by the imperfect production methods for light microscopy lenses. Abbe found, that the general resolution with optical systems is around 200 nm for visible light due to the diffraction limit, which can be expressed as a function of the the wavelength of light used [Abb73]:

$$d = \frac{\lambda}{2\ \mathrm{NA}} \tag{1.1}$$

with d as the maximum resolution, λ as the wavelength and NA as the numerical aperture of the system. The resolution has been surpassed by various methods with so called Reversible Saturable Optical Linear (Fluorescence) Transitions (RESOLFT) techniques. These feature a resolution beyond the diffraction barrier for specific applications and have started to been developed in the late 20$^{\text{th}}$ century [HW94]. Stimulated Emission Depletion (STED) microscopy for example allows to achieve resolutions more than one order of magnitude beyond what Abbes limit would allow and is a widely used technique in science. It has been awarded by a nobel prize in chemistry in 2014 [Nob14]. This technique however does not allow for a general microscopy resolution beyond the Abbe limit. It has limitations as of which configurations can be imaged. Therfore classical microscopy setups and their improvement remain a current topic of instrumentation development.
Microscopy comprises mainly two methods in general: full field microscopy and focusing or scanning microscopy. *Classical* full field microscopy allows to obtain information such as absorption contrast or phase contrast for a certain area of a sample and allows for real time measurements. In scanning microscopy the sample is located in the focal spot of a focusing

lens upstream of the sample. In full field microscopy an objective lens has to be downstream of the sample. In other words in scanning microscopy the light source is imaged onto the sample while in full field microscopy the sample is imaged on a screen. Examples for both techniques are shown in Figure 1.1.

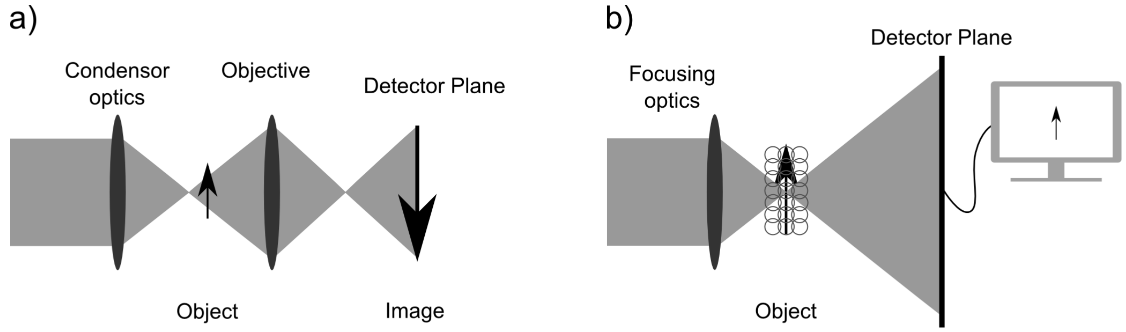

Figure 1.1: Scheme of a) Full field imaging and b) scanning transmission microscopy.

According to the Abbe limit shorter wavelengths of light are necessary to push the diffraction barrier to higher resolutions. After the wave-particle dualism has been described the use of electrons instead of photons was considered for microscopy purposes. Transmission electron microscopy (TEM) and scanning electron microscopy (SEM) have been developed based on this idea and are still widely used for high resolution material analyses.

Also other types of microscopy method exist, which are based on significantly different principles; atomic force microscopy and Kerr microscopy for example can be used to shed light on roughness and magnetization states, respectively [BQG86, ZKK97].

When Wilhelm Conrad Röntgen first discovered X-rays he did not see any refraction when they passed material boundaries. He assumed it would not be possible to focus the rays at all [Rön98]. This would imply, that no microscopy would be possible due to the lack of available lenses.

Indeed the prerequisites for refractive lenses are very different for X-rays as compared to visible light. Due to the very small refraction for nearly all materials as compared to visible light only a very small change in the light propagation direction can be expected.

A first step towards X-ray microscopy has been achieved by total reflection mirrors [KB48]; roughly at the same time Fresnel zone plates for X-rays have been discussed [MJ51], while their general principle then been known for some time [Fre96]. Finally in the late 20th century refractive X-ray lenses have been successfully developed [SKSL96]. However it is necessary to string together several lenses to achieve a sufficient refraction.

For electromagnetic waves the relationship between the wavelength λ and the photon energy E is calculated by $\lambda = \hbar c/E$. Each range of energies (see Figure 1.2) in the electromagnetic spectrum can be used for different techniques.

X-rays allow for energy and element dependent contrast. Due to their large energy they can induce atomic fluorescence, which makes them very suitable for the elemental mapping of materials and other applications. In X-ray microscopy a differentiation can be made by dividing it into soft X-ray microscopy and hard X-ray microscopy. Soft X-ray microscopy is

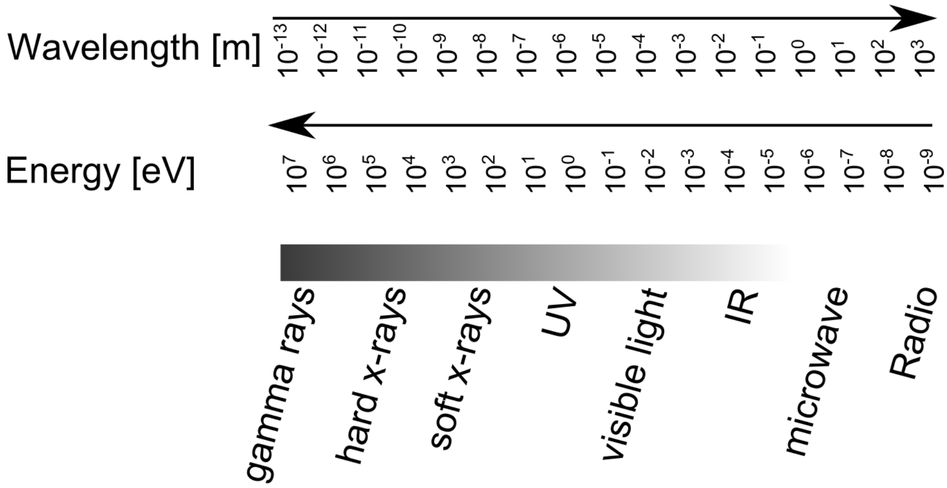

Figure 1.2: Electromagnetic spectrum of light.

partly aiming into the energy range of the so called water window ($\approx 280 - 530\,\text{eV}$). This is the range in the electromagnetic spectrum, for which the contrast of carbon and oxygen is very large and allows to differentiate between water and carbon, i.e., biological materials, in particular.

X-rays with shorter wavelengths and energies above 5 keV can be considered as hard X-rays [Att07]. Many experiments are performed at energies between 8 keV and 25 keV depending on the type of X-ray source used. Hard X-rays are used to probe samples composed of more heavy elements.

Two ideal and important examples of applications are batteries and microprocessors. The demand of energy, distributed electricity generation and energy storage is currently a major topic in Germany as well as worldwide in the scope of the energy transition (German: *Energiewende* [Bun17]). Batteries in particular will play a large role for several aspects of this process, such as mobile energy storage and in particular for electromobility. Mobile energy storage is necessary in order to power cars and other types of vehicles, which are relevant for individual and mass transportation and batteries are currently the most prominent candidate for energy storage in electric cars. It is expected, that some types of batteries can be improved to suffer a lower capacity loss over time and feature a higher energy density. Also new types of batteries could be made available or significantly improved beyond existing types in some aspects with a better understanding of the internal processes [BDN+00].

The development of microprocessors on the other hand for a long time was well described and by now is driven by what is called Moore's Law [Moo06]. A lot of effort is put in the development and improvement of new manufacturing techniques, of which EUV lithography is currently a major part in order to allow to stack more individual transistors in a smaller volume [WH10]. This allows to increase the available computation power significantly. It also allows for a reduction of the required amount of energy for the same tasks over time compared to recent versions of microchips.

These developments require adequate probing methods. X-ray methods allow for a nondestructive testing of individual samples in e.g., a transmission geometry and also can give

information about burried features. Therefore this technique is most suited for properties, which cannot be examined by electron microscopy methods, which usually require very thin samples or can only provide information about the surface.
Best "direct" imaging X-ray methods today achieve resolutions in the range of 10 nm while advanced methods allow even better resolutions. A photon energy of 12 keV corresponds to a wavelength of 0.103 nm, which would allow resolution according to Abbe significantly below 1 nm. While electron microscopy methods such as SEM and EDX allow for higher resolutions, they are are limited to probe surface and near surface properties only.
The limiting factor in order to achieve near wavelength resolution with X-ray microscopy is currently the available numerical aperture of available lenses paired with their quality in terms of aberrations. Large numerical apertures can be obtained with lenses featuring short focal lengths. However a sufficient working distance is desired in order to allow the measurement of several types of samples and methods.
An established type of X-ray optics is the Fresnel zone plate. It is based on the principle of diffraction through a grating. The structure is, however, adapted to allow for focusing. This is achieved by changing the angle of diffraction continuously, so that the resulting diffraction is pointed towards a single point on the optical axis. Figure 1.3 shows a scheme of such a structure.

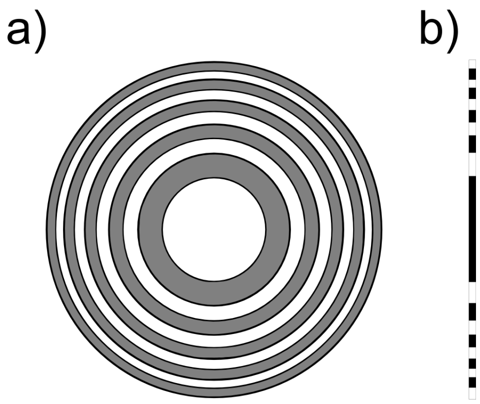

Figure 1.3: a) General zone plate structure made up of concentric rings around the optical axis
b) Side view of a zone plate structure.

The achievable resolution is limited by the numerical aperture. For a given focal length this can be improved by adding further structures on the outerlying edges. The width of the structures (i.e. of the individual zones) is decreasing with the distance to the optical axis. This type of optics has been fabricated mainly using techniques based on electron-beam lithography. Electron-beam lithography has shown to be able to produce structure sizes in the order of down to 10 nm. However, the manufacturing of significantly smaller structures is not possible without further ado. Additionally the aspect ratios are limited by the stability of such a structure; currently aspect ratios in the range of 1 : 30 have been achieved by lithographic techniques [VCGF+11]. However for an effective diffraction a larger aspect ratio might be desired in order to achieve relevant efficiencies. Especially for hard

X-rays the efficiency of the structures might be limited and therefore it would be desirable to manufacture structures with smaller zone widths larger apertures and yet larger optical depths as shown in Figure 1.4. A method to achieve such structures is thin film deposition which forms the individual zones. This has been first proposed in the early 1980s to be made on wire type substrates [RS80, RNS82]. This type of X-ray optics is called Multilayer Zone Plate (MZP) and has a circular structure similar to Fresnel zone plates. If these structures are made on flat substrates the resulting structure is called MLL (multilayer Laue lens) and offers a structure similar to linear Fresnel zone plates [KTK84]. These types of optics have been considered to achieve focal spot sizes in the region below 1 nm and high focusing efficiencies at the same time [SKP+05, YMM+07].

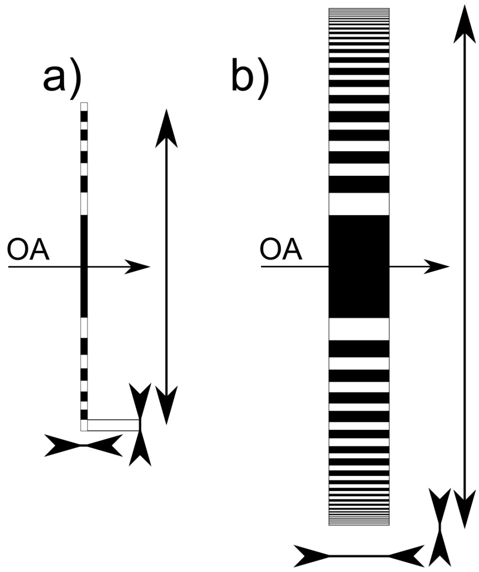

Figure 1.4: a) Standard zone plate structure side view.
b) Improved zone plate structure with a larger section thickness t and additional zones with a smaller width dr_{min} leading to a larger physical aperture D.

This thesis targets the development and improvement of MLLs at the Fraunhofer IWS in Dresden. The goal was to bring these optics to a stage of development, where they can be used at synchrotron beamlines for user experiments. Therefore, it was necessary to give a user the best possible resolutions on the one hand connected with a justifiable effort in terms of sample alignment and enviroment preparation on the other hand. In particular this is connected to working distances in the order of several millimeters.

This allows experiments with bulky sample environments with an unprecedented high resolution. First users at the ESRF beamline ID13 have already used the MLLs made within the scope of this thesis with an indentation device and further experiments with different sample environments are planned.

2 Hard X-ray optics and theoretical background

The manufacturing and understanding of focusing optics requires several basic concepts. Of particular interest is the general concept of how focusing in general is achieved. The part of the electromagnetic spectrum, which is taken into account in this thesis is the hard X-ray range. As the electromagnetic spectrum ranges from the lowest possible energies of radiofrequency waves, over infrared and visible light to X-rays and gamma rays, it has to be defined, which part is taken into account. There is no single definition for so called hard X-rays especially in terms of the comparison with soft X-rays. While the water window with energies between 282 eV and 533 eV is almost always considered as the part of the soft X-ray range the transition to hard X-rays is less clearly defined. In this thesis hard X-rays will be assumed to start at an energy of 5 keV. Although even higher energies can be used the main emphasis of this thesis is laid in the of photon energies of 5 keV and 25 keV; many experiments are designed to be done in this range.
In this section the generally observable interaction of hard X-rays with matter will be discussed and subsequently the use of these effects will be discussed in the context of the respective optical elements with emphasis on MLLs.

2.1 X-ray interaction with matter

Generally there are several general effects of interactions of X-rays with matter, which affect the propagation of X-rays:

- Refraction
- Diffraction
- Reflection

Refraction

One of the properties which plays a major role for the properties and the type and intensity of interaction of matter is the atomic scattering factor of a material [HGD93]. From the scattering factors the complex index of refraction of a material can be calculated, which is well-known to describe refraction in a material or within a transition between different volumes filled with different materials as well as attenuation within matter. For photon energies in the X-ray range the index of refraction n is usually characterized using δ and β for the equation [Att07]:

$$n = 1 - \delta + \mathrm{i}\beta \tag{2.1}$$

Typical values for δ and β range between 10^{-4} to 10^{-8} for the hard X-ray regime. δ is a merit for the phase shift in the material:

$$\Delta\Phi(z) = \Phi(z) - \Phi(0) = \frac{2\pi\delta}{\lambda} z \tag{2.2}$$

β is a decay parameter, which is used in Beer-Lambert's law:

$$I(z) = I_0 \exp\left(-\frac{4\pi\beta}{\lambda} z\right) \tag{2.3}$$

In Figure 2.1 a) and b) δ and β are shown for tungsten, molybdenum, carbon and silicon for photon energies from 5 keV to 25 keV. These materials have been considered for the mentioned energies in the scope of this thesis. The *steps* in β represent an absorption edge for that material at that specific energy.

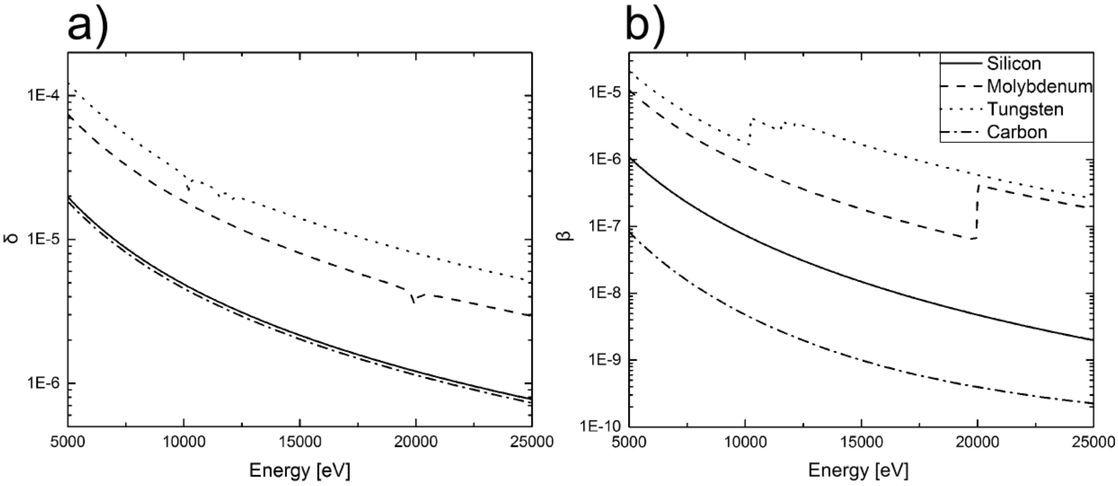

Figure 2.1: δ and β for tungsten, molybdenum, carbon and silicon for photon energies between 5 keV and 25 keV [hen17].

In comparison to X-rays, for which the real part of the refractive index is smaller than unity, it is larger than unity for visible light. For visible light usually the absolute number of the real part of the refractive index is given (e.g. $n \approx 1.5$ for glass). Using the refractive indices of two materials n_1 and n_2 in Snell's law allows to calculate the change in direction of between the angle of incidence Θ_1 to the angle of refraction Θ_2 in the second material:

$$\frac{n_1}{n_2} = \frac{\sin\Theta_2}{\sin\Theta_1} \tag{2.4}$$

Both angles are given with respect to the normal vector of the surface.
For an incoming ray of visible light from vacuum into material at an angle of 5° this results in a change of the direction of the beam to an angle of 3.3°. For X-rays the same incoming angle

results in an exit angle of 5.00002°. A scheme of visible light and X-ray refraction is shown in Figure 2.2 a) and b) respectively. Note that the direction of the change has switched sign as the index is smaller than unity for X-rays as compared to visible light. The small deviation from the original direction was the reason for the original assumption, that no lenses can be made for X-rays [Rön98].

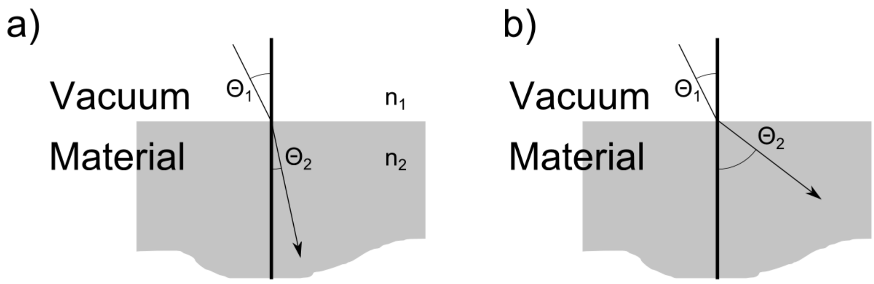

Figure 2.2: Refraction at vacuum/material surface for a) visible light and b) X-rays.

2.2 Total external reflection

Total reflection is a special case of refraction. As the real part $\mathrm{Re}(n) < 1$ for X-rays total external reflection occurs as compared to total internal reflection for visible light. It is achieved with grazing incident beams transiting from an optically thicker to an optically thinner medium; it is achieved when the incoming grazing incidence angle is smaller than the respective critical angle for the interface in question. The critical incident angle can be calculated with Snell's law:

$$\Theta_c = \arcsin\left(\frac{n_2}{n_1}\right) \tag{2.5}$$

2.3 Diffraction at a grating

Refraction does describe a situation well, when light is assumed to propagate as a ray. However, there are situations, which cannot be depicted by refraction and for which a different approach has to be chosen. The Huygens-Fresnel principle is a description of the wave propagation; a wave field is describes in a way, that every part of a wave is the origin of a new spherical wave and at every point in space the waves interfere with each other. The result can be either constructive or destructive interference. A simple structure to visualize this principle is a grating.

The simplest example is a grating which consists of transparent and opaque parts of the grating alike as shown in Figure 2.3. The incoming wave field is diffracted and split up into several diffraction orders with different angles. The behavior after passing the slits can be explained by the wave theory of light. Constructive interference is achieved in a direction where the path differences of the transmitted parts is a integer multiple of the wavelength. The grating equation gives the angles of constructive interference [Att07]:

$$\sin \Theta_m = \frac{m\lambda}{d} \qquad m \in \mathbb{Z} \tag{2.6}$$

The grating is thus a primitive monochromator: the angle of diffraction differs for every wavelength. However, it does not suppress any wavelengths by its design. The expected diffraction efficiency depends on the specific properties of the grating such as the relative width of transmissive and opaque zones, the materials used and the order of diffraction.

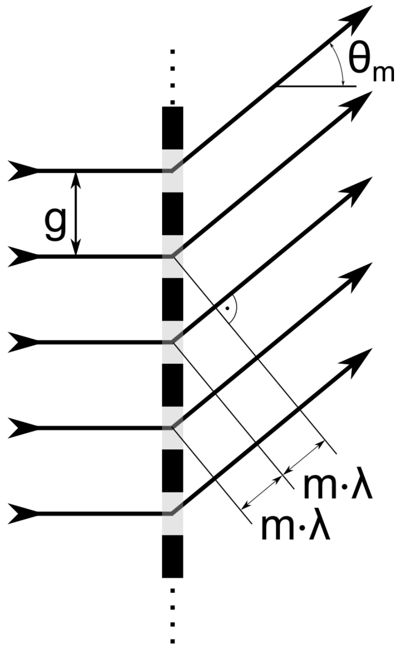

Figure 2.3: Diffraction at a grating into the m^{th} diffraction order. The path difference between waves of neighboring transparent zones is a multiple of the wavelength.

The resulting wave field for a particular diffraction order for a flat incoming monochromatic beam behind the grating does not diverge or converge and thus is again a flat field with (depending on the order) a different angle of propagation.

2.4 Nanoimaging X-ray optics

Focusing X-ray optics are being used to produce a volume of concentrated intensity with small dimensions: the focal spot. However due to the small phase shift and the relatively high absorption it remains challenging making X-ray optics with a large numerical aperture. First types of focusing optics for X-rays have been developed based on the reflection and diffraction; these types have already been manufactured in the middle of the 20^{th} century [KB48, MJ51]. Refractive lenses have emerged starting not earlier than in the 1990s due to the challenges which have had been identified already by Wilhelm Conrad Röntgen. In general, focusing can be achieved by using the concepts, discussed in section 2.1:

- Refraction by refractive lenses
- Reflection by Kirkpatrick-Baez (KB) mirrors, waveguides, capillaries
- Diffraction using gratings, FZPs, MLLs

While this list is not exhaustive, it represents some of the most widely used optics for the focusing of synchrotron radiation. Micro- or nanofocusing beamlines at synchrotron radiation sources are widespread and can use different kinds of optics; each having distinct advantages and disadvantages. Some of the most relevant optics are discussed in this section.
However, first it is necessary to establish the general principle of focusing optics. Regardless of the actual shape or the working principle of a specific type of lens a general prerequisite has to be met. All optics aim to define one point in the focal distance f from the optics to which all or most of the incoming light has to converge after passing the respective optical element. Therefore, it is necessary to modify the incoming light in a way, that the direction of every part ray of light behind the lens is pointing towards one single coordinate – the focal point.
This property can be achieved by modyfing the phase as shown in Figure 2.4 a) corresponding to the "virtual" additional path difference Δs [Att07]:

$$\Delta s(r) = f\left(\sqrt{1+\left(\frac{r}{f}\right)^2}-1\right) \tag{2.7}$$

off which the phase shift function is calculated:

$$\Phi(r) = -k\Delta s(r) \tag{2.8}$$

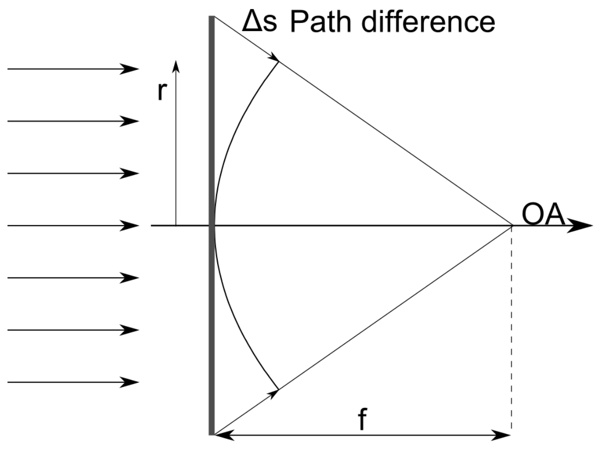

Figure 2.4: General calculation of the path and phase difference for focusing.

Differences from this ideal phase function will lead to aberrations and a distorted focus, which has been calculated and/or measured for various optics [SM83, AKB15, PKH+17, SSS+17, DSPY+17].

Refractive Lenses

Refractive lenses are known from everyday use in the form of eyeglasses for example. However, for X-ray photon energies the refractive power of such a lens would be rather small. While glass has a refractive index of $n \approx 1.5$ at visible light frequencies it has a refractive index of $n \approx 0.99998$ at 5 keV. The effect can be illustrated by calculating the focal length f of a lens with a specific radius for X-rays and visible light. Using

$$f = \frac{R}{2\delta} \tag{2.9}$$

the focal length can be calculated [Hec09]. For visible light a convex glass lens with a radius of 10 cm would result in a focal length $f = 10\,\text{cm}$. A concave lens with the same radius would have a focal length $f \approx 2.5\,\text{km}$ at 5 keV photon energy. A radius of 50 µm still results in a focal length of 12.5 m. Initially, it seemed unfeasible to build a refractive lens for X-rays. Different approaches have been chosen for focusing and imaging optics for X-rays.
Only about one century after the first experiments by Röntgen a diffractive lens was developed [SKSL96]. The idea was to make an arranged stack of individual lenses, which the X-rays would pass through consecutively. Every lens would refract the incoming beam to a larger angle. At first such lenses were made from an aluminum block, where cylindrical holes were drilled into to obtain a set of individual refractive lenses, which together would act as a single line focusing element. Such a lens is called a compound refractive lens (CRL) and the focal length f of such a lens can be calculated using:

$$f = \frac{R}{2M\delta} \tag{2.10}$$

with M as the number of individual lenses. In Figure 2.5 a), b) and c) the shape of refractive lenses for visible light as well as for X-rays is shown. Refractive X-ray lenses are required to have a concave shape compared to a convex shape for visible light. Since the first publication several types and improvements of refractive lenses have been developed including individual stackable CRLs, nanofocusing lenses made by deep reactive ion etching in a silicon substrate, adiabatically focusing lenses, which achieve unprecedented angles of focusing by a gradual adaption of the numerical aperture, refractive lamellar lenses using layers deposited by atomic layer deposition and Fresnel type refractive lenses [VWB+11, SKP+05, APS+16, PKH+17, SSS+17].

Total external reflection optics

Total reflection optics rely on the reflection off their surfaces, which are oriented along the beam propagation direction. Several types of total reflection optics are in use.
Some of the most commonly used optics in this field are Kirkpatrik-Baez mirrors (KB mirrors) and capillary optics. KB mirrors are mainly used in synchrotron radiation facilities and they are large parabolically or elliptically shaped mirrors. One mirror focuses only in one direction, so two of them have to be aligned in a crossed geometry to obtain a point focus. The manufacturing is challenging especially due to the required contour precision over a

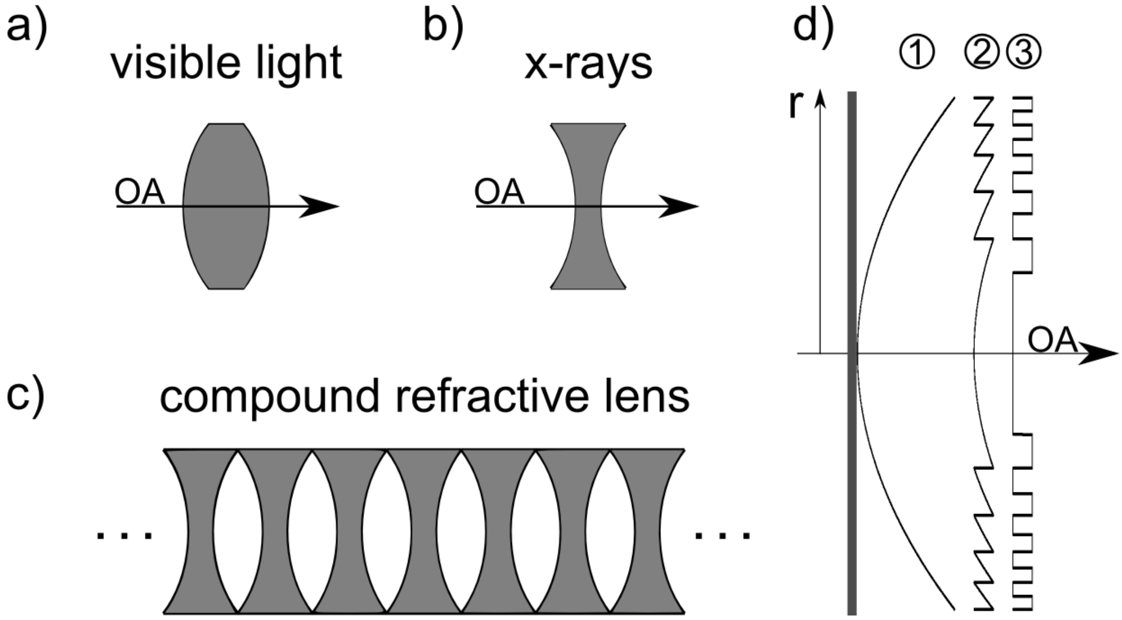

Figure 2.5: Shape of refractive lenses for a) visible light and b) X-rays. Part c) shows the setup of several stacked lenses to achieve a sufficient refraction. d) Phase difference (1) coming from a refractive lens, (2) from a refractive Fresnel lens and (3) the approximation by a zone based structure.

significant length of the mirror.
An application example for Kirkpatrick-Baez mirrors is the use for the focusing of X-rays of a free-electron laser [YMK+13]. A significant advantage of total reflection optics is the achromaticity which makes them suitable for use with a non-monochromatic beam.

Diffractive reflection optics

In comparison to total reflection optics diffractive reflection optics make use of a multilayer or a crystal structure and have a larger numerical aperture for the same length of the mirror due to their larger angular acceptance. The description can be made best using the wave image: an incoming beam will invoke constructive interference, if the path difference to the next reflective (multilayer or lattice) and back to the surface is a multiple of the wavelength. This is classical Bragg reflection, which occurs in periodic structures with corresponding lattice parameters.
The Bragg equation gives the angle θ at which Bragg reflection occurs as a function of the wavelength, the lattice parameter and the material parameters [Att07]:

$$m\lambda = 2g\sin^2\theta - 2\bar{\delta} \tag{2.11}$$

with $\bar{\delta}$ being the weighted δ of the multilayer materials if applicable. The Bragg reflection at a set of interfaces is visualized in Figure 2.6; in this case the Bragg equation is reduced to:

$$m\lambda = 2g\sin^2\theta. \tag{2.12}$$

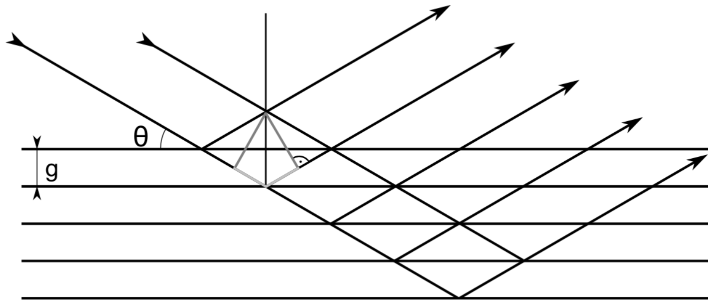

Figure 2.6: Scheme of Bragg reflection at a set of planes.

Different shapes of these mirrors are in use for several purposes. An example is the Göbel mirror [HDMB00]. Through its geometry which has to be as close as possible to a set of confocal plane-parabolic interfaces it can parallelize light coming from a point or line source. These mirrors are widely used in diffractometers and other laboratory machines.
In general diffractive optics are monochromatizing elements. Reflection optics based on crystals are installed at many synchrotron beamlines for this particular use case. A recent notable result for focusing hard X-ray can be found in [DSPY$^+$17].
A focal spot size in one dimension of 7 nm has been achieved by a deformable multilayer mirror using a correction system adapting the shape of the mirror [MHK$^+$10].

Diffractive Transmission Lenses

In this section a general introduction into transmission diffractive optics including FZP and MLLs is given. Basic working principles, differences between FZP an MLL as well as the design process will be discussed.
In a first step the focusing properties of these optics have to be established. Starting from the focal spot the phase function of the lens can be described based on the general definition for focusing from section 2.4. The phase function can be approximated by using to different materials with specific widths. The areas defined by both types of materials are called *zones* and the path difference from the focal point to the boundary has to be equal to half a wavelength of the light or π in phase terms. Figure 2.5 d) shows the necessary optical path difference, the approximation using a Fresnel type refractive lens [Yan93] and using zones of two materials with a distinct optical properties.
Geometrically this can be expressed using the the zone plate law [Att07]:

$$r_n = \sqrt{n\lambda f + \frac{n^2\lambda^2}{4}} \tag{2.13}$$

According to the zone plate law the zone interfaces have to be placed in a specific distance r_n from the optical axis. The zone plate law does, however, not specify the geometry in the third dimension. *Classic* FZP consist of concentric rings around the optical axis. For linear zone plates the optical axis is not a line but a plane instead. Figure 2.7 a) and b) show diffractive optics made of concentric rings and linear zones, respectively. Linear zone plates with zones formed by a multilayer structure are called MLL.

Most properties are the same or similar for concentric and linear zone plates. If properties are not distinguished from here on, they are assumed to be similar for both geometries. For focal lengths significantly larger than the aperture the zone plate law can be approximated to:

$$r_n = \sqrt{n\lambda f} \tag{2.14}$$

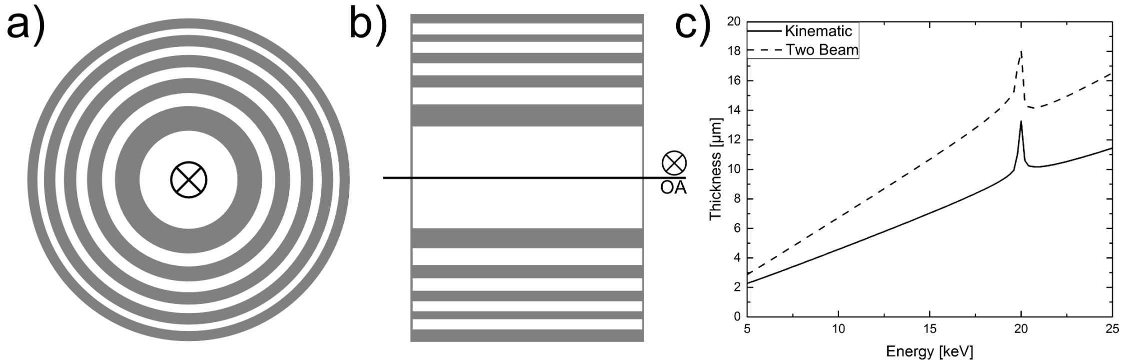

Figure 2.7: a) Concentric and b) linear zone plates with optical axis and optical "plane", respectively.
c) Optimal phase shift thickness and dynamical diffraction thickness for the material combination Mo/Si.

Similar to a diffraction grating several orders are present amongst which the intensity is split. The order of interested is the one, which corresponds to the focusing properties, which have been defined to make the zone plate; this is the first focused order.
Usually only the first three to four orders have relevant intensities for practical purposes and the geometry of the first two is shown in Figure 2.8. Orders can be *constructed* using geometrical optics by the outer limits of the aperture and the designated focal spots. The focal distance changes with the diffraction order m with the factor $1/m$; for negative defocused orders a virtual focal spot on the upstream side of the lens is present.
In the initial approach the two materials are assumed to be fully transparent and opaque, respectively, and have a very small thickness in the beam propagation direction. However, real materials are neither fully transparent nor fully opaque but rather transparent to a certain degree and also phase shifting. The absorption and phase shift depends on the material itself but also on the wavelength of the light.
According to the difference of refractive indexes of the two materials the optimal thickness t_{opt} in order to achieve the desired phase shift π can be calculated if the relative phase shift $\Delta\delta$ is considered [Sch11]:

$$t_{opt} = \frac{\lambda}{2\Delta\delta} \tag{2.15}$$

However, this is only valid for a geometrical (also known as kinematic) regime, which can be considered relevant for large zone widths. For small zone widths a transition is made towards the dynamical diffraction regime, where diffraction properties cannot be described geometricall anymore; this is also known as the dynamical diffraction regime. The two-beam

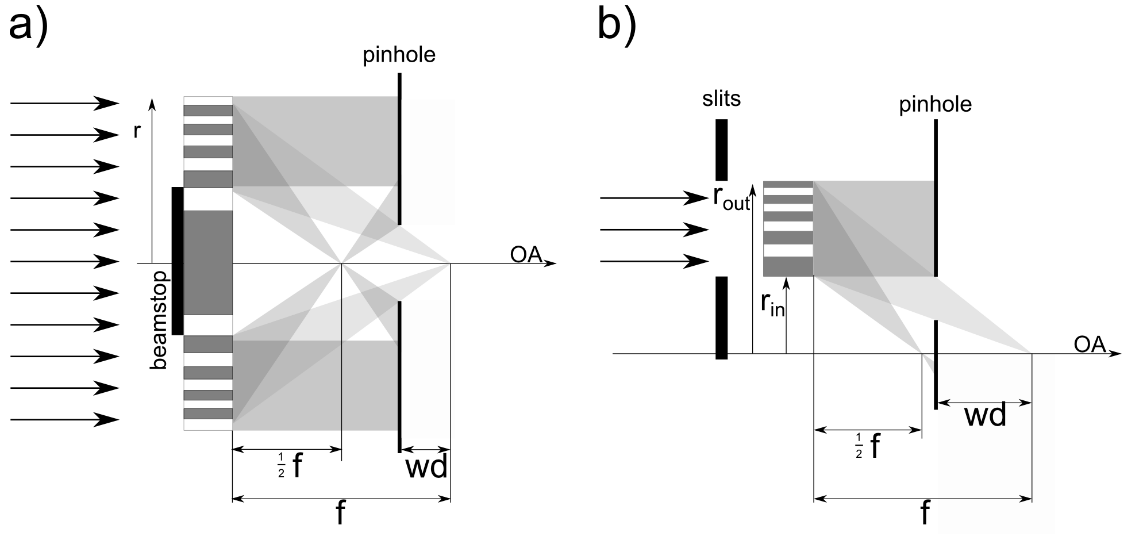

Figure 2.8: Multiple focusing diffraction orders for a) a FZP geometry with beam stop and b) a linear zone plate/MLL with slits.

approximation allows to estimate the efficiency of a two material system if the complex index of refraction is known for both materials for the dynamical diffraction case. The efficiency can be calculated using a single equation [KSL+05]:

$$\eta = \exp\left(-\frac{2k\bar{\beta}t}{\lambda}\right)\sin^2\left(kt\Delta\delta/2\right)\sinh^2\left(kt\Delta\beta/2\right) \tag{2.16}$$

This will give larger necessary values for the optimal thickness t_{opt}. For transmission diffraction optics this is considered valid for zone widths smaller than about 10 nm [Mas94, Mas17, KSL+04]. For a combination of the materials Mo/Si the thicknesses to achieve the optimal phase shift and the optimal dynamical diffraction is shown in Figure 2.7 c).

Further approaches in the field of diffractive transmission optics exist, in particular so called photon sieves have been discussed [KSJ+01]. This is a structure consisting of pinholes of different sizes arranged in a similar manner as a zone plate. They have been proposed for X-rays in the 2000s but have since been in focus in other field such as laser applications or UV light [ZXHW15].

Comparison of the manufacturing of MLLs and FZPs

Thin film deposition and electron-beam lithography are used for the making of MLLs and FZP, respectively. Both techniques have limits, advantages and disadvantages relevant for the focusing properties of diffractive transmission optics.

Lithography and thin film deposition for transmission diffractive optics have different geometrical approaches and implications to the results. Also, the achievable resolution depends on the smallest possible structures perpendicular to the optical axis, that can be formed by the respective technique. For electron-beam lithography this is given by the size of the narrowest possible structure. Additionally, the aspect ratio is defined by the ratio of the smallest zone width and the thickness of the material parallel to the optical axis.

The spatial zone placement error accuracy mainly depends on the positioning accuracy of the electron beam. Locally zone boundaries might be shifted slightly as compared to the design so the width of the zones and thus the absorber/spacer ratio might vary locally. However, globally the accuracy proved to be fairly high to resemble the zone plate geometry [SM83]. With lithographic techniques the smallest manufactured structures are currently in the range of 10 nm which limits the resolution of the resulting lens accordingly. To improve the smallest possible structure size so called zone-doubled zone plates can be manufactured [VCJR+09]. In this case a regular zone plate is manufactured and additionally a thin film layer using atomic layer deposition on top of the existing structures is deposited. This allows achieving smaller effective zone widths [VCGF+11]. For electron-beam lithography it has been shown, that aspect ratios of up to $\approx 1:30$ can be achieved currently [VCGF+11]. One of the limiting factors is the stability of the construction. Transparent and more phase shifting zones are comprised of air and a solid material, respectively. Air does not support the structure and thus the individual zones made of the material might collapse. This behavior has been observed for high resolution test patterns [KBN+14a]. To improve the aspect ratio a stacked zone plate approach has been developed: several zone plates are brought in close adjacency or are directly bonded in order to resemble a larger material thickness; with this technique it is also possible to obtain a curved-like structure [GWL+14, WRGS14]. However, this approach currently seems to be limited to only a few stacked FZPs.
For MLLs made by thin film deposition the precision of neighbouring layers is expected to be very accurate: the deposition of precise 1 nm thick individual layers has been shown [BMM+02]. However, due to the consecutive build-up of the layers even a small deviation of the deposited thicknesses will be accumulated throughout the deposition process. For solely thin film made transmission diffractive optics the thinnest layer limits the achievable resolution in a similar manner as for FZPs.
The stability of individual zones is not a limiting criterion due to the monolithic nature of an MLL. Thus, very high aspect ratios are possible. It can be chosen nearly arbitrarily according to the needs of the respective material combination and photon energy. Especially for energies in the hard X-ray regime above 5 keV these dimensions exceed what can be manufactured using electron-beam lithography. For every material combination and photon energy used there is an optimal section thickness for the lens structure. The section thickness is defined by the sectioning process, which has to be done separately for MLLs.
One MLL made from a deposition on a flat substrate is focusing one-dimensionally as its zone structure is developed only in one dimension in comparison to an FZP as shown in Figure 2.7. This can be advantageous for certain measurements [NBG+18] but many methods and samples require a point focusing device for optimal results. This makes it necessary to align two MLLs in order to form a point focus. Two degrees of freedom are necessary: In a first step it is necessary to ensure to obtain a common focal plane for both lenses. Second the relative perpendicular alignment is necessary to uncouple horizontal and vertical focusing directions. The tolerable angular misalignment is discussed in section 3.5. The combination of two MLLs for point focusing will be called *crossed* geometry.

The use of two crossed MLLs results in a lower focusing efficiency compared to a single lens due to the doubled diffraction process into the desired diffraction order.

General dimensions and terms of an MLL

In literature several sets of terms have been used in order to describe dimensions, directions and sizes connected to MLLs. Therefore, in the following definitions are given, which terms are used in this thesis in order to depict an MLL. Figure 2.9 a) shows the scheme of an MLL bar with a deposition on a substrate and an MLL lamella in the center and Figure 2.9 b) shows the notation of two crossed lenses.

The *deposition thickness* is the sum of the thicknesses of all deposited layers. It is usually in the range of 20 µm to 100 µm. The dimensions of the lamella along the optical axis is called the *section thickness*. The dimension perpendicular to the optical axis parallel to the layer interfaces is called *width* of the lens.

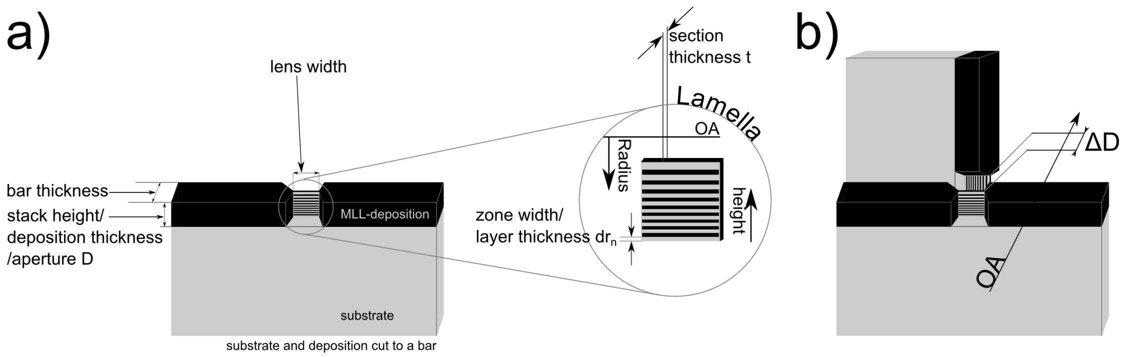

Figure 2.9: General dimensions and notations on and of a) a single MLL b) crossed MLLs.

Generally speaking *individual layer thicknesses* correspond to the zone widths of a zone plate. In case of a design incorporating different absorber/spacer-ratios or more than two materials, one *period* of the multilayer stack corresponds to two zones according to the zone plate law. These cases are discussed in sections 3.8 and 4.1.

Transmissive Diffraction Lens Geometry

Several types of MLLs and diffractive lenses in general can be categorized as different geometries along the radius or along the optical axis. The first distinction is necessary between full, half and partial MLLs. These types with the same aperture D are shown in a scheme in Figure 2.10. Due to their very similar numerical aperture these lenses would have a vers similar focal spot size. Starting with the zone plate structure the zones are located on both sides of the optical axis; this is known as a *full* lens. For a lithographic process this does not impose any significant fabrication challenges; for thin film deposition processes, however, the total thickness of the deposition as well as the thickness variation are critical parameters. Therefore, MLL deposition have usually been manufactured with zones only on one side of the optical axis. If all zone numbers including the first one are present this is called *half* lens. Most MLL depositions have been made manufactured with an innermost zone number significantly larger than 1. The result is an off-axis lens and is known as *partial* geometry lens; it has several advantages as compared to a full or half lens geometry originating from the omittance of the central beam stop [YC13].

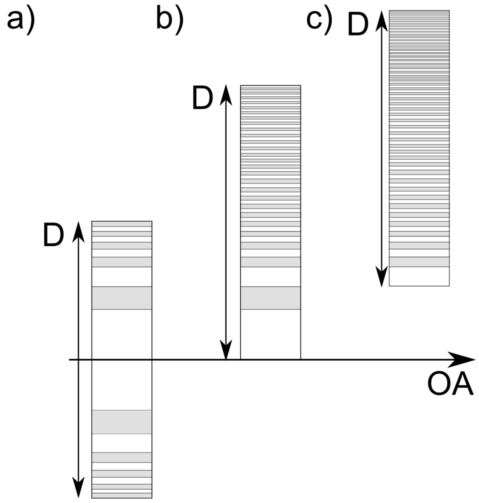

Figure 2.10: Full, half and partial geometry MLL with the same physical aperture.

A second geometry differentiation is made between *flat*, *tilted*, *wedged* and *curved* [KMS+06, YMM+07]. Earlier publications also used the term *ideal* for what is now usually referred to as wedged or curved [KMS+06]. These concepts refer to as how well the optimal shape for focusing – confocal ellipses – is approximated by the actual structure. Figure 2.11 shows a part of a set of confocal ellipses with vertical intersections representing the geometries used for MLLs. The wedged geometry approximates the ellipse borders with straight interfaces which are not parallel while the curved geometry exactly resembles the cut out part of the ellipses. The curved geometry is the optimum, that can be reached in order to obtain the best focusing as discussed in the calculation section 3. The rightmost cutout is an “arbitrary” rectangular cutout, which also has curved interfaces. Due to the manufacturing process, this cutout corresponds more to the actual geometry of MLLs than the previous one. However so far only MLLs with straight interfaces have been manufactured.
A wedged lens is obtained, if the slope of the zone boundaries are made so they meet in a point with approximately double the distance of the focal length. This can be expressed by an additional scale factor $a(z)$, which is a function of the position along the optical axis [CLQ+08]:

$$a(z) = 1 - \frac{z}{2f} \tag{2.17}$$

This is a sufficient approximation, if the focal length f is much larger than the section thickness t. Otherwise the curved geometry is necessary in order to obtain optimal properties. This requires to have the following scale factor:

$$a(z) \approx \sqrt{1 - \frac{z}{f}} \tag{2.18}$$

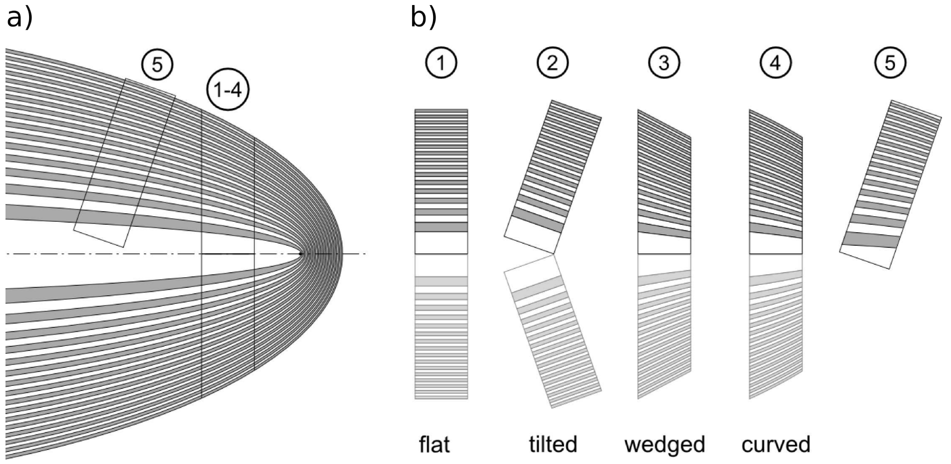

Figure 2.11: a) Part of confocal ellipses with b) the geometries (1) flat, (2) tilted, (3) wedged and (4) curved; they are a result of a cutout and an approximation of the ellipses at that position. (5) is a cutout with a different orientation and curved interfaces. Full lenses include the lighter grey parts.

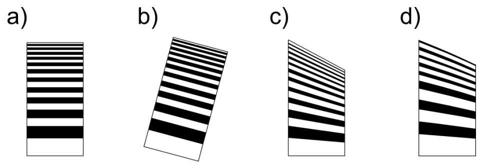

Figure 2.12: Flat, tilted, wedged, curved geometry as usually shown in literature.

Calculations of their properties are discussed in section 3.2 and the manufacturing of wedged MLLs is discussed in section 4.2. Retrospectively it would seem more adequate to introduce a different denomination for half and partial MLLs. The first differentiation is the physical shape of the lens:

- all zone interfaces are parallel (flat MLL)
- interfaces are straight but point toward double the focal length (wedged MLL)
- interfaces are curved according to the ideal ellipsoid shapes (curved MLL)

In any case the lenses have to be tilted to be at aligned to their optimum angle, which results in best diffraction efficiencies and focusing properties. Using these definitions a differentiation between flat and tilted lens is redundant for MLLs. Therefore there is a *manufacturing geometry* and usually an *application geometry*. This partly depends on the sectioning process of the lens.

Full lens optimization

There are approaches of making circular thin film lenses, so called multilayer zone plates (MZP), which usually represent a full flat geometry. A tilted geometry similar to the tilted MLL can be achieved by a cone substrate as shown in [KTT$^+$11].

Currently apparently the best transmission diffractive optics would be a full and partly apodized curved MZP. This would imply the maximum possible efficiency from all possible variants of a transmission diffractive optics of this kind:

1. Thin film structures offer the possibility to achieve optimal section thicknesses for maximum efficiency.
2. The curved geometry is superior in terms of exploiting the available aperture of the lens.
3. The concentric structure requires only one lens and there is no loss from the crossed geometry and the square dependency on the individual efficiency.
4. With superior flux from the first focusing order it might be possible to relinquish a central beamstop.

Based on the classifications in this section the term *MLL* will be used equivalently to all linear partial flat MLL in this thesis, if not stated differently.

State of the scientific knowledge and development

Several groups are working on the development of MLLs and many papers have been published on the results before and during the work on this thesis.
Based on the principle of the FZP, first approaches have been made in the 1980s and 1990s to manufacture multilayer zone plates where the zones are represented by a transparent and opaque material manufactured by thin film deposition techniques [RS80, RNS82, KS95]. Limited capabilities to produce thin and smooth layers onto a round substrate have limited the achievable results and prevented a breakthrough of this type of lens at that time. This, however, laid the fundamentals for more recent development until after refractive lenses have been successfully manufactured this type of diffractive transmision lenses has not been pursued very insistently for a while. Only more recently several groups have published work on this topic again [KTT$^+$11, KRM$^+$14, EODK15].
Linear lithographic zone plates have already been known considered quite early [HSMH66]. In the first decade of the 21st century the thin film deposition technique has achieved very reasonable smothness and reliability for the production on flat surfaces and thus the linear zone plate approach was transferred towards a thin film transmission optics. A first proof of concept paper aiming in this direction discussed calculations and experiments with a transmission diffraction grating made by thin film deposition [KSL$^+$04]. The first publication mentioning the term multilayer Laue lens has been published in 2004 [MSV$^+$04]. Calculation results for MLLs based on Coupled Wave Theory (CWT) and propagation algorithms have been shown [SKP$^+$05, KMS$^+$06].
The development of MLLs has been published continuously and calculations, expected efficiencies and limitations of the respective geometries, manufacturing challenges in terms of deposition and the manufacturing process were discussed [YMM$^+$07, KSL$^+$07, CLQ$^+$08]. Meanwhile, several groups have fabricated first lenses and have tested their performance [KMS$^+$06,

KIT+08, YRS+11]. Remarkable progress has been made by achieving spot sizes well below 20 nm with flat lenses [KYW+08, HYN+13] and wedged MLL results have been published most recently [HCB+15, MPA+15, KMG+17].
After many calculations of MLLs have been in press, recent papers aimed more on the achievement of relevant measurements or manufacturing relevant calculations [YCM+13]. First applications have been shown and aspects of the design and manufacturing process of the lenses have been discussed more in depth or are in progress [YCM+13, YC13].

MLL designs

In this section some aspects of the design requirements of MLLs for the use in focusing applications will be discussed. The term *design* will be used for a set of properties of the lenses: the focal length and a corresponding photon energy, either the inner and outer radius of the lens or the zone numbers in the lens. Other properties such as the aperture are then unambigously defined.
Due to the presence of multiple diffraction orders that have to be separated in case of zone plates and MLLs, the working distance is smaller than the focal distance. For MLLs in most cases it is necessary to use an order sorting aperture, which is located between the lens and the focal plane at that distance, where the first focused order is physically separated from the zeroth order which is shown in Figure 2.8 b). The order separation has to be done as the orders can introduce a significant background signal in the measurement. If the background would be negligible, the order sorting aperture could be omitted.
The working distance is a function of the distance of relative distance between the innermost zones and the optical axis and the outermost zones and the optical axis [YC13]. Due to the off-axis geometry a larger working distance in relation to the focal length is achieved if the innermost zones are moved outwards. The geometric working distance wd for an MLL can be calculated by the intercept theorem using the inner radius r_{in} and the physical aperture of the lens D:

$$\frac{wd}{f} = \frac{\frac{r_{in}}{D}}{1 + \frac{r_{in}}{D}} \tag{2.19}$$

The the respective graph is shown in Figure 2.13.
The first MLLs made in Dresden were made from depositions, which started with zone number 1 [BKM+13]. Such a design imposes several challenges. The thickest and thinnest layers had a ratio of the thicknesses of 64 : 1. With such a design the angular velocity of the substrate movement changes over almost two orders of magnitude. Due to technical limiations in the controller/motor combination, this imposed significant challenges on the accuracy, in particular. Additionally, this type of design is not optimal in terms of working distance. As shown in Figure 2.13 the working distance for $r_{in} = 0$ is zero as part of the transmitted beam will pass the order sorting aperture. To overcome the virtually nonexisting working distance optimized designs have been drafted. The designs discussed in this thesis can be found in Table 2.1. Most of the depositions have been made in the deposition machine at

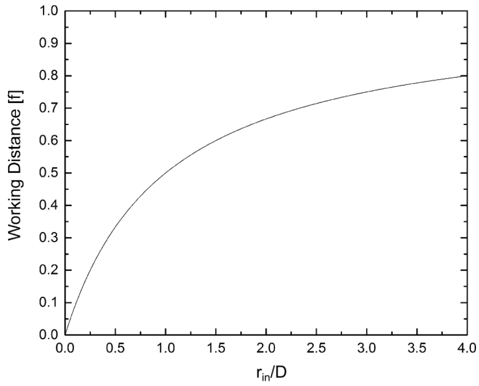

Figure 2.13: Working distance/focal length ratio as a function of the fraction innermost radius r_{in}/D.

Table 2.1: Deposition designs used in the scope of this thesis. Design energy and focal length, number of zones is given according to the zone plate law; total thickness according to the design.

Name	Made at	Focal length/energy	Zones	Total thickness [µm]
DDD20@20_50[1]	IWS	20 mm @20 keV	50 - 2500	50 µm
DDD9@15_50	IWS	9.5 mm @15 keV	850 - 7850	53 µm
DDD9@12_50	IWS	9 mm @12 keV	970 - 6970	50 µm
N100	BNL	9.6 mm @12 keV	632 - 15170	102 µm

Fraunhofer IWS [BMM+02] and one of them in the deposition machine of the Brookhaven National Laboratory (BNL) by Raymond Conley and Nathalie Bouet [CBB+09].

In a first step general requirements for the lens have to be defined. They will have the most significant influence on the lens design:

- Desired photon energy
- Desired resolution (numerical aperture)
- Desired working distance (distance from the order sorting aperture to the focal plane, given by the dimensions of the sample or additional experimental equipment)
- Desired setup space (distance from the lens to the order sorting aperture)

For a full zone plate aperture the relation between resolution d and outermost zone width dr_{min} according to the Rayleigh criterion is given by:

$$d = k \cdot dr_{min} \tag{2.20}$$

[1]Experimental results with a lens made from this deposition have been published in [KBN+14a]; experiments were performed at PETRA III beamline P06 and are not discussed in this thesis as the results have been superseded by later experiments.

k or "k-factor" depends on the geometry of the lens (e.g. circular, square) and the distribution of the local focusing efficiency and is usually in the order of 1. The direct relation between the outermost zone width and the resolution, however, is only valid for full FZP geometries. For half or partial geometries an additional factor has to be considered in order to reflect the "missing" part of the lens, which does not count into the numerical aperture. In order to achieve the same numerical aperture for off-axis geometry lenses needs to involve parts of the design which are located farther away from the optical axis than for a full geometry. Therefore, smaller zones have to be manufactured for the same resolution. For a half geometry with an identical focal length and an identical aperture as shown in Figure 2.10 b) requirements on the zone width increase to:

$$d = 2k \cdot dr_{min} \tag{2.21}$$

For the same physical aperture more zones have to be manufactured. For a double radius the zone width is reduced by half. For a partial MLL this requirement changes to:

$$d \approx 2k \cdot \frac{1}{1 - \frac{r_{in}}{r_{out}}} \cdot dr_{min} \tag{2.22}$$

r_{in} is the inner radius, r_{out} the outer radius. As more inner zones are omitted, the outermost zone width has to be smaller. According to [YC13] a good choice for the fraction $\frac{r_{in}}{r_{out}}$ is 0.2. Thus, 20 % of the inner zones are omitted. For a 10 nm diffraction limited focus zone widths in the range of 4 nm are necessary instead of 10 nm as for a full geometry.
Further limitations might occur due to unevenly distributed focusing efficiencies over the aperture of the lens especially for flat or tilted lenses. This will decrease the effective aperture and therefore limits the achievable resolution with flat lenses [KMS+06]. These limitations can be overcome in part by using wedged or curved lenses, which usually have a very evenly distributed diffraction efficiency.
In this thesis the resolution is given as the Full Width Half Maximum (FWHM). The k-factor is known to be 1.22 for circular apertures and in general can be directly derived by the calculation of the point spread function of the shape of the aperture [Att07]. The point spread function pattern can be calculated using the Fourier transformation of the respective aperture. For a circular aperture the point spread function is called Airy pattern and corrsponds to the Bessel function of the first kind. For a rectangular aperture the point spread function corresponds to a sinc^2-function in both directions [BW13].
In the zone plate geometry usually a beam stop has to be inserted in a position on the optical axis. In this case the point spread function generally shows similar characteristics as compared to the circular Airy pattern but has more intensity in the side lobes. This behavior is called apodization effect [EDA+16]. This is the result of the deviation from the radial boxcar function in the profile.
Implicitly it was assumed, that the local focusing efficiency is evenly distributed over the aperture. Although the shape of the aperture of a lens might correspond to one a solid circle or square, the distribution of the effective aperture might differ. In fact for many transmission

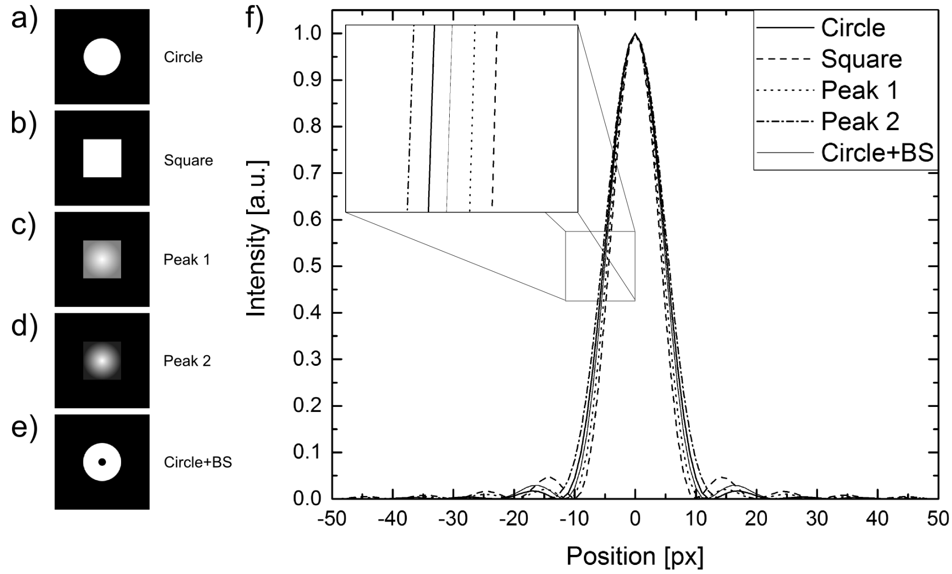

Figure 2.14: Physical apertures and corresponding point spread functions: a) circular aperture, b) rectangular aperture, c) rectangular aperture intensity gradient, d) rectangular aperture with narrow intensity gradient, e) circular aperture with central beamstop and f) plot of the respective point spread functions.

diffractive optics the local focusing efficiency is strongly dependent on the local zone width, the angle of incidence of the beam. Several publications have shown the differences in the local efficiency for flat, tilted and wedged lenses. Wedged geometry lenses have a very uniformly distributed diffraction efficiency for most zone widths. Tilted MLLs show a distinct peak in efficiency in that part of the lens, where the Bragg diffraction is fulfilled. The diffraction efficiency drops very significantly for other parts of the lens. For flat lenses some efficiency is found for the innermost part while it drops for outer zones [KMS$^+$06].
Examples for the local efficiency distribution and corresponding point spread functions are shown in Figure 2.14. The square apertures represent the MLL aperture with different efficiency distributions. For a narrow peak in the intensity the fourier transformation shows a wider peak which reflects the effects of narrow local efficiency peaks for tilted MLLs.
Several calculation methods exist, which can estimate the diffraction efficiency of a bilayer system. The already mentioned two-beam approximation does take into account only the first order diffraction and therefore overestimates the actual expected efficiency. It can still be used as a good estimate in order to compare efficiencies at different energies of for different materials systems. The choice of materials mainly depends on two different aspects:

1. Deposition and manufacturing properties

2. Optical properties

First and foremost materials have to be found, which can be used with the desired deposition technology. The properties of those materials have to be in line with the expected behavior and properties of the produced multilayer coating.
For Magnetron Sputter Deposition (MSD) is necessary to pay attention to the following properties:

1. Conductivity
2. Deposition rates
3. Amorphous or nanocrystalline growth
4. Interdiffusion properties of neighboring materials

Figure 2.15 shows the theoretically expected efficiencies as a function of the thickness for different material combinations according to the two-beam approximation. It can be seen, that the optimum thicknesses change with different relative phase shifts. Different orders are disregarded by the method and therefore the maximum efficiency η with phase shifting materials is $\approx 100\,\%$ as it assumes dynamical diffraction across the whole lens.

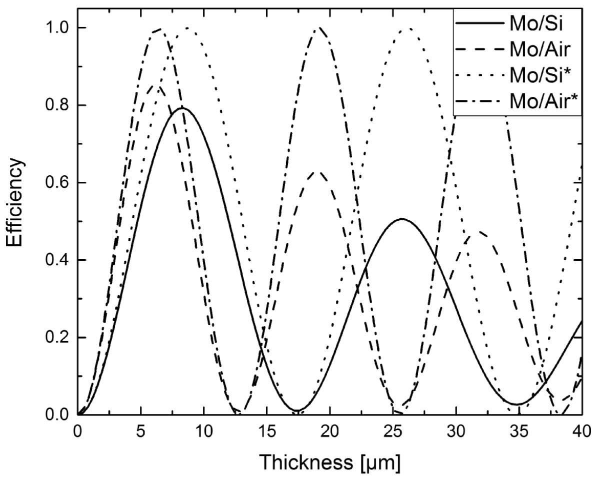

Figure 2.15: Comparison of diffraction efficiencies of different theoretical material combinations in dynamical diffraction calculated by the two-beam approximation: Mo/Si, Mo/Air, Mo/Si* with no absorption and Mo/Air* with no absorption.

Synchrotron radiation X-ray Sources

Test of the focusing performance and other tests have been made at synchrotron radiation facilities. A synchrotron light source is a large scale electron or positron storage ring which features several experimental stations for radiation generated by a deviation of the particle beam. This is usually done using several types of magnetic structures and arrangements such as undulators and bending magnets which are described in [LM90]. Depending on the layout the exiting beams can be in the hard X-ray regime with photon energies of several tens of keV but can also have a significantly lower energy down to the infrared region [SKB+14, PS16].
A bending magnet is a bipole magnet, which changes the direction of the ring electrons. The change in direction leads to tangential radiation and emits a continuous spectrum of photon energies. An undulator uses many consecutive dipole magnet sections. The geometry is designed to ensure an overlap of the individual radiation cones. The result is positively interfering radiation, which leads to distinct radiation characteristics. Undulators can achieve very high intensities and newest developments are used in Free Electron Lasers (FELs) [GSS+10].

FELs use a very long linear accelerator and long undulator in order to achieve very short pulsed radiation.
The synchrotron radiation sources and respective beamlines visited and used in the scope of this thesis are listed in Table 2.2. Many other sources are scattered around the world. According to [Lis17] there are currently around 60 relevant light sources worldwide.

Table 2.2: List of synchrotron radiation sources.

Facility	Location	Circumference	Electron energy	Beamline	Type
APS	Argonne, USA	1104 m	7 GeV	1BM	bending magnet
ESRF	Grenoble, F	844.4 m	6 GeV	ID13	undulator
PETRA III[2]	Hamburg, D	2304 m	6 GeV	P06	undulator

[2]See footnote 1 on page 35.

3 X-ray Optics Characteristics Calculation

In this section calculations of the properties of MLLs will be presented and discussed. The emphasis lies on the focal shape and size and the efficiencies for ideal as well as non ideal MLLs and their alignment from which tolerances can be drafted. Calculations include the focal profile as a function the layer placement error and misalignment in a 2D setup as well as general efficiency considerations for a range of energies. The Strehl ratio is used in order to evaluate the quality a lens [Wel86]. If not stated differently for particular calculations the MLL design stated in Table 3.1 will be used. MLLs manufactured based on this design have also been used for some experiments discussed in sections 5.4 and 5.5.
Material parameters have been taken from the Henke database [HGD93], where available. For energies above 25 keV the material parameters from the Chantler database have been used [Cha00].

Table 3.1: MLL design used for calculations corresponding to the design DDD9@12_50.

Photon energy:	12.0 keV
f	9.0 mm
n_{min}:	970
n_{max}:	6970
$\mathrm{dr}_{\mathrm{min}}$	5.8 nm
$\mathrm{dr}_{\mathrm{max}}$	15.5 nm
D	50.5 µm
Material:	Mo/Si

3.1 Beam Propagation Method

The Beam Propagation Method (BPM) is a method based on the direct propagation of a wave field through a structure. It can be used to calculate the properties of wavefields in various types of structures.
The principle of the BPM is to calculate the properties of the wave field with an arbitrary distribution of material properties on a step by step basis. The discretization of an MLL for the BPM is shown in Figure 3.1. Material properties of the structure are stored in a complex grid.
An initial wave field is usually defined with the following starting conditions:

$$I_0 = 1 \;\forall\; x \quad \text{and } \Phi_0 = 0 \;\forall\; x \tag{3.1}$$

The amplitude A is defined by the initial intensity I and the complex angle Φ of the wave field. The structure is segmented into individual slices, for which the wave field properties have to be calculated and the distance of these slices is given by d_{prop}. The principle of the step by step calculation is as follows:

1. Initial wave field is propagated towards half the designated propagation step $\frac{1}{2}d_{prop}$.
2. The resulting wave field is phase shifted by the real part of the complex index δ of refraction of the respective materials and reduced in amplitude by the damping factor. The new intermediate wave field is calculated by $A(t)_{\mathrm{mod}} = A(t)\exp(i\delta)\exp(-2\frac{\pi}{\lambda}\beta d_{prop})$.
3. Wave field is subsequently propagated forward half a propagation step $\frac{1}{2}d_{prop}$. This represents the final situation of the slice.
4. Steps 1.-3. are repeated until the full propagation thickness has been reached.

If the properties of a tilted lens are supposed to be calculated the wavefield at the entry plane of the lens is slanted instead the whole structure. This situation is shown in Figure 3.1 b). This modified slanted phase for the angle α for positions x along the radius is calculated by:

$$\Phi(x) = xk \sin\alpha \tag{3.2}$$

In this case the wave field at the exit plane of the lens is slanted back for the same angle.

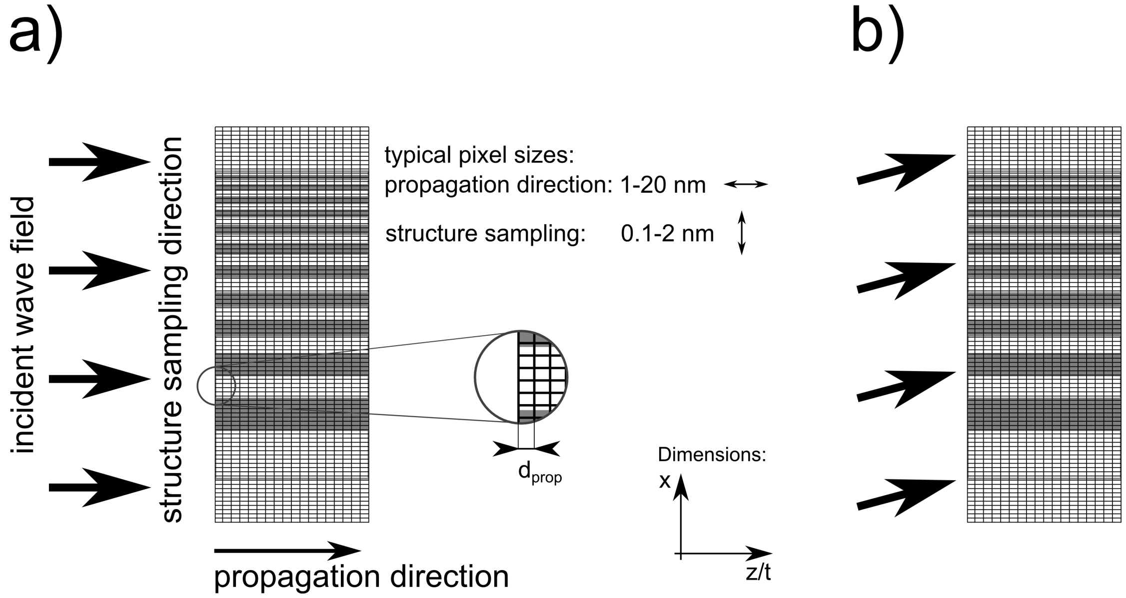

Figure 3.1: a) Basic principle of the implementation of the BPM with the grid and the individual material properties. On the left side the wave field with the starting conditions has to be initialized.
b) Tilting of the structure is simulated by tilting the incoming beam.

The accuracy of BPM calculations mainly depends on resolution of the structural grid perpendicular to the propagation direction. In [LHW$^+$14] the accuracy of the calculations has been determined as a function of the respective pixel sizes for MLL structures. Using a pixel along the structure of approximately one order of magnitude smaller than the smallest zone width considered has shown to obtain sufficiently accurate results; however, in the propagation direction even a propagation step more than pixel size of several times the smallest zone width was sufficient. The implementation of the FFT-BPM algorithm used in this thesis was inspired by [Rum13]. The BPM algorithm uses free space propagation and therefore the results do not take into considerations total reflection with this current implementation. However, the critical angle is significantly smaller than the first order Bragg angle and the effects of total reflection are neglected.

For the calculations the smallest pixel size on the MLL grid was chosen in general to have a maximum size of one tenth of the outermost zone width and individual propagation steps were generally calculated with $\mathrm{d}_{prop} = 5\,\mathrm{nm}$. The numerical calculations have been performed using a desktop computer with 16 GB RAM and an Intel Core i5-3570. Typical dimensions of the calculated field are $67\,\mu\mathrm{m} \times 20\,\mu\mathrm{m}$. The maximum number of pixels used along the MLL stack height was 2^{20} px but usually 2^{17} px have been used. The full physical spread of the propagation array is the full size of the MLL perpendicular to the propagation direction with usually several tens to hundreds of thousands of pixels and up to several tens of micrometers in the propagation direction which corresponds to the section thickness.

Starting from results of the BPM further calculations can be made as shown in Figure 3.2 and described in the following.

It is not possible to calculate the local and total diffraction efficiency directly from the wave field at the exit of the MLL structure. In order to calculate the efficiencies further steps have to be considered. The wave field at the exit plane of the MLL has to be propagated in a plane, where order separation is ensured. This plane can be near the theoretical focal plane, which simultaneously allows to determine the properties of the focus as shown in Figure 3.2 a). The total intensity in the focal plane around the first order focus divided by the intensity at the entry plane of the lens represents the total efficiency of the first focusing order. In order to determine the local efficiency the wave field has to be propagated back into the exit plane of the lens after other parts of the beam, in particular the direct beam, have been cut off by a virtual order sorting aperture by setting the intensities outside the pinhole to zero. The intensity of the resulting wave field is the distribution of the local diffraction efficiency as shown in Figure 3.2 b). The wave field at the focal plane can also be propagated further downstream in order to obtain its shape in the far field as shown in Figure 3.2 c). These calculations can also be performed for different diffraction orders by choosing the propagation distance accordingly. This method has periodic boundary conditions which have not been compensated for [KK86]. This means intensity leaving on one side will enter on the opposite side of the grid. Therefore, the size of the propagation grid has to be chosen sufficiently large in order to physically enclose all orders with a significant diffraction intensity (generally the first three diffraction orders). It is possible to evaluate the wave field in the lens at every section thickness separately. This is usefull in order to calculate depth dependent properties such as the efficiency or the shape of the focal profile by using the intermediate wave fields inside the structure in order to propagate those towards the focal plane.

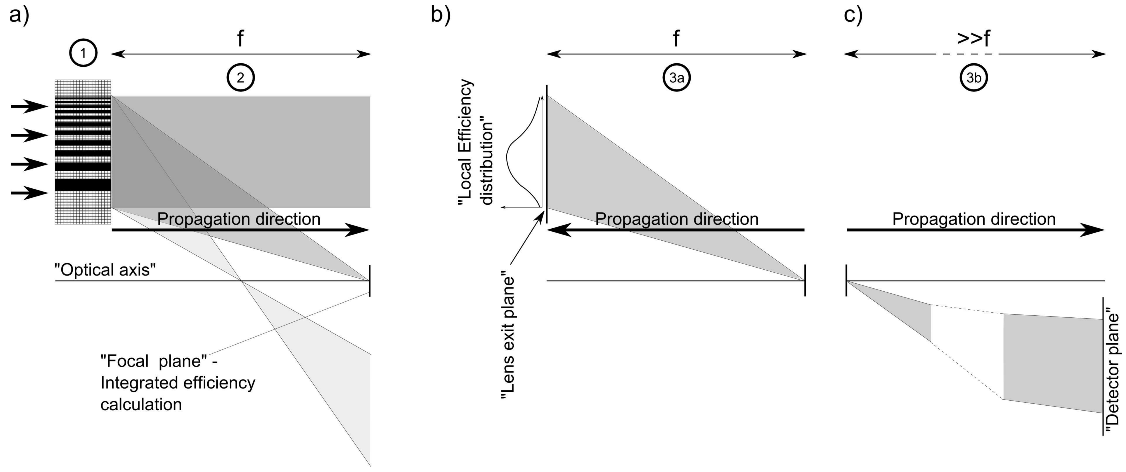

Figure 3.2: a) Propagation through the lens and propagation to a position near the designated focal plane.
b) Propagation back to the lens exit plane after other diffraction orders have been stripped away. The intensity of the resulting wave field represents the local diffraction efficiency.
c) The wave field can also be propagated into the far field.

3.2 Basic properties of flat, tilted and wedged MLLs

In this section specific differences in efficiency and behavior between flat, tilted and wedged lenses will be discussed. Tilted and wedged geometries can be utilized in order to make use of dynamic diffraction effects to increase the local diffraction efficiency of the structure.
In Figure 3.3 the calculated local diffraction efficiencies are shown as a function of the position on the MLL as well as a function of the the section thickness t together with the respective focal profiles for an a) flat, b) tilted and c) wedged geometry. The local efficiencies were calculated as discussed in the previous sections. The focal profiles have been taken at the theoretical focal length of the lens for each section thickness. Results show strikingly the difference between the flat, tilted and wedged geometries. Similar local efficiency maps have been shown in [KIT$^+$08, YCBC14].
For the flat geometry MLL only the inner part representing the larger zone widths features a significant efficiency. With an increasing section thickness the maximum local diffraction efficiency drops and several distinct regions in the lens feature separated only some diffraction efficiency are present. The focal profile for the flat lens for smaller section thicknesses shows a regular single peak. For larger section thicknesses the multifold distribution also results in multiple peaks.
The calculations of the tilted geometry lens are made at a tilting angle, where the total diffraction efficiency of the lens is maximal due to the fulfilled Bragg condition. It is evident, that the part near the center of the lens for a section thickness around 8 µm features the largest diffraction into the first focusing diffraction order. The focal profile at the theoretical focal plane shows a distinct maximum, which does not split up into several separated beams with an increasing thickness but moves perpendicular to the propagation direction. This geometry also features a significantly increased local efficiency for a large part of the lens and

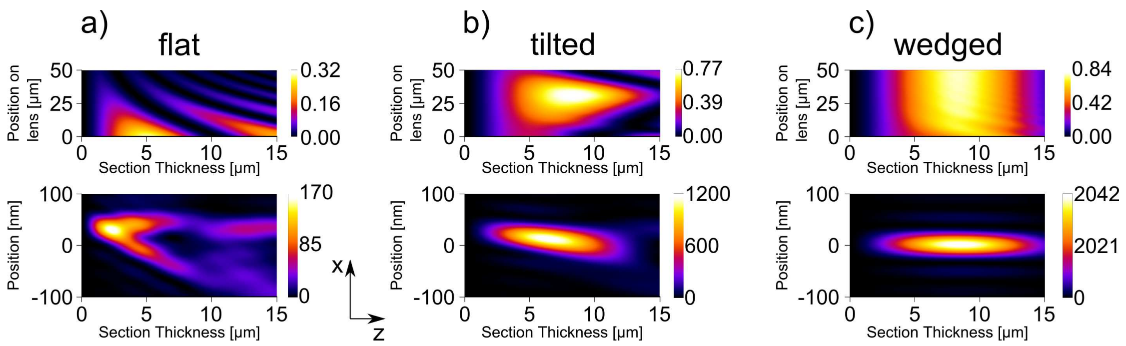

Figure 3.3: Efficiency maps of a) flat, b) tilted and c) wedged MLL as a function of the position on the lens and the section thickness. Focal profile maps of d) flat, e) tilted and f) wedged MLLs as a function of the section thickness.

thus also a significantly higher total diffraction efficiency. As a result the peak intensity for the tilted lens is significantly larger than compared to the flat lens.

The wedged MLL features a very similar maximum local diffraction efficiency as the tilted lens. However, it can be utilized over almost the full aperture of the lens at the optimum section thickness. As a result the total diffraction efficiency is superior and it also features a well-defined focal profile.

The total diffraction efficiencies into the first focusing order as a function of the section thickness are shown in Figure 3.4 a). Besides the different maximum total efficiency every geometry shows its maximum at a different section thickness due to the different use of dynamic diffraction effects. The flat lens has the smallest optimal section thickness and efficiency; dynamic diffraction effects are not utilized with this geometry. The tilted lens has a significant advantage over the flat lens in terms of the maximum total diffraction efficiency; it also achieves its maximum for a larger section thickness due to the partly transition to dynamic diffraction effects. The wedged lens achieves an even larger total diffraction efficiency at an even larger section thickness as listed in Table 3.2.

Table 3.2: Best efficiency and necessary section thickness for flat, tilted and wedged MLLs.

Geometry	Maximum Efficiency	Section Thickness [μm]
flat	8.3 %	3.7 μm
tilted	47.8 %	6.8 μm
wedged	74.5 %	8.4 μm

However, it has to be emphasized, that taking into account only the value of the absolute efficiency can be misleading. The measured efficiency is determined as the integrated intensity on a plane with a certain width. This might include parts of the beam, which actually do not contribute to the intensity in the main peak but rather to the background noise. This can be observed for the beam shape for the flat geometry lens in Figure 3.3 for larger section thicknesses, which is split up into several distinct maxima.

Figure 3.4 b) and c) show the best focal profiles for all geometries in direct and normalized comparison, respectively. The wedged lens has a slight advantage in terms of the focal spot size for this particular aperture.

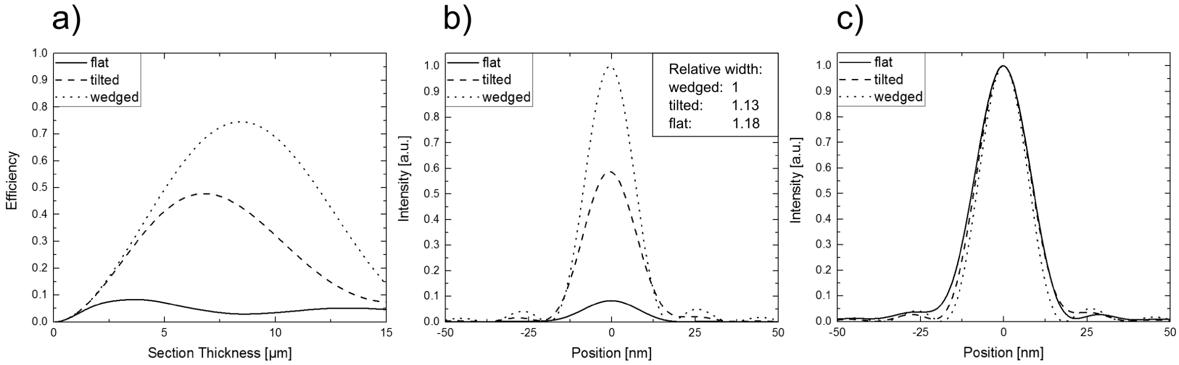

Figure 3.4: a) Diffraction efficiency as a function of the section thickness for flat, tilted and wedged MLLs. This corresponds to the total diffraction efficiency calculated based on Figure 3.3 a) - c)
b) Line profiles in direct comparison normalized to the maximum intensity reached by the wedged lens in theoretical focal plane.
c) Line profiles of flat, tilted and wedged MLLs normalized to their respective maximum intensity in theoretical focal plane.

In Table 3.3 lens designs *2f* to *f/8* are listed. *1f* corresponds to the lens design listed in Table 3.1. Designs *2f* to *f/8* are derived and their range from double the focal length to an eighth of the focal length while keeping inner and outer radius of the design constant. This roughly corresponds to a range from half the numerical aperture to an eightfold numerical aperture as compared to the *1f* design.
The calculations show the significantly reduced local efficiencies for larger apertures for the flat geometry. For the tilted geometry the area with a significant local diffraction efficiency is also reduced with increasing numerical aperture and increased diffraction angles. For large section thicknesses the beam also gets distorted and two distinct peaks can be observed; this is a result of "missaligned" dynamic diffraction inside the lens. This is indicative for the limited capabilities of MLLs with parallel interfaces in terms of the maximum diffraction efficiency. However for small section thicknesses with little effect from dynamic diffraction focal properties are near the expected optimum but with a very limited efficiency. For the wedged aperture the local efficiency distribution is almost constant for the lens designs *1f* to *f/4*. In calculations of *2f* it can be observed, that the larger zone widths around 20 nm have a significantly reduced diffraction efficiency even in Bragg condition; this corresponds well with calculations in [KIT+08]. Also of interest is the behavior for the calculations of the wedged MLL *f/8*. The diffraction efficiency is reduced for the smallest zone widths below approximately 2 nm. The same design with a curved geometry does not show this behavior. This is an indication of the necessary transition to this type of geometry for very small zone widths as the Bragg condition cannot be fulfilled for the whole thickness of the MLL. Similar results regarding the expected focal spot size for flat, tilted and wedged geometries have been discussed in [KMS+06].

Assuming 2 nm as the smallest practical zone width for wedged geometries, the smallest focal spot size is approximately 5 nm according to equation 2.22. However, if efficiency is irrelevant, it is possible to obtain a diffraction limited resolution by avoiding dynamic diffraction effects as far as possible by manufacturing an MLL with a very small section thickness.

Table 3.3: Design of lenses with different numerical apertures.

Lens design	$2f$	$1f$	$f/2$	$f/4$	$f/8$
f [mm]	18	9	4.5	2.25	1.125
n_{min}	485	970	1940	3880	7760
n_{max}	3485	6970	13940	27880	55760
drn_{min}] [nm]	11.55	5.78	2.89	1.44	0.72
drn_{max} [nm]	30.98	15.49	7.74	3.87	1.94
Aperture [µm]	50.5	50.5	50.5	50.5	50.5
NA [mrad]	2.8	5.6	11.2	23.3	44.8

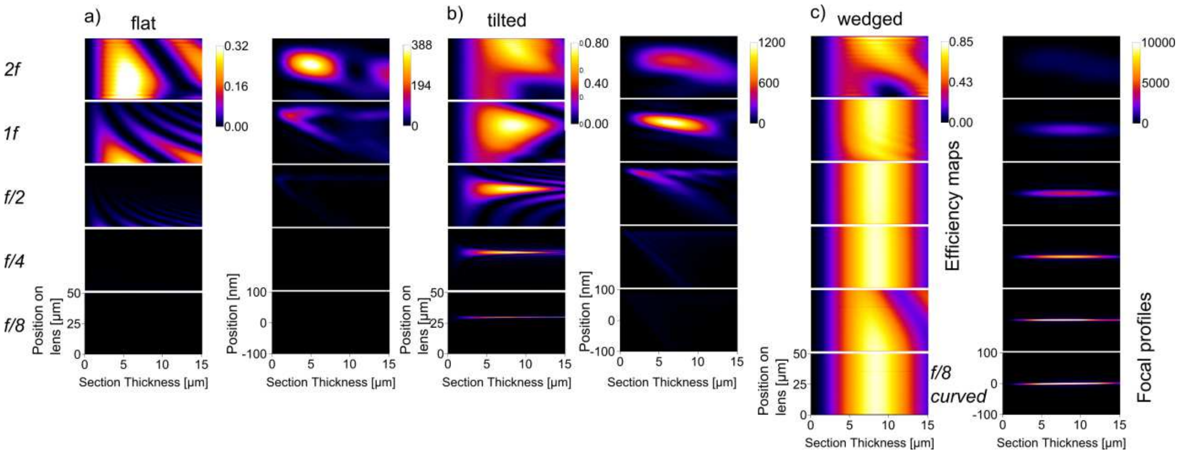

Figure 3.5: Local diffraction efficiency and focal profiles as a function of the section thickness for a) flat, b) tilted and c) wedged MLLs for different numerical apertures defined by the focal length $2f$ to $f/8$. The efficiency of the wedged MLL decreased for smaller zone widths; therefore a corresponding curved MLL was calculated.

The calculations have only considered perfectly monochromatic beams. However, according to the zone plate law (equation 2.13) the focal length is energy dependent. In [YC13] calculations have been made on the beam size of an MLL as a function of the energy spread. It has been concluded, that the monochromaticity requirements for partial MLLs are larger than for full and half MLLs as the focal plane moves along the optical axis and not the slanted beam propagation direction. For an example lens and a defined threshold beam broadening of 15% the monochromaticity requirement is 2.13×10^{-4}.

3.3 Photon Energy dependent Efficiency Calculations

As a result of the previous section it can be said the maximum efficiency of an MLL heavily depends on the geometry of the lens, the material combination used for the fabrication as well as the actual design of lens in terms of smallest and largest zone widths. In smaller zone widths the dynamic diffraction effects have a larger impact. Thus, the expected efficiency will be larger but the angular acceptance is lower [KKC+15].

In this section the expected maximum diffraction efficiency in the first focusing order is calculated. The total efficiency of the lens is calculated by the full propagation through the structure and a subsequent propagation into the first order focal plane. Here the intensity in and around the first order focus is compared with the intensity at the lens entrance. This has to be done for every thickness and tilting angle of the lens separately. The individual focusing efficiencies are evaluated and the tilting angle and thickness with the largest efficiency is determined. Calculated efficiencies for several material systems have been published by various groups [YCBC14, KMF+17].

As a reference the efficiency of a full zone structure is calculated. This full zone structure is assumed to be comparable to the partial MLL in terms of the aperture. The maximum radius is 29 µm with a central beam stop diameter of 8 µm and the geometry corresponds to a flat MLL; it is still considered to be a line focusing element.

From the calculations shown in Figure 3.6 it can be seen, how the demands for lithographically made FZPs rise. The maximum section thickness of an FZP is limited mainly by the lithographic process and improvements are challenging. Larger aspect ratios in the order of 1 : 30 have been demonstrated [VCGF+11]. However, for smallest zone widths in the order of 10 nm this would be equivalent to a maximum section thickness of approximately 300 nm. This is far less, than what is needed to obtain the maximum calculated diffraction efficiencies. Improved aspect ratios can be achieved by stacking of individual FZPs, interlacing, or by making multilayer zone plates [WRG+09, GWL+14, KTK+12, MVR+17]. However, these methods also come with their own challenges such as the positioning precision.

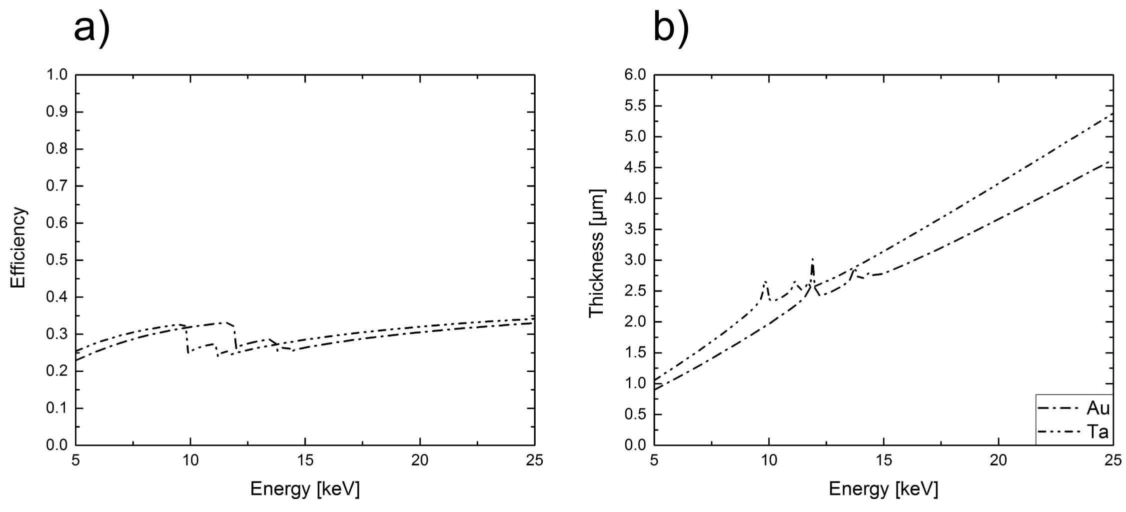

Figure 3.6: a) Calculated efficiency and b) calculated optimal thickness for a flat Au and Ta FZP-like structure.

The calculations of MLL efficiencies have been done for tilted and wedged geometries. In general for tilted MLLs the efficiency is heavily dependent on the tilting angle; the optimum angle also changes as a function of the photon energy. In order to reduce the computational effort in calculations the efficiency is calculated only for several angles and intermediate values are approximated using a second order spline interpolation. This is made under the assumption, that the efficiency function is smooth. The spline of the efficiency is calculated with tilting angle and thickness as free parameters and the maximum of this spline was calculated using an array with 100 times the original density.

The material combinations taken into account for the calculations are all based on silicon as the spacer layer and tungsten, molybdenum or vanadium as the absorber layer. For many lenses reported in literature the respective silicides of the absorber materials have been in use or have been considered [KMS+06, YRS+11, KBN+14a]. They tend to have a lower absorption and phase shift due to the lower density but apart from that feature very similar properties to the bulk material. Therefore, the general properties can be assumed to be very similar for a wedged MLL.

Figure 3.7 shows the expected diffraction efficiency into the first focusing order for tilted and wedged MLL, respectively. Generally the tungsten-based lenses have the smallest optimum thickness, followed by the molybdenum-based lenses. Vanadium-based MLLs need by far the largest section thickness in order to achieve their best focusing efficiency. For wMLL molybdenum-based lenses have the largest diffraction efficiency for up to an photon energy of 20 keV due to the molybdenum-K absorption edge. Above 20 keV the V-based system outruns this advantage. For tilted MLLs the situation is somewhat different. Due to the large necessary section thickness only a part of the lens is in Bragg condition and the dynamic diffraction effects effectively reduce the overall diffraction efficiency as compared to tungsten- and molybdenum-based systems.

MLLs have to be employed in a crossed geometry of two lenses for point focusing or imaging. Therefore, the efficiency for the point focusing element is the square of the efficiencies of the individual lenses. The efficiency for two crossed lenses is plotted separately in Figure 3.8. It is evident, that two tilted molybdenum-based MLLs reach a maximum efficiency of $\approx 27\,\%$, while two crossed wedged lenses reach up to $\approx 75\,\%$ combined.

For photon energies between 25 keV and 100 keV similar calculations have been made and are shown in Figures 3.9 and 3.10. It is evident, that the possible efficiencies for two tilted MLLs are rather limited reaching a combined efficiency of around 40 % just below 70 keV for a tungsten-based system, while two wedged MLLs can reach an efficiency of more than 90 % in case of vanadium-based systems. The large difference between the efficiencies of tilted and wedged MLL is intriguing; it is a result of the large necessary section thickness for optimum efficiency. For the tilted geometry this is however only utilized in the small part with Bragg diffraction.

For Multilayer Zone Plates (MZPs) similar aspect ratios as for MLLs can be reached; additionally MZPs are point focusing elements and therefore do not need a second optical element, which would reduce the diffraction efficiency. MZPs have also already been tested using hard X-rays. A *tilted*- and *wedged*-like MZP-geometry, where the layer interfaces are not parallel to the optical axis were partly considered to be made on a tapered wire core and with a graded multilayer thicknesss, respectively [KTT+11]. Due to the challenges of producing a

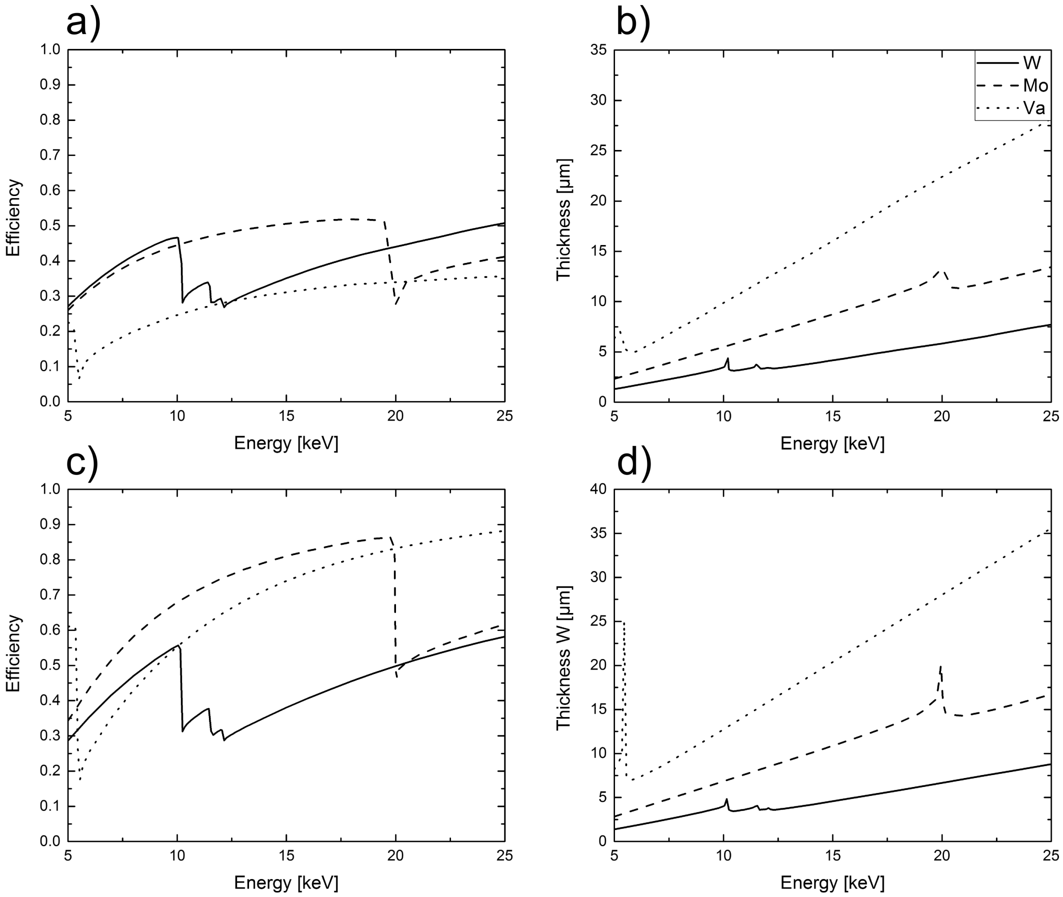

Figure 3.7: a) Calculated efficiency and b) calculated optimal thickness for tilted MLL. c) Calculated efficiency and d) calculated optimal thickness for wedged MLL. Tungsten, molybdenum and vanadium are considered as the absorber and silicon as the spacer material.

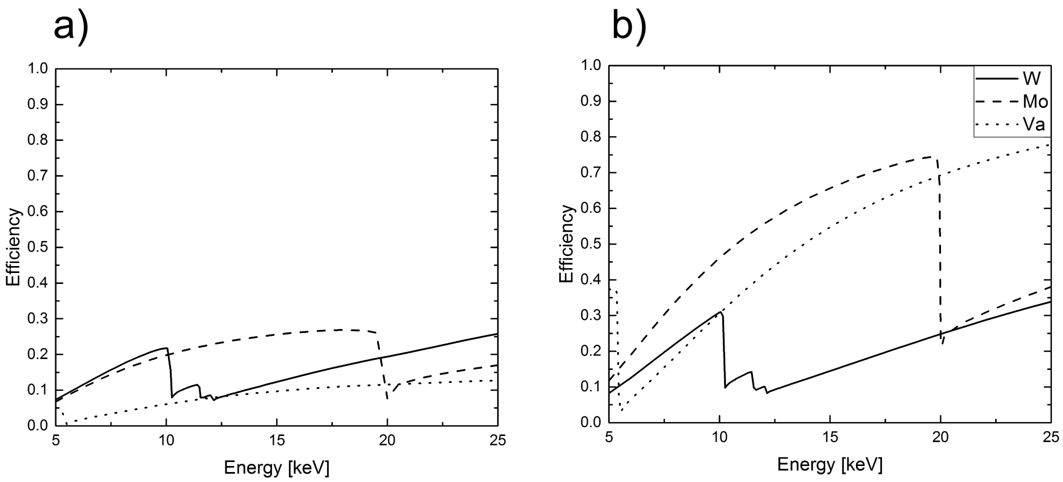

Figure 3.8: Efficiency of two crossed MLLs with a) tilted and b) wedged geometries.

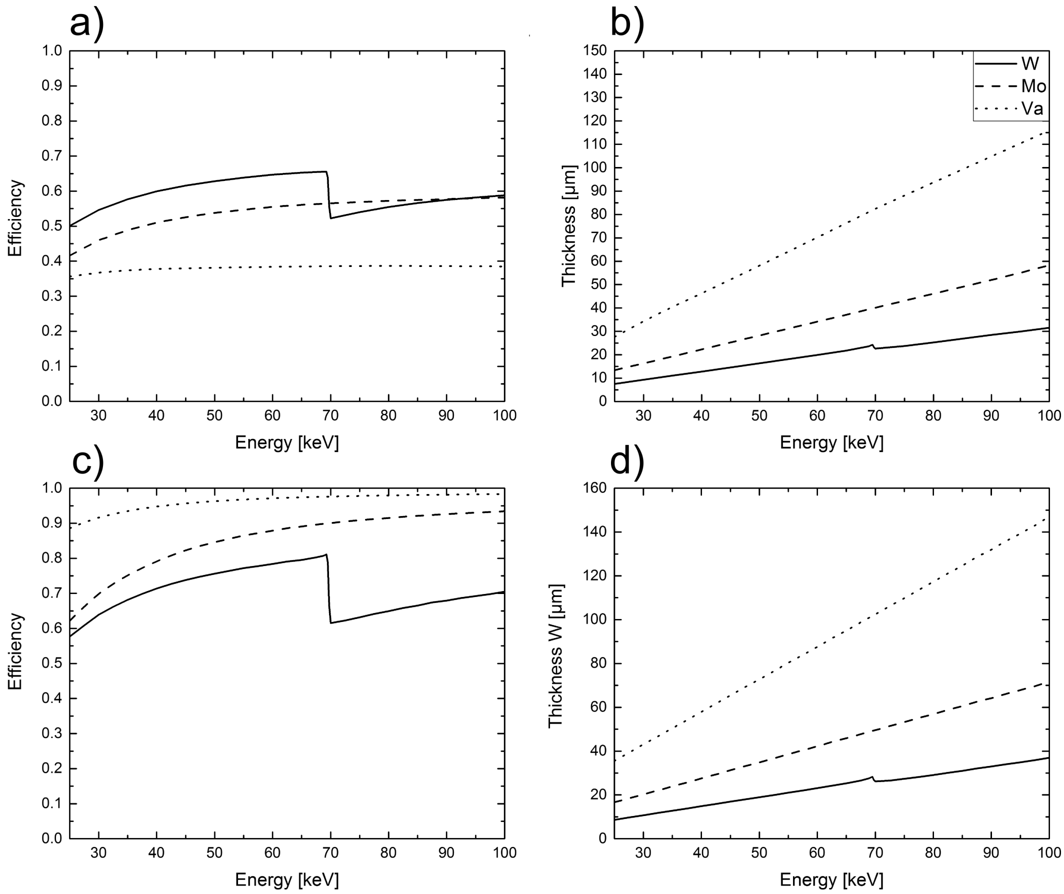

Figure 3.9: a) Calculated efficiency and b) calculated optimal thickness for single tilted MLLs. c) Calculated efficiency and d) calculated optimal thickness for single wedged MLLs.

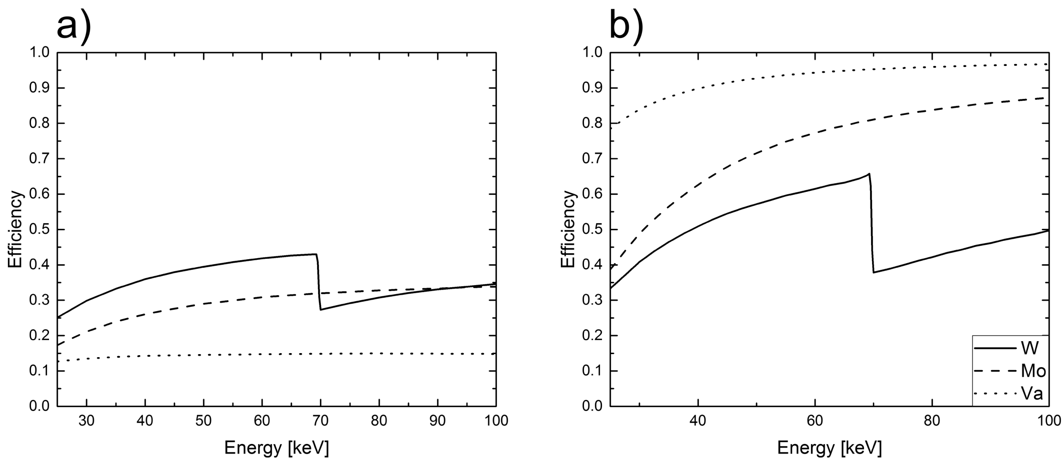

Figure 3.10: Efficiency of two crossed MLLs with a) tilted and b) wedged geometries for energies from 25 keV to 100 keV.

flawless wedged deposition it is therefore assumed, that currently the maximum achievable efficiency with a good focal spot corresponds to a tilted-like MZP. Although the circular geometry differs from the the MLL geometry, the estimation is still based on the linear MLL geometry. Deviations from the equal thicknesses or widths of more and less absorbing and phase shifting materials and the slanting angle are expected to have larger impact on the efficiency than the difference in circular/linear geometries.
Figure 3.11 shows a direct comparison for the expected efficiencies of different diffractive transmission geometries including two crossed MLLs in tilted and wedged geometry, MZP and FZP with their respective optimum section thicknesses. It shows the large benefit of wedged and tilted geometries in particular. Eventually it would be most favorable to fabricate MZP with a wedged geometry in order to exploit the full potential of diffraction optics with a large section thickness. Due to the large expected gain (i.e. the relative increase in intensity in the area of the focal spot compared to the intensity behind a pinhole of the same size) it would be possible to use the lenses without a beam stop for suited experiments [Pra14].

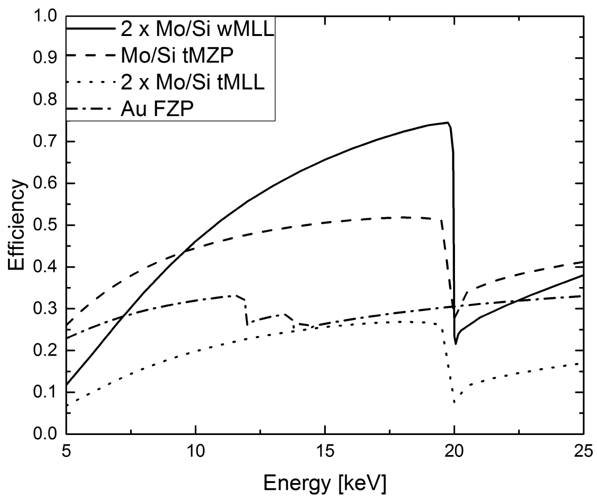

Figure 3.11: Efficiency of a crossed wedged Mo/Si MLL systems, a tilted-like MZP, crossed tilted MLL and Gold-FZP optics in direct comparison.

In Figure 3.12 the expected two-beam approximation calculated efficiencies are plotted for energies from 5 keV to 25 keV for two types of calculations. The first represents an MLL optimized in terms of the section thickness for a fixed photon energy of 12 keV; the second represents lenses optimized for each individual photon energy. The calculation shows a lens made for a specific energy can be used for a whole range of energies; however, a decreasing efficiency has to be taken into account.

3.4 Influence of Layer Placement Error

A large challenge during the multilayer deposition is the overall process stability. However, even during a very stable process the deposition rate is expected to change during a the deposition mainly caused by the target erosion as discussed in section 4.1. In order to

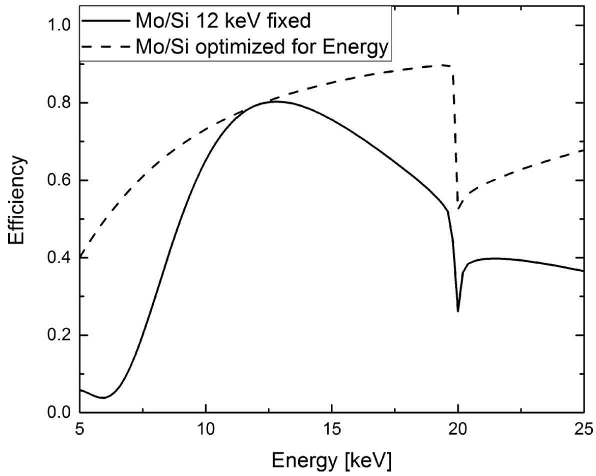

Figure 3.12: Calculated efficiency for an MLL with an optimized section thickness for 12 keV for the range of energies of 5 keV to 25 keV compared to the calculated efficiency for an MLL optimized for the respective photon energy.

quantify the influence of a defined layer placement error calculations have been made for various gradual reductions of the zone widths along the radius mimicing a gradual reduction of the deposition rate during a "virtual" deposition process. A linear decrease of the deposition rate over time was assumed. The total displacement (=difference of the last interface to the design position) was assumed to be between two different values. The smallest assumed displacement equals 10 % of the smallest zone width in the MLL of 5.8 nm. The largest displacement shall be equal to gradual decrease of the deposition rate of 1 % during the deposition process. These values equal to an absolute displacement of between 0.58 nm and ≈ 250 nm, respectively. Table 3.4 lists the layer placement errors considered for the calculations.

The calculations have been made for the MLL geometries flat, tilted, wedged as well as for two different displacement types in an FZP-like geometry. It was assumed, that the smallest zones are deposited first and inherit no error while the largest zone widths has the largest displacement. The deviations in the FZP-like structures have been made assuming a zone plate like structure with the largest zone in the center of the structure; here two types of errors have been considered. The first assuming, that a full geometry (see Figure 2.10 for reference) deposition would be deposited on a substrate and the second assuming a deposition on a "wire" type substrate, where a central substrate is used to be deposited from both sides. For the latter type of error the displacement is nonexistent in the center of the structure and present for both ends with the smallest structures. The types of errors are shown in Figure 3.13. The type of layer placement error for flat, tilted, wedged and the first type of error user for the zone plate type geometry will be called *linear* error. The second type of error for the zone plate type geometry will be called *radial* error.

In Figure 3.14 a montage of the propagation of the wave field behind the tilted lens and the two types of errors going with the zone plate like geometry with different layer placement errors are shown. A change of position for the first few calculations is barely notable. With an increasing layer placement error, however, the position of the peak intensity does move

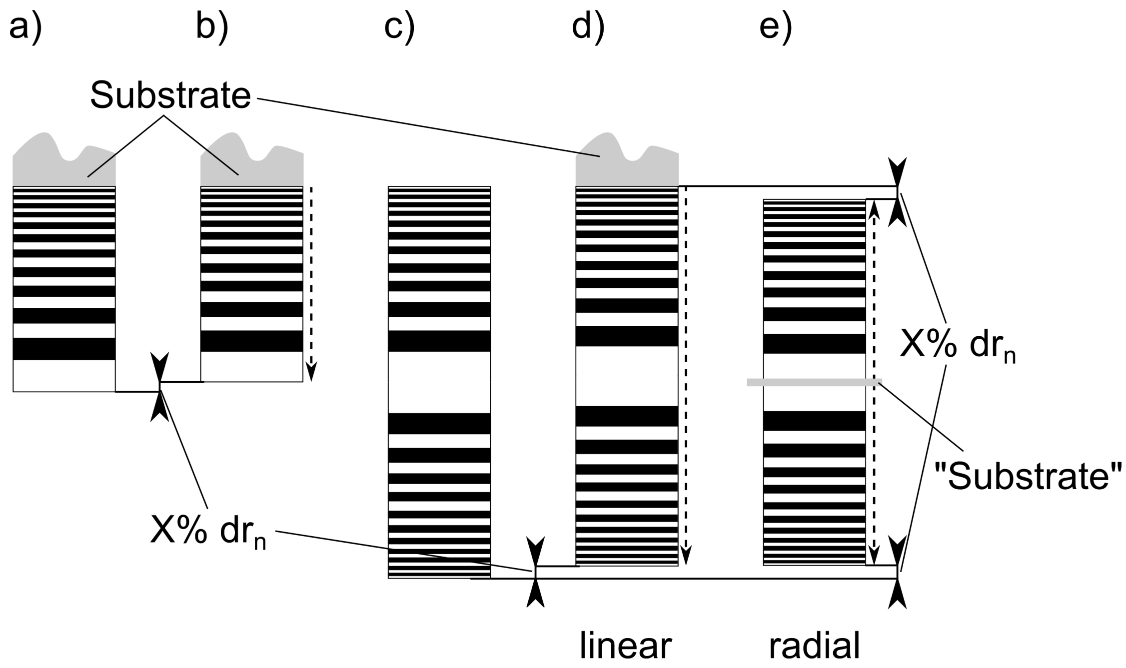

Figure 3.13: Types of layer placement errors for the flat, tilted and wedged MLL geometries as well as the full lens geometries. The dashed arrow indicates the direction of the increasing layer placement error.

perpendicular to the propagation direction of the beam as well as upstream in the propagation direction for the linear types of layer placement errors. A closer analysis also reveals, that the plane with the highest intensity is located slightly upstream of the theoretical focal plane for all layer placement errors as well as the calculation without the layer placement error. In [SKP+05] this has already been observed and connected to refraction in the lens structure. This could be of interest for high resolution wedged or curved MLLs. According to [CLQ+08] the deposition gradient has to be approximately $a(z) \approx \left(1 - \frac{z}{2f_0}\right)$ for a wedged geometry MLL. Due to the smaller effective focal length the angle of wedging needs to be adapted precisely.

The profiles of all layer placement errors for all types of geometries are shown in Figure 3.15. The intensities were normalized to the respective maximum intensity for a specific geometry and with no layer placement error.

A quantitative analysis can be done by calculating the reduction of the peak intensities of the beams propagated from the structures with different layer placement errors. The focal profile of the lens without layer placement error is used for normalization; with the increasing layer placement error the maximum intensity reduces. A reduction of less than 20 % to the maximum intensity is considered as tolerable and can still be called diffraction limited [Wel86]. This is known as the Strehl ratio. The Strehl ratios of all types of structures with the respective layer placement errors is shown in Figure 3.16 a). The Strehl ratios have been calculated by the propagation of the wave field from the lens to around the theoretical focal plane. The field of view equals $\pm 150\,\mu\mathrm{m}$ from the theoretical focal plane. From the free parameters section thickness and propagation plane the plane of maximum intensity was

Table 3.4: Layer placement error list. "rel MLL $dr_{n_{min}}$" is the displacement relative to the smallest zone width in the MLL of 5.78 nm; "rel FZP $dr_{n_{min}}$" is the displacement relative to the smallest zone width in the FZP of 17.75 nm. Drift is the assumed change of the deposition rate.

No.	rel MLL $dr_{n_{min}}$	rel FZP $dr_{n_{min}}$	Displacement [nm]	Drift [%]
1	0.00	0.00	0.00	0.000
2	0.10	0.03	0.57	0.002
3	0.25	0.08	1.44	0.005
4	0.50	0.16	2.88	0.011
5	0.75	0.24	4.32	0.017
6	1.00	0.32	5.77	0.022
7	1.50	0.49	8.65	0.034
8	2.00	0.65	11.54	0.045
9	3.00	0.98	17.31	0.068
10	4.37	1.42	25.21	0.100
11	8.74	2.84	50.42	0.200
12	13.12	4.26	75.70	0.300
13	21.86	7.10	126.13	0.500
14	32.80	10.66	189.24	0.750
15	43.73	14.21	252.32	1.000

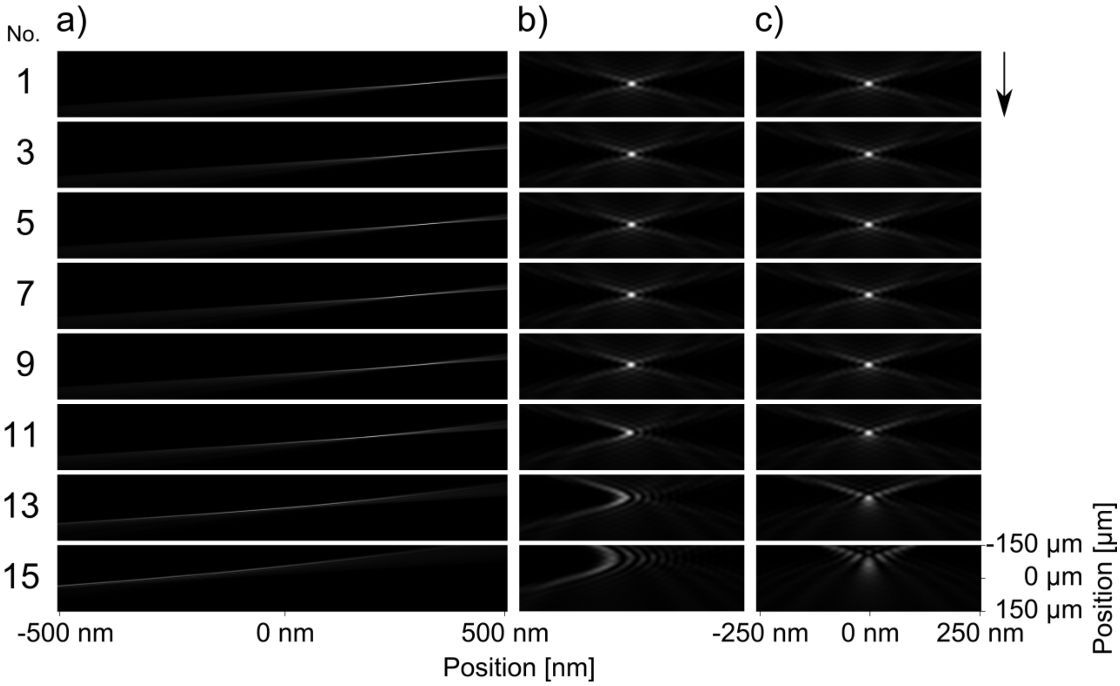

Figure 3.14: Montage of the wave field around the expected focal plane for a) a tilted MLL, b) the FZP geometry with the linear error and c) the FZP geometry with a radial error. The arrow indicates the beam propagation direction.

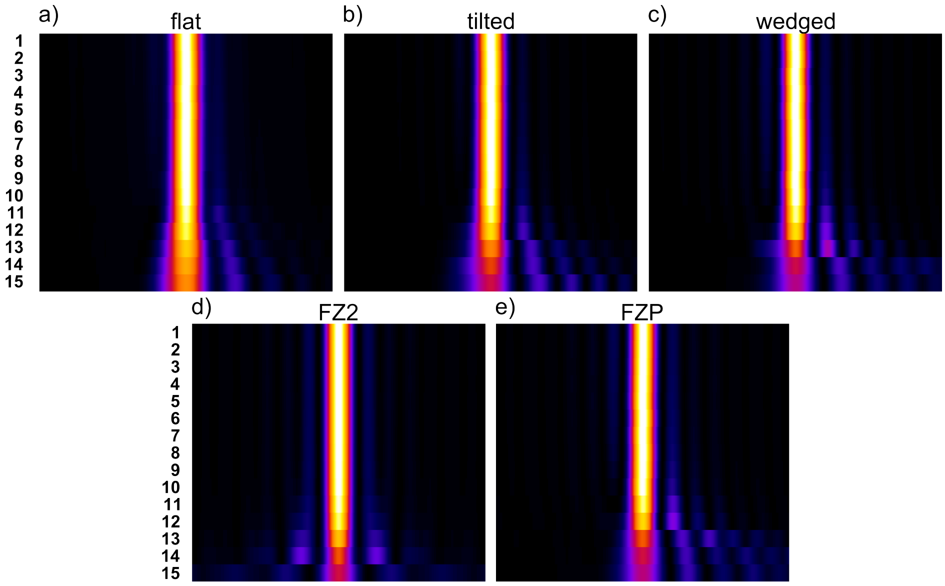

Figure 3.15: Centered profiles of the peaks with different layer placement errors for a) flat, b) tilted c) wedged d) linear type FZP e) radial type FZP layer placement error.

determined. The tolerable layer placement error for FZP has been calculated in [SM83]; it has been estimated to be approximately half the FHWM beam width. The calculations made here for MLLs suggest a more forgiving behaviour for a deviation of approximately 4 times the FWHM of the smallest beam size.

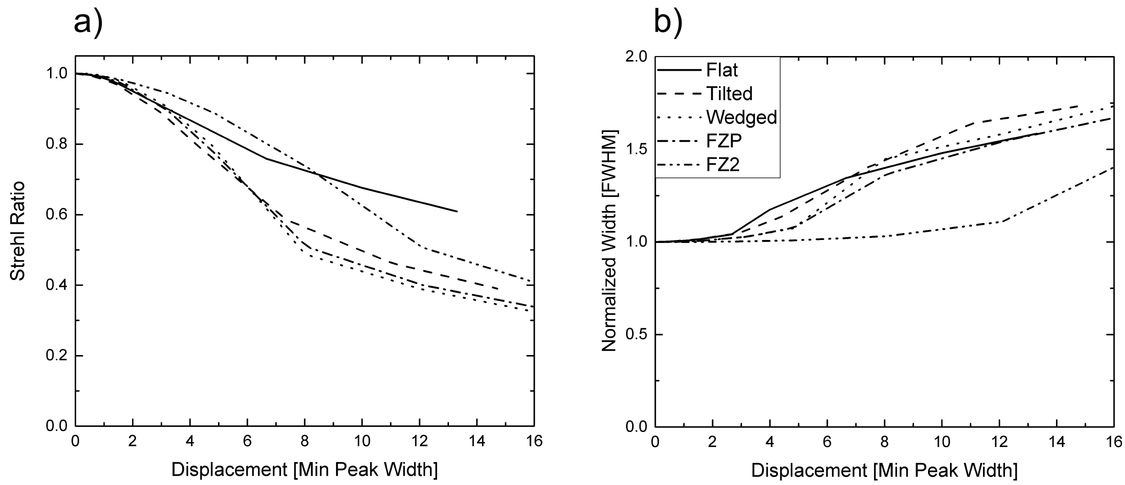

Figure 3.16: a) Strehl ratio for the considered structures as a function of the different layer placement error.
b) Normalized focal widths for the considered structures as a function of the layer placement error.

In Figure 3.17 a montage of the local efficiency maps for the various layer placement errors is shown. The calculated efficiency maps basically do not change with a relatively small layer placement error.

The calculations in this section can only be seen as an example for a quantification of the effects. An actual layer placement error will not evolve as uniformly as the underlying assump-

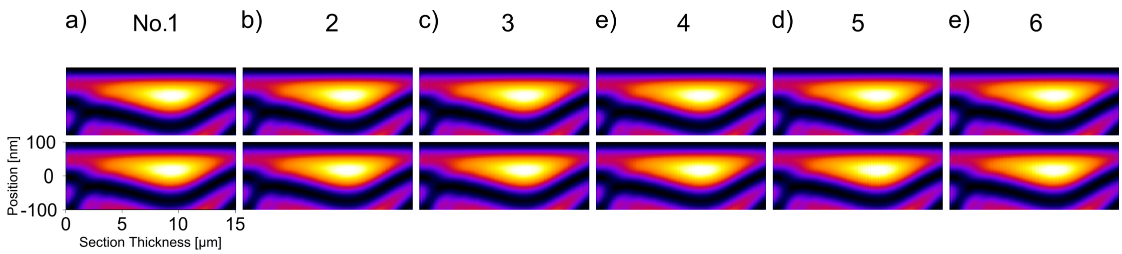

Figure 3.17: Montage of the calculated efficiency maps for the different layer placement errors. No significant change is visible in the distribution for various layer placement errors.

tion for these calculations. Real characteristics can only be calculated based on deposition data. Several publications have been published discussing various types of layer placement errors. In [LHW+14] an analysis was made how a stochastic layer placement error changes the peak intensity. Another estimation of one example was made in [YCBC14] where the focus profile of a lens with a specific layer placement error was calculated and compared to a perfect lens. In [AKB15] several types of layer placement errors of wedged MLLs are discussed.

3.5 Two-dimensional alignment

Adjusting the correct relative angle and distance of two MLLs is crucial for the beam. A calculation of the necessary precision of the perpendicular alignment was done in [YMK+08]. There the required precision was calculated to be:

$$\gamma < \frac{\lambda f_2}{2D^2} \tag{3.3}$$

With f_2 being the focal length of the downstream MLL, D the physical aperture, λ the wavelength of the X-rays and γ the relative angle. The relevant criterion is assumed to be the change of the focal distance through the coupled focusing of horizontally and vertically focusing lenses; the resulting change of the focal positions in both directions along the optical axis has to be smaller than the depth of focus. As a consequence the required angular precision for a lens with an aperture of 50 µm similar to the designs DDD20@20_50 and DDD9@15_50 is $\gamma \approx 0.01°$. In order to achieve sufficient orthogonality for the N100 design with an aperture of 102 µm with a focal length of 9.6 mm at 12 keV photon energy a precision of $\gamma \approx 0.0027°$ is necessary. In Figure 3.18 the orthogonality requirement is shown as a function of the aperture and of the diffraction limited focal spot size.

In order to quantify the required alignment precision with a second approach a different method has been chosen here, additionally. The properties of the focal spot have been calculated as a function of the relative distance of the focal planes of the individual lenses and the relative alignment angle. This is done by the direct 2D propagation of assumed wavefields of thin lenses. Due to memory restrictions practical calculations were possible with a maximum field of view if 8192×8192 pixels. In order to accommodate the full aperture

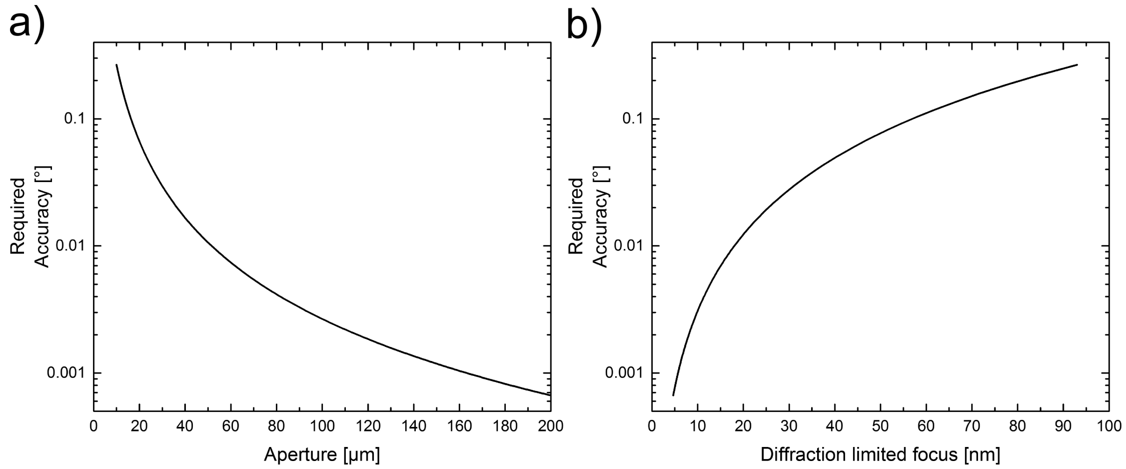

Figure 3.18: a) Angular accuracy required for a lens with a focal length of 9 mm at a photon energy of 12 keV for a range of physical apertures of 10 µm to 200 µm. b) Angular accuracy for a lens with a focal length of 9 mm at a photon energy of 12 keV with variable aperture size but as a function of the diffraction limited focal spot size.

of the lenses, the pixel size is therefore set to 10 nm and the lens occupies 5000 pixels in each direction, which results in an effective aperture of 50 µm. The pixel size is obviously significantly larger than the one used for previously discussed calculations. Therefore, it was not possible to accommodate calculations of individual zones.

The two-dimensional focusing was implemented in two steps to approximate the focusing. In a first step an aperture with the approximate dimensions of a real lens was assumed. The aperture was defined by a field with the amplitude 1 with dimension 5000 $\times$ 6000 pixels as shown in Figure 3.19 a). The phase is calculated by the assumed phase shift for a focusing wave with the designated focal length as shown in Figure 3.19 b). As compared to the MLLs considered previously the lenses are focusing on-axis and have only one focusing order. However, for most nanofocusing experiments only the properties of one focusing order are of interest. The focused intensity is evenly distributed over the whole aperture and thus can be assumed as an approximation of the local efficiency distribution of wedged MLLs.

Free space propagation was utilized in order to calculate the wave field properties at the second aperture. This aperture and the focusing are rotated with an angle of 90 °and additionally any misalignment as compared to the first lens is implemented as shown in Figure 3.19 c) and d). Ideally the focal lengths of the lenses are adapted to the propagation distance between the lenses. Deviations are deliberately included into the definition of the second lens to obtain the effect of the respective mismatches.

For the correct alignment both lenses have to be placed in the correct physical distance of the difference in focal lenghts. For the lens design considered the first lens has a focal length of 9.000 mm at 12 keV and the second lens in order has a focal lengths of 8.95 mm. Due to the difference in focal lengths of 50 µm the ideal physical distance is expected to be 50 µm. The intensities for different positions along the propagation direction are shown in Figure 3.20. For a non ideal distance between the nominal focal planes, the focal planes are separated

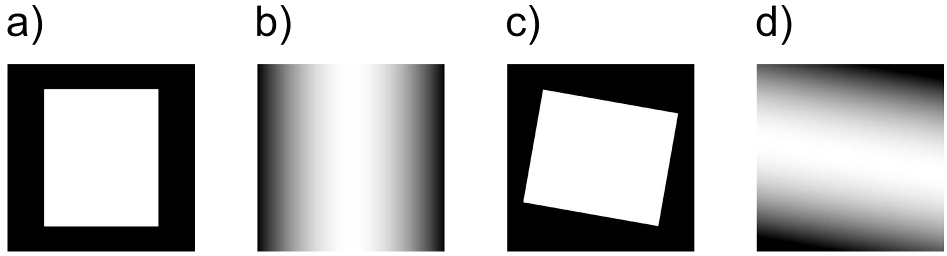

Figure 3.19: a)/c) Aperture and b)/d) phase for the first and second lens element, respectively. The deviation of the rotation angle 90° is exaggerated.

and line foci in vertical and horizontal directions can be found at two distinct propagation distances. The distance between these focal planes corresponds to the difference in the focal lengths of the lenses involved.

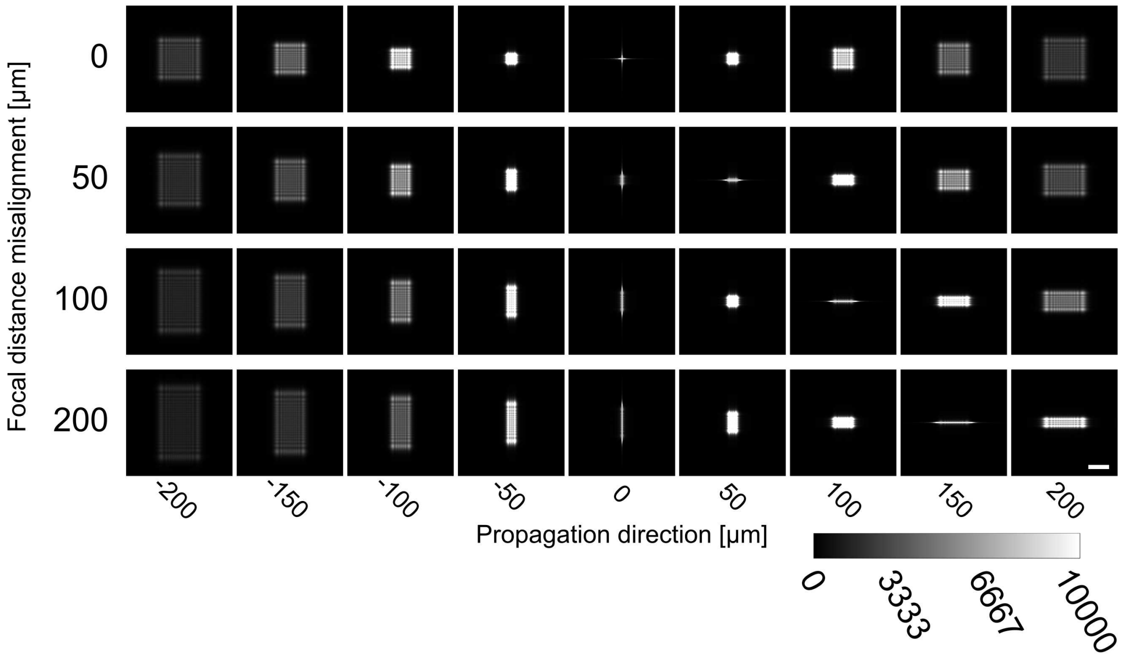

Figure 3.20: Montage of the propagated wavefield of two lenses aligned with the correct relative angle and differing distances. The number on the left gives the distance of the focal planes. The white bar in the lower right frame represents a length of 500 nm.

Assuming a correct distance between the lenses the angular alignment has to be considered next. Calculations with different deviations from the perfect alignment of 90 °are shown in Figure 3.21. The propagated wave fields show an enlarged area of intensity at the combined focal planes as compared to the perfect alignment. Additionally, a kind of apparent line focus is observed at a certain distance of the combined focal planes. The angular line focus orientation of this line changes more significantly for small deviations of the perfect alignment. For larger deviations the line is almost diagonal and the length of the focal line increases. Qualitatively these calculations have also been confirmed by raytracing simulations using RayT [KN17].

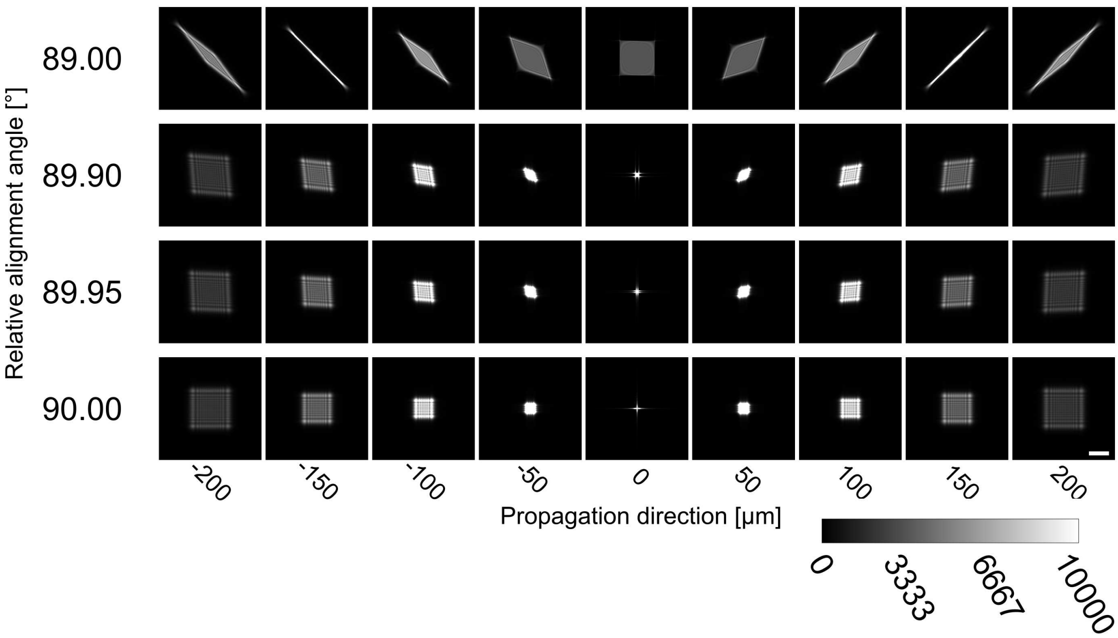

Figure 3.21: Montage of the propagated wavefield of two lenses aligned with the correct distance and differing relative angles. The number on the left gives the angle between both lenses. The white bar in the lower right frame represents a length of 500 nm.

Due to the relatively large pixel size in the calculations it is not possible to draw a detailed image of the actual focal shape with a similar accuracy as shown in [YMK+08] with this specific method. However, a quantitative analysis of the width and the maximum intensity is possible and shown in Figure 3.22 a) and b).
For this particular setup a diffraction limited alignment according to the Strehl ratio criterion of 0.8 of the maximum intensity can be achieved if the lenses are aligned with an accuracy of $\gamma \approx 0.03°$. According to equation 3.3 the necessary necessary accuracy for this setup would be $\gamma \approx 0.01°$. The order of these results is comparable and the difference is assumed to result from different criteria used to assess the tolerable deviation.
In order to show the effect of lenses not aligned well in distance and angle propagations of lenses with a fixed relative distance of 150 µm and different angles are shown in Figure 3.23. The calculations discussed here can be used to classify the type of misalignment of the lenses if the wave field of the lenses is obtained by ptychography. Additional aberrations can be expected, when the multilayer is not perfectly made and for example feature some kind of layer placement error such as the ones, that have been discussed in section 3.4. Other types of manufacturing errors could be included into the 2D calculations by mapping the respective phase and intensity effects on the 2D-aperture. Calculations showing similar beam intensity features have been published recently in [YHB+17]. The calculations presented here have been done independently.

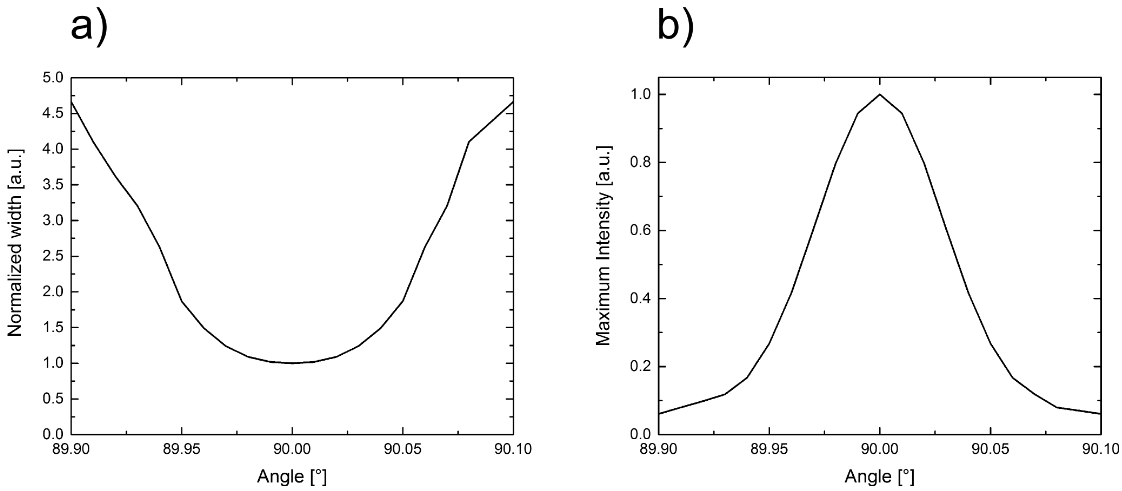

Figure 3.22: a) FWHM of the beam as a function of the relative angle of the lenses in the nominal focal plane. b) Maximum intensity as a function of the relative angle of the lenses in the nominal focal plane.

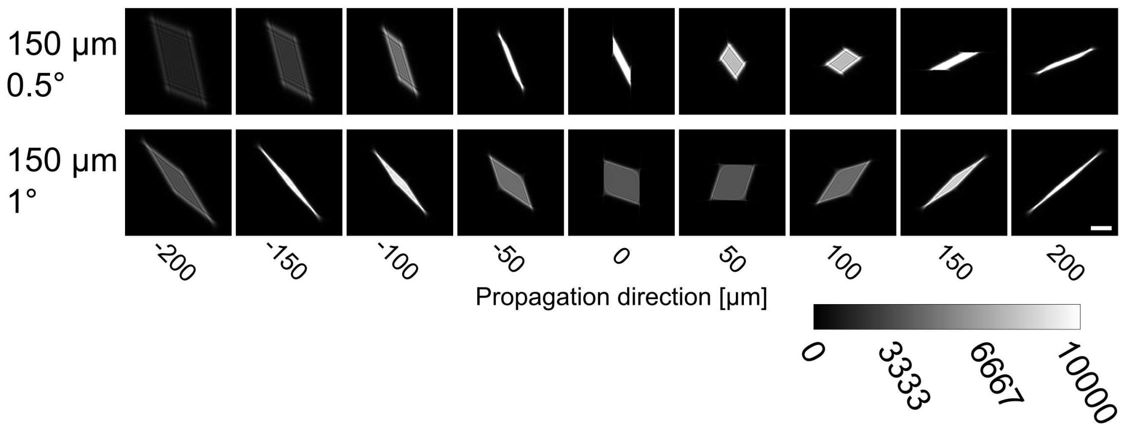

Figure 3.23: Montage of beam profiles for lenses misaligned in distance and a missalignmentof 0.5°and 1.0°. The white bar in the lower right frame represents a length of 500 nm.

3.6 Beam size and efficiency of monolithic lenses as of photon energy

In order to allow a lens to be used for a range of photon energies the pairs of MLLs have to be adapted accordingly. However, it has to be considered, that the focal length changes linearly with the photon energy for each of the lenses. Considering lenses having a different focal length of 9.000 mm and 8.995 mm at 12 keV photon energy and a physical distance of 50 µm will lead to a changing distance between the focal planes for different energies. The beam size $w(z)$ of a gaussian beam as a function of the distance from the focal plane is [Mes99]:

$$w(z) = w_0\sqrt{1+\left(\frac{z-z_0}{z_R}\right)} \text{ with } z_R = \frac{\pi w_0^2}{\lambda} \tag{3.4}$$

With w_0 being the size of the beam in the focal plane, z the position along the optical axis, z_0 the focal plane position and z_R the Rayleigh length. Considering the depth of focus it can be assumed, that a certain mismatch of the respective focal planes is tolerable. The beam size for different focal spot sizes is shown in Figure 3.24 b).

Based on this the smallest intermediate symmetric beam size of two lenses can be calculated for different relative distances of the lenses. In Figure 3.24 c) the intermediate symmetrical beam size for a pair of 15 nm diffraction limited lenses is plotted for several relative distances. A smaller relative distance is favorable in order to obtain small beam sizes even outside the immediate focal plane. If 15 nm resolution lenses are mounted in a distance of 10 µm a sub-20 nm beam can be achieved in a range of photon energies of 5 keV up to ≈ 20 keV. This is a major advantage as compared to separately mounted lenses where the lenses have to be realigned in terms of their relative distance for each energy [YRS+11].

However, this approach is only suited down to intermediate resolutions in the order of ≈ 10 nm. For lenses with diffraction limited focal spot sizes significantly smaller the depth of focus is too short in order to cover a range of photon energies with a reasonable resolution.

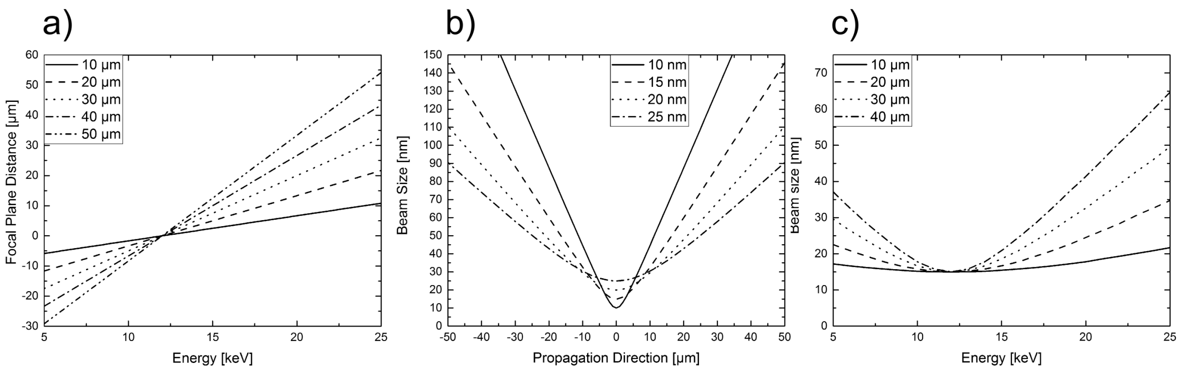

Figure 3.24: a) Beam size as a function of the distance of the focal plane for given diffraction limited focal spot sizes. b) Resulting smallest symmetrical beam sizes as a function of the energy for different relative distances of the lenses. This assumes a 15 nm focal spot size and optimized lenses at 12 keV base energy.

3.7 Three material multilayer Laue lens calculations

The residual stress in MLL depositions poses a limitations in terms of the growth thickness. It is therefore necessary to find solutions to reduce this stress. The discussion of this system is discussed more in depth in section 4.1.

Calculations have been made for a three material system based on the materials Mo, Si and $MoSi_2$, which is identified as a promising approach in terms of stress reduction. The results have been published in [KBG+16] and will be discussed here shortly. Due to the absorption properties of $MoSi_2$ the calculated efficiencies for Mo/$MoSi_2$/Si with a large share of $MoSi_2$ is significantly lower than for small thicknesses of $MoSi_2$. The expected diffraction efficiency is very comparable to the ones, where the only pure molybdenum is used as absorber, if the transition layer is kept thin.

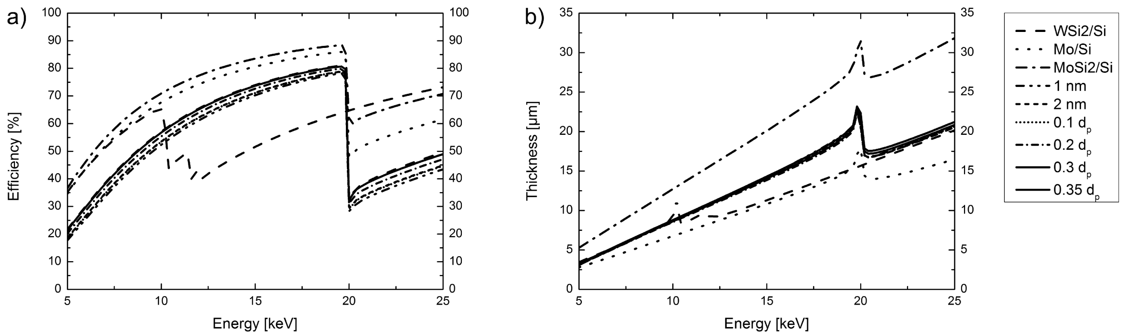

Figure 3.25: Calculated efficiencies of the three-material-system with various transit layer thickness as well as several two-material-systems. Figure 1 from [KBG+16].

3.8 Influence of varied relative absorber and spacer material thicknesses on the diffraction efficiency

The variation of the relative absorber and spacer material thicknesses can have a significant impact on the diffraction efficiency. For multilayer systems Γ is used to describe this property; Γ gives the part of the period occupied by the more absorbing material. Here calculations for Γ between 0.1 and 0.9 have been considered for absorber materials Mo and WSi_2. These calculations were performed with a CWT algorithm [MS92]. Discussions of some manufacturing implications can be found in section 4.1.

The calculations have been done for a wedged lens with a focal length of 4.5 mm and a smallest zone width of 2 nm.

In Figure 3.26 the results of the calculations for the Mo/Si combination are shown. Subfigures a) and b) show the expected efficiency and the necessary section thickness for a ratio of the absorption layer in a period Γ between 0.1 and 0.9. Subfigures c) and d) show the efficiency and necessary section thickness for three distinct photon energies above and below the molybdenum K-edge. The calculations show that for energies below the molybdenum-K absorption edge the Γ ratio has only limited impact on the diffraction efficiency for a Γ between approximately 0.1 and 0.6. However, the optimum section thickness increases significantly for smaller Γ. A larger difference in the diffraction efficiency can be observed for energies above the absorption edge.

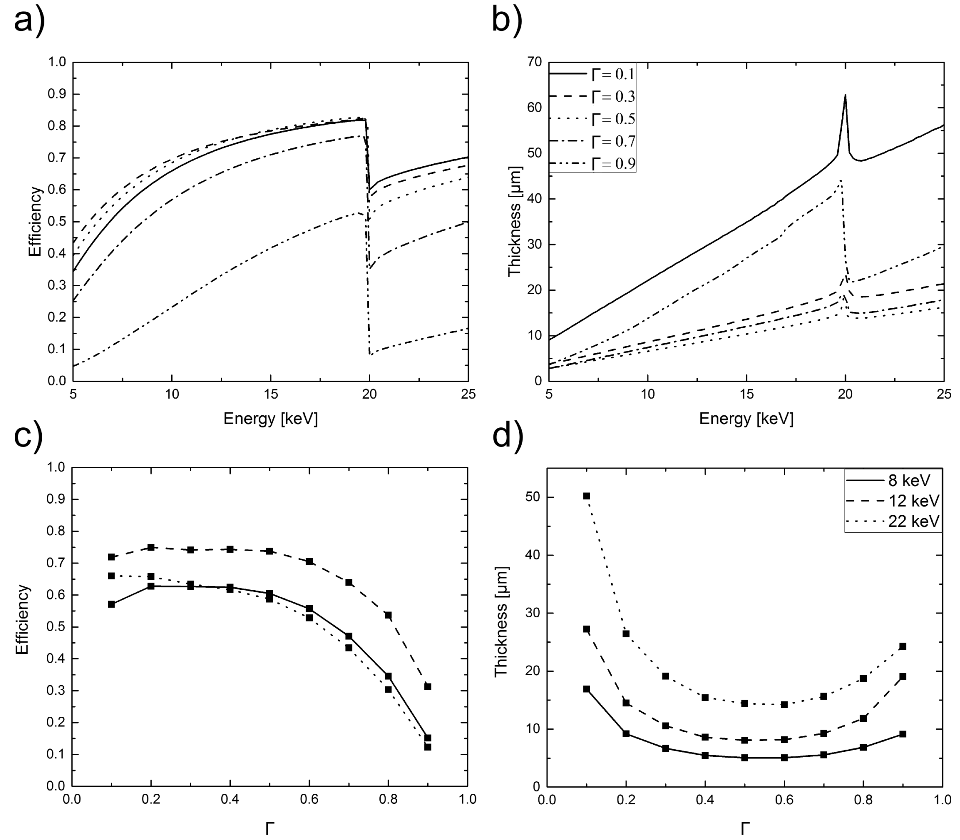

Figure 3.26: a) Efficiency as a function of the photon energy for several Γ-ratios for a Mo/Si system
b) Section thickness for the optimum efficiency in a)
c) Efficiency for different Γ for three distinct energies for a Mo/Si system
d) Optimal section thickness for the lenses calculated in c).

In Figure 3.27 the results of the calculations for the WSi_2/Si combination are shown.
The calculations show, that the optimal Γ is not necessarily 0.5. Generally the optimum section thickness increases with difference from $\Gamma = 0.5$ and particular $\Gamma < 0.5$ is of interest due to the negligible influence to the diffraction efficiency. Larger section thicknesses have been stated as being beneficial for the sectioning process in [YCBC14]. On the other hand smaller section thicknesses might be favorable for making stress optimized MLLs.

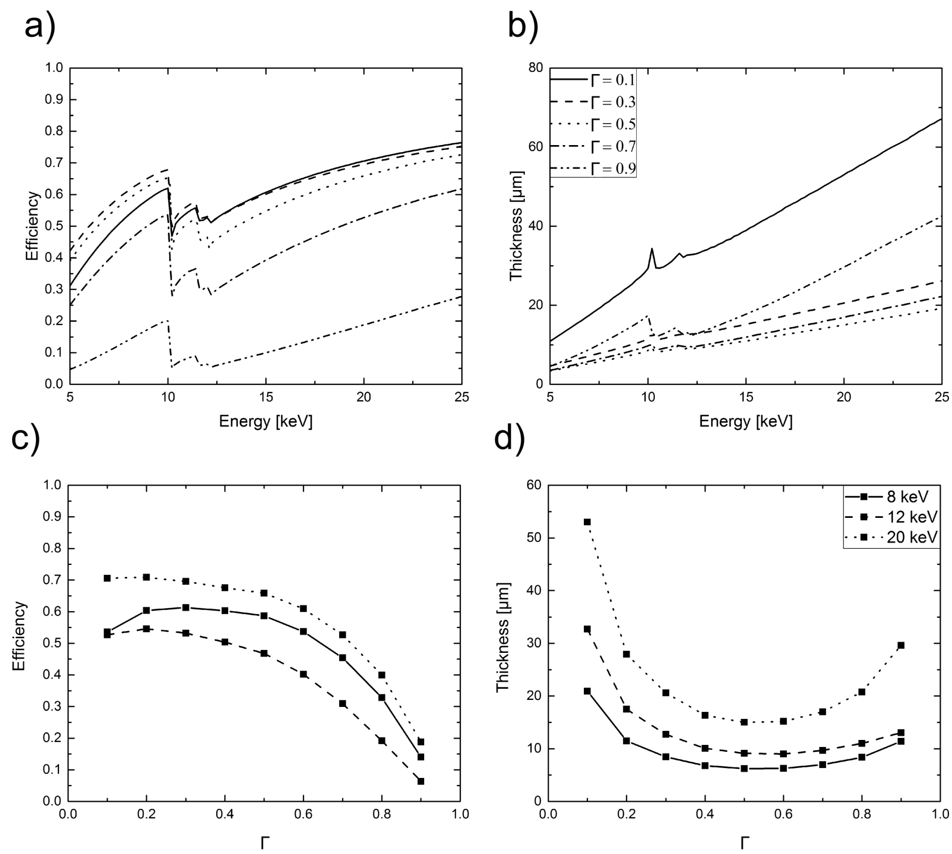

Figure 3.27: a) Efficiency as a function of the photon energy for different Γ-ratios for a WSi_2/Si system
b) Section thickness for the optimum efficiency in a)
c) Efficiency for different Γ for three distinct energies for a WSi_2/Si system
d) Optimal section thickness for the lenses calculated in c).

4 Manufacturing

The manufacturing process of MLL consists of three steps in general: multilayer deposition, sectioning and alignment of the lenses. All three steps have specific challenges, which have to be overcome in order to make a diffraction limited MLL. In section 3 it has been shown, that high precision is necessary:
A precise deposition according to the zone plate law is crucial for optimal diffraction efficiencies while the correct relative alignment of the lenses ensures an optimally focusing phase.

4.1 Multilayer Stack Deposition

The first step in the manufacturing process of an MLL is the deposition process of the respective multilayer stack. Several thin film deposition methods have been used so far for the fabrication of diffractive transmission optics: Magnetron Sputter Deposition (MSD), Atomic Layer Deposition (ALD), Pulsed Laser Deposition (PLD) [CBB+09, KRM+14, EODK15]. MSD [KA00] is the most preferential coating technique for MLL depositions it features:

- smooth layers on smooth substrate for suitable materials
- acceptable deposition rates
- good process stability
- precise thickness control
- good repeatability

Due to the large full stack height one deposition process still can last from several days up to two weeks. During this time the process has to be stable. Furthermore, due to inevitable changes of some components involved in the process it has to be iteratively adjusted to achieve the desired accuracy for such a long deposition. Once the desired accuracy has been reached in one deposition a large number of individual lenses can be made from this particular run. This is due to the large covered area of the multilayer deposition.
The MLL coatings fabricated in the scope of this thesis were made in a rotary MSD machine made by PINK GmbH. The MSD chamber has a square footprint and the four magnetrons are located in the respective corners as shown in Figure 4.1. They are oriented with the deposition direction facing up. The planetary substrate motion consists of the spin motion around the axis of the substrate center which is held constant and the speed of the circular motion around the center of the chamber. This speed can be varied to achieve a desired film thickness and thickness profile due to different coating times. The chamber is part of a

machine that features an additional storage space for two substrate carriers, a load lock, a handler and a PLD module. Standard deposition conditions in the MSD module are:

- Vacuum base pressure: $< 1 \cdot 10^{-7}$ mbar
- Argon working pressure: $1 - 1.5 \cdot 10^{-3}$ mbar
- Magnetron source power: $50 - 400$ W
- Voltages: 200 V to 700 V
- Target dimensions: 304.8 mm × 88.9 mm × 6.35 mm
- Angular frequency: $f_\Omega = 0.2 - 4$ rpm
- Spin frequency: $f_S = 0.5 - 5$ Hz

A detailed description of the machine can be found in [BMM+02].

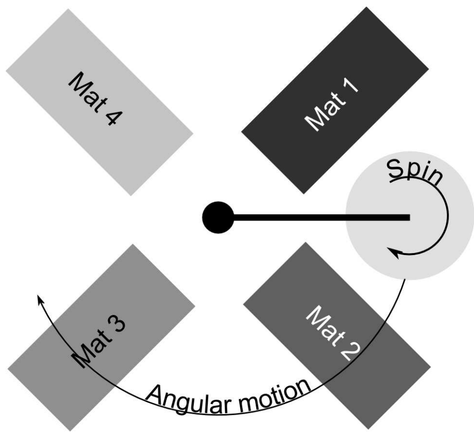

Figure 4.1: Scheme of the planetary motion geometry in the MSD machine in top view. The substrate is facing down; magnetron sputtering is facing up.

Deposition

The deposition process takes place within a vacuum environment, with residual gas constituents of $< 1 \cdot 10^{-7}$ mbar. Additionally, Argon is introduced into the chamber as sputter gas. A voltage is applied between the anode and cathode. Due to ionization processes of the sputter gas a plasma emerges and the ions are accelerated towards the cathode with the target material. The bombardment induces collision cascades and target material particles leave the bulk. This process is called sputtering. The particles sputtered from the target cross the plasma region and condense on the substrate surface. This results in the formation of the desired thin film.
Due to the constant sputtering process the thickness of the deposited layer is a function of the time the substrate spends over the magnetron. A more detailed description can be found in [Bra04].

Preparation and Deposition

The deposition of the MLL lens stack with individual thicknesses is the most challenging part of the manufacturing process. A multilayer stack has to be deposited very precisely; acceptable deviations from the design are small as discussed in section 3.4.
For the deposition of an MLL stack a precise knowledge of the deposition rate is necessary. The deposition rate for each of the materials has to be determined individually in order to calculate the necessary angular frequencies f_Ω of the substrate carrier in the respective areas in the deposition chamber.
The deposition rate of a material can be determined by the deposition of a simple multilayer stack, which has to be comprised of two different multilayers; for one of the materials the angular frequency and thus the time spent over one of the magnetrons has to be changed. The resulting multilayer stack has two distinct bilayer thicknesses as shown in the scheme in Figure 4.2 a). The thickness of these stacks can be measured using X-ray reflectometry (XRR) [KvB01]. A reflectivity measurement for one periodic multilayer stack is shown in Figure 4.2 b). An additional set of Bragg peaks would be present in case of two distinct thicknesses.
A Bragg peak analysis allows to calculate the layer thicknesses. The reflectivity data consists of two sets of Bragg peaks, which emerge from the different multilayer thicknesses. All peaks have to be matched to the corresponding (thinner/thicker) stack . The measured difference in the multilayer thicknesses is used to calculate the effective deposition rate of the respective material:

$$kc = \frac{\Delta D}{1/f_{\Omega 1} - 1/f_{\Omega 2}} \tag{4.1}$$

kc is the deposition rate, $f_{\Omega 1}$ and $f_{\Omega 2}$ the angular frequencies used and ΔD the difference in thicknesses between the two multilayer stacks.
This is repeated for all relevant materials. The deposition rates are used to determine the expected multilayer thickness according to the calculated deposition rates. This expected multilayer thickness will often differ from what has been actually measured. This difference is due to the contraction between different neighboring materials and the contraction can differ for different materials combination and sequences [BFvL$^+$03]. This difference is assumed to be independent from the actual multilayer thickness.

Layer placement error

The accuracy of the layer thicknesses throughout the deposited stack is an important aspect. Though the initial deposition rate can be determined very accurately it will change over time caused mainly by the sputter target erosion. For a deposition process of a few hours the effects of a rate change are usually negligible. However, for a process lasting up to hundreds of hours this has to be taken into account. Usually the change in the deposition rate is not known beforehand for a specific setup and it is also specific to the deposition targets and the overall geometry of the machine. The rate change causes layer thicknesses to differ from

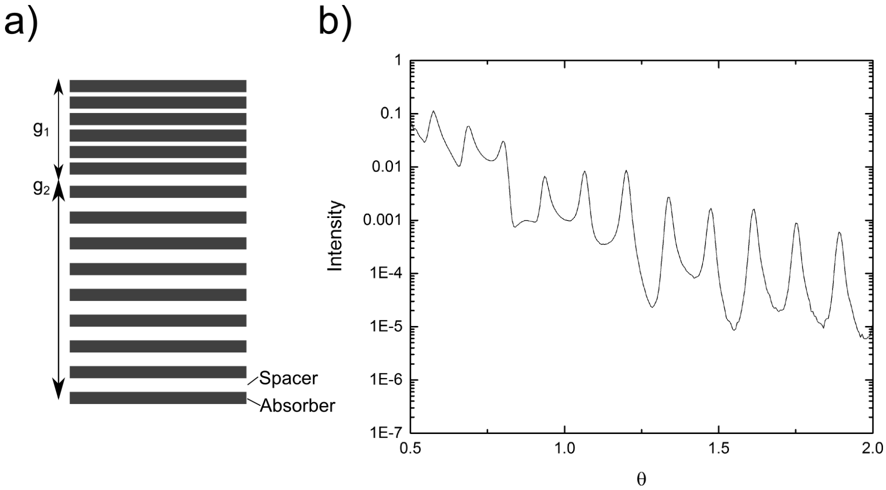

Figure 4.2: a) Scheme of a stack with two different period thicknesses, where the absorber has a constant thickness.
b) Reflectivity of one periodic multilayer stack with distinct Bragg peaks; two different periodic multilayer stacks would result in an additional set of Bragg peaks in superposition.

the intended design, if it is not compensated for. If the thicknesses of individual layers do not correspond to the design the subsequently deposited parts of the stack will inherit an accumulated layer placement error, i.e. their position on the radius will not correspond to the design according to the zone plate law. Calculations showing the impact of a layer placement error can be found in section 3.4.

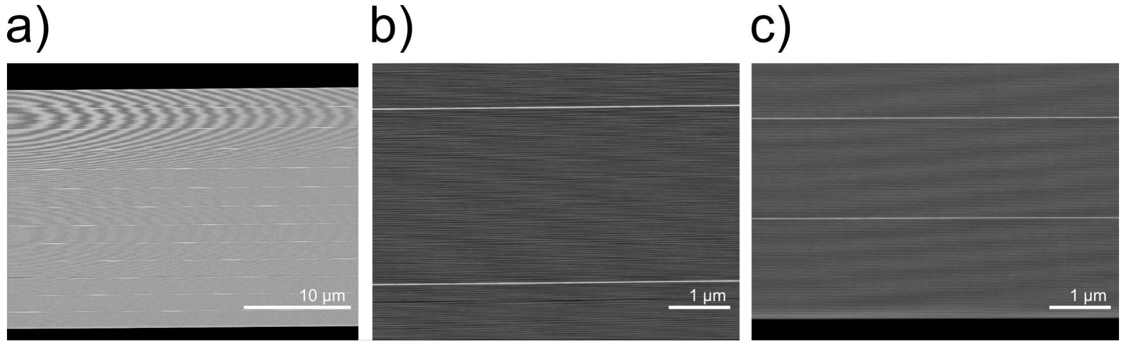

Figure 4.3: a) SEM image of MLL cross section with visible marker layers.
b) The two neighboring marker layers with the largest gap.
c) The two neighboring marker layers with the smallest gap and lower surface.

The characteristic of the rate change has to be known in order to adapt the frequency of the angular motion throughout the deposition process. However, currently these changes can only be determined experimentally ex-situ and this information has to be fed back iteratively into the deposition process to obtain the necessary precision. These measurements are done with a cross section analysis by means of FIB and SEM. Ideally the period thicknesses would be measured for the whole stack. Due to the small field of view of the SEM measurements

in high resolution mode a series of separate images has to be made to cover all the deposited layers.
Additionally, in order to obtain a positioning aid marker layers have been proposed [CBZ+12]. A marker layer is a layer, which is made of one of the materials in the stack but has a thickness, corresponding to its own regular thickness and additionally one or more periods; it substitutes one or several periods. In a regular two-material system (e.g. Mo/Si) one marker layer usually has a thickness of three zones combined.
The marker layer do not change the overall diffraction properties of the stack if their thickness is properly calibrated as the multilayer stack is interrupted only locally. However, their thickness makes them visible as a distinct feature in the SEM images and enables to determine their relative distance. This distance is compared to the distance according to the deposition design. Figure 4.3 a) shows an SEM image of a multilayer stack with incorporated marker layers; Figure 4.3 b) and c) show images of two positions on such a stack: the first in the stack and the second at one of the surfaces, respectively.
The individual period thicknesses can be evaluated based on the gray value line plot. Due to the still limited resolution of the SEM images, as only a few pixels per period length are present, the statistical error for evaluated single period thicknesses is several percent. It is therefore useful to evaluate averaged layer thicknesses over a certain distance. The measured thicknesses is then compared to the design thicknesses. The example of such an evaluation is shown in Figure 4.4.

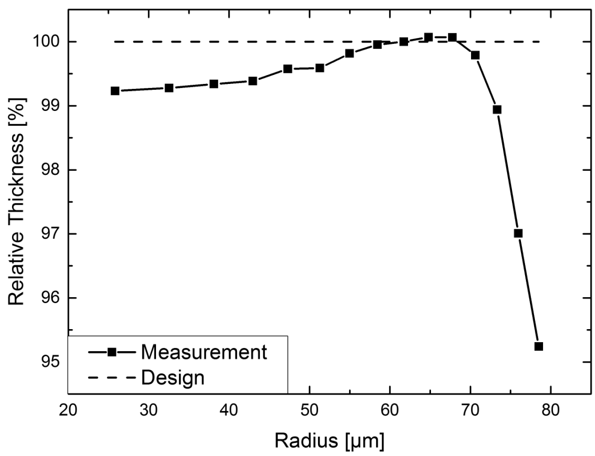

Figure 4.4: Measured layer placement error of an MLL. The parts of the lens representing larger radii have a significant deviation from the ideal thicknesses.

Residual Stress in MLL Structures/Thickness limitations

For focusing applications using X-rays a large aperture optical element is desired in order to achieve the best possible resolutions. For MLLs the aperture is synonymous with a corresponding thick deposition of the respective multilayer stack. Depending on the X-ray source

setup different aperture sizes might be necessary to make use of a significant part of the coherent flux.
The end stations of modern synchrotron radiation sources have a lateral coherence length in the order of 100 µm [MCD+11]. Considering this, the first experiments aiming for a large aperture transmission diffraction optical element based on thin film technology, a first predecessors of an MLL had an aperture of approximately 20 µm [KSL+04]. At that time this was considered a very large deposition thickness.
Recently deposition thicknesses of around 50 µm [YRS+11, KBN+14a] and even more than 100 µm have been reported [MKC+15]. Obtaining a deposition thicknesses in the order of 40 µm can be achieved by modern deposition processes without major obstacles [Bra17, Yan13, Bou15]. Significantly larger deposition thicknesses impose challenges especially due to the residual stress in the multilayer stack. Residual stress bends the substrate and at some point the bending can cause cracking and breaking of the substrate during the deposition. This was experienced several times during depositions for this thesis and also been reported by another group [Bou15]. Therefore, it seems natural to aim for the reduction of the residual stress.
Several approaches have been discussed and published to push the thickness barrier to larger deposition thicknesses. Some methods are briefly discussed in the following.
Standard sputter atmosphere consists of Argon and the residual gas in the deposition chamber. Reactive sputtering was tested to reduce layer stress in Mo/Si multilayer stacks [Win07]. This has been adopted in order to be used for the deposition of MLL by Conley et al.; additionally reactive nitrogen gas was added to the process [CBZ+12].
The impact of the variation of the relative thicknesses of absorber and spacer on the residual stress of the whole multilayer stack was discussed in [SMM+14]. For the material combination $MoSi_2$/Si the materials have tensile and compressive stress respectively. If the ratio of the absorber thickness to the period thickness Γ is changed residual stress can be significantly reduced as discussed in [SMM+14]. A challenge of this approach is, that the optimal Γ changes as a function of the bilayer thickness [Mas17]. However, a disadvantage of this method is the required increase of Γ for standard material combinations such as Mo/Si and W/Si in order to reduce the residual stress. This increase of the absorber material thickness leads to a reduced diffraction efficiency which reduces the maximum diffraction efficiency. Calculations on lenses with several Γ are discussed in section 3.8. For an optimal residual stress configuration Γ would have to be changed gradually throughout the stack. This would result in a *multi*-Γ lens, which has been proposed in [ZHLW11]; however no efficiency calculations for such a combination have been published, yet. If residual stress limitations are set aside this could also be used in order to manufacture a lens with a more optimized diffraction efficiency.
A successful approach was developed at BNL [MKC+15]: Compared to previous MLL a different material compound has been used: WSi_2 and aluminum with doping of about 5 % silicon to obtain preferential properties for the layer roughness. The use of aluminum instead of silicon reduces residual stress while the X-ray optical properties are changed only in the order of 10% as shown in Figure 4.5.

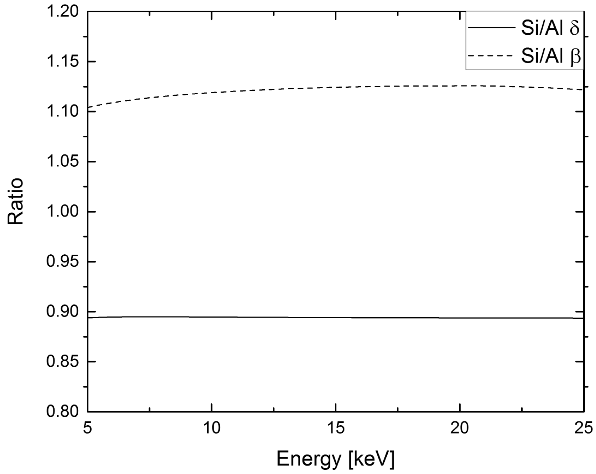

Figure 4.5: Relative comparison of δ and β for aluminum and silicon.

Three material system

The approach to reduce the residual stress used in the scope of this thesis is discussed in the following. This approach has been described in [BKG+15].

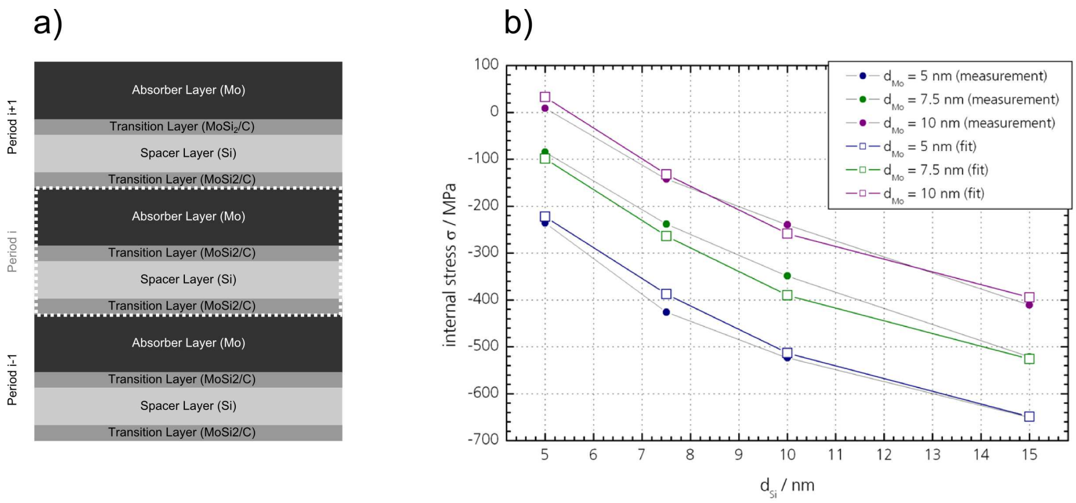

Figure 4.6: a) Scheme of the three material MLL multilayer system.
b) Measured residual stress as a function of Mo and Si thicknesses. Figure 4 from [BKG+15].

Most materials, which have been used regularly for MLLs form amorphous structures. Amorphous structures are mostly known to feature compressive stress. A desirable way would be to introduce materials with a tensile stress component to the multilayer system in order to balance compressive and tensile stress locally. Silicon brings the largest contribution to the compressive stress to the system. Therefore, replacing silicon with a different material with less or no compressive stress would be desirable.

Nano-crystalline structures represent an alternative as they feature tensile stress. Aluminum or boron – due to their favorable X-ray properties – would be viable materials to be used as spacer layers. However, due to the chemical reactivity of boron only aluminum should be considered. Pure aluminum has the disadvantage of showing a layer roughness of more than 1 nm for relevant layer thicknesses. This makes it unfeasible for making precise thin film layers, where the roughness has a large negative impact on the optical properties of the multilayer system [Yan09].

A different path are metallic materials with a higher atomic number to replace the absorber. Due to similar X-ray optical properties to the silicides pure molybdenum and tungsten appear to be reasonable choices. The properties are comparable to their respective silicides for relevant photon energies leading to very similar efficiencies and smaller optimal section thicknesses.

Completely stress free multilayers have been demonstrated using combinations of Mo/Si and W/Si [Win00] and both bilayer systems have been used successfully to manufacture MLLs [TIO+09]. Out of these two absorber materials molybdenum has the better trade-off in efficiencies and properties for X-ray photon energies up to approximately 20 keV. However efficiency calculations show, that the necessary low-stress absorber-spacer ratio seemed to be unfavorable. Compared to the spacer thickness a significantly thicker absorber is necessary. This significantly reduces the achievable efficiency as discussed in section 3.8).

Therefore, an approach on adding a transition layer between the “regular” absorber and spacer materials between the respective interfaces in the multilayer structure has been developed. The structure of such a multilayer is shown in Figure 4.6 a).

It is therefore necessary to chose a material, which prevents interdiffusion of its neighboring materials. The two candidates, that have first and foremost been taken into account are $MoSi_2$ and C. Extensive tests have been made using $MoSi_2$ as the spacer material. Several sets of multilayers with different thicknesses have been made.

The residual stress was measured for different periodicities and designs of the multilayer systems. Molybdenum and silicon were considered as the main contributors of the stress and change of the $MoSi_2$ thickness showed virtually no difference in the external stress of the multilayer system. Thus, the systematic measurements were focused on thickness variations of Mo and Si.

The residual stress is measured in units of pressure (Pa). Typical values for residual stress are up to several hundred Megapascal. The stress measurements were done with laser deflection measurements. An FLX 2320 by Toho Technology Cooperation was used to carry out the measurements. The position of a reflected laser beam is measured by a diode and based on this laser positions on the diode the curvature of the surface is determined. The residual stress σ of a thin layer can be derived from this curvature according to the Stoney equation [Son09]:

$$\sigma = \frac{E_s h_s^2}{6(1-\nu_s) d_{\text{layer}}} \left(\frac{1}{R_0} - \frac{1}{R_1} \right) \tag{4.2}$$

E_s being the Youngs modulus of the substrate, h_s the substrate thickness, ν_s Poisson’s ratio, d_{layer} the layer thickness, R_0 the radius of curvature of the substrate without coating and R_1 the radius of the curvatrue of the substrate with the coating. The measured residual stress as a function of the Mo and Si thicknesses is shown in Figure 4.6 b).

As the contribution of $MoSi_2$ towards the total stress of the multilayer, even with differing

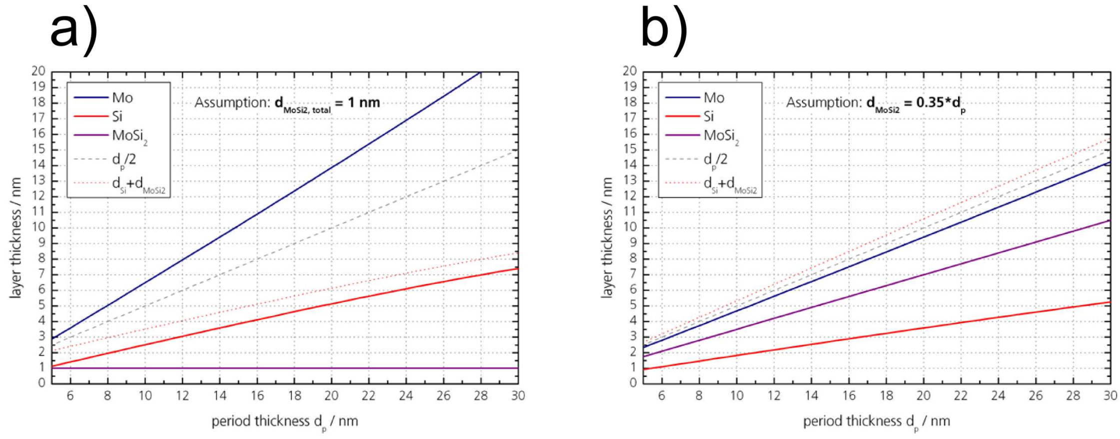

Figure 4.7: Individual layer thicknesses with different given $MoSi_2$ thicknesses for stress free multilayer stack:
a) 1 nm and
b) 0.35· d_p
Figure 6 in [BKG+15].

thicknesses, has shown to be negligible its impact on the residual stress has not been taken into account for further considerations. Based on these measurements the prerequisite for a stress free system can be calculated:

$$d_{Mo} = \frac{g - d_{MoSi_2}}{1+c} \text{ and } d_{Si} = c \cdot d_{Mo} \text{ with } c = -\frac{p}{2} + \sqrt{\frac{p^2}{4} - q} \tag{4.3}$$

with

$$p = \frac{b_{Mo} + b_{Si}}{a_{Si}(g - d_{MoSi_2} + b_{Si})} \text{ and } \frac{a_{Mo}(g - d_{MoSi_2}) + b_{Mo}}{a_{Si}(g - d_{MoSi_2}) + b_{Si}} \tag{4.4}$$

a_{Mo}, b_{Mo}, a_{Si} and a_{Si} are the fitting parameter obtained from the quadratic fits in Figure 4.6 b), d_{Mo}, d_{Si} and g are the thicknesses of molybdenum, silicon and the period, respectively. The resulting required thicknesses for stress free multilayer configurations as a function of the period thickness for a constant transition layer thickness and a transition layer thickness relative to the period thickness are plotted in Figure 4.7. Graphs are shown for several thicknesses of $MoSi_2$ as the barrier material. The expected efficiencies of different configurations of the three-material system have been calculated using the BPM discussed in section 3.25. It is not necessary to achieve an absolute stress free system. A trade-off in terms of relative layer thicknesses has to be found for optimal performance and optimal deposition properties. During the work on this thesis $MoSi_2$ has been replaced by carbon for later depositions due to lower absorption. General considerations discussed above for $MoSi_2$ also apply for carbon. In terms of X-ray optical properties carbon features less absorption than silicon and has similarly low interdiffusion with both, silicon and molybdenum as its neighboring layer. However, the deposition rate is significantly lower than compared to silicon, which makes it unfeasible from a practical point of view to act as the main spacer layer itself. With Mo/C/Si/C a maximum deposition thickness of 90 µm has been reached.

4.2 Structuring

Subsequently to the deposition process it is necessary to manufacture individual lenses from the coated wafer. The actual lens element is a structure, which is made up by a small part of the coating. Typical dimensions of an MLL lamella are: the multilayer stack thickness as a height, twice as wide as the height and depending on the material and desired photon energy and a section thickness of single digit micrometer up to several ten micrometers.

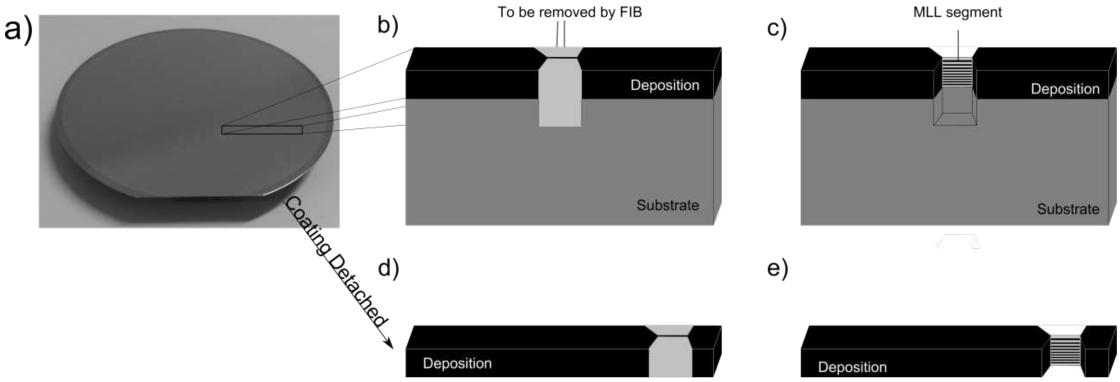

Figure 4.8: a) 150 mm silicon substrate with deposition.
b) Cut out stripe with highlighted volume to be removed by FIB milling and c) final shape of the bar with the MLL segment in the center.
d) Similar scheme for a coating detached from the substrate and e) final shape of the MLL.

For a crossed lens the structured part has to be sufficiently wide in order to allow full overlap between the width of the first lens with the width of the second lens.
Except for the one MLL made at BNL all lenses discussed in this thesis have been proposed with either laser sectioning or wafer saw sectioning. The wafer saw was used to cut stripes; afterwards a TEM H-bar type lamella has been milled into this stripe by FIB milling. The general procedure is shown in Figure 4.8 a)-c). A more elaborate discussion and description can be found in [Nie15].
For lenses made in later stages a different approach has been chosen. The deposition was mechanically detached from the substrate. Subsequently, rough sectioning was done by laser cutting before FIB milling was used to obtain the final dimensions of the lens [KMF$^+$17]. Figures 4.8 d)-e) show the modified geometry of the bar and the final lamella.
For rough FIB milling a maximum ion current of 90 nA was used. Finer milling is done with 50 nA and fine polishing using a current of 30 nA and finally 10 nA is used for the finishing. Figure 4.9 a)-b) shows SEM images of a detached and laser cut coating before and after the FIB milling process. Stress might be introduced by the laser structuring due to the heat influence zone or due to the gallium treatment in the FIB machine. For this geometry

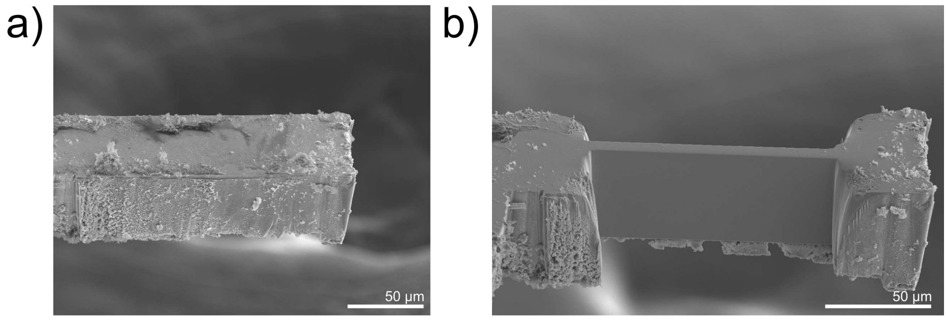

Figure 4.9: Sectioning approach in photographs: a) Tip before FIB milling.
b) Tip after FIB milling.

of freestanding MLL structure it was found, that the “dog bone” structure as shown in Figure 4.9 is preferential as compared to a pencil type structure in terms of stability as shown in Figure 5.14 b) and c). Residual stress in the stack may cause distortions and a bending of the MLL, which has been experienced in the first MLL experiments using free standing MLL ([KMF+17] and section 5.4).
Additional characterization can be done in an Xradia NanoXCT-100. Here the transmission through the lens is acquired and Bragg diffraction effects in particular can be observed. This is advantageous in order to find enclosed droplets or small cracks, that remain invisible in the SEM measurements as well as other effects in the lens such as residual bending. Figure 4.10 shows a stitched X-ray transmission image of an MLL acquired in the Xradia NanoXCT-100.

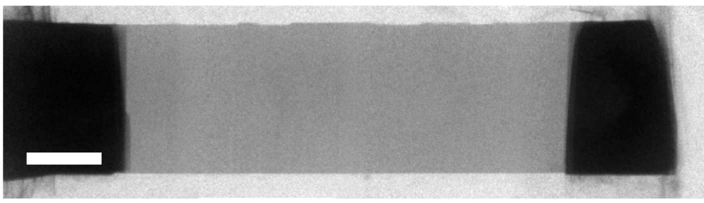

Figure 4.10: Transmission X-ray microscope image of one of the manufactured MLL acquired in the Xradia NanoXCT-100. The white bar represents a length of 25 µm. (Image courtesy of Dr. Jürgen Gluch, Fraunhofer IKTS)

Wedged MLL fabrication

An advantage of the MLL approach as compared to FZP is the possibility, that the large section thickness can be used to exploit dynamical diffraction effects. For typical MLL section thicknesses relevant zone widths start below 10 nm. The Darwin-width – the width of the rocking curve – of the Bragg diffraction decreases with increasing optical thickness. For MLL the effect of the dynamical diffraction effects have been calculated e.g. in [KIT+08].
The most straightforward way to achieve a higher total diffraction efficiency this is to tilt a parallel interface MLL. If tilted to the right angle this will engage Bragg reflection in a part of the lens structure. To improve the diffraction efficiency more advanced geometries –

wedged or curved – have to be used. So far two main approaches have been discussed to manufacture wedged MLL.

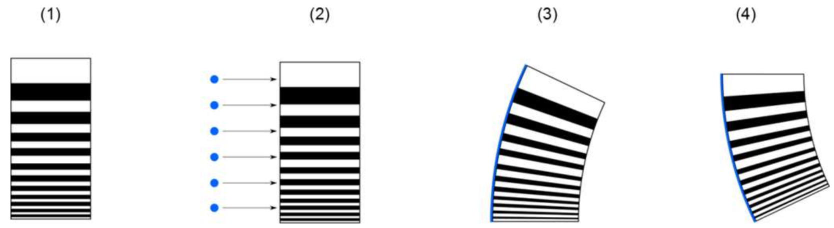

Figure 4.11: The transformation of a flat MLL into a stress-wedged MLL is done in the following steps: in a first step a regular flat lens is made usually by FIB milling; in a second step a stress layer is deposited onto a sidewall; this will cause the lens to bend and transform into a wedged MLL. This structure has to be tilted accordingly to obtain the best possible diffraction efficiencies.

The approach used by Conley et al. and Prasciolu et al. is using a mask during the deposition process. This mask blocks parts of the material beam from the magnetron towards the substrate [CLQ+08, PLK+15]. The mask has to be designed to lead to a steep gradient in the thickness of the deposited multilayer system. In order to achieve the necessary relative gradual angle as discussed in section 2.4. Due to the shadow of the mask the effective deposition rate can be reduced significantly and the time needed to deposit the corresponding lens prolonged as compared to a flat geometry. Furthermore the deposited wedge has to be known precisely; the actual lens element has to be cut at the right position with the correct dimensions. This type will be called *gradient-wedged* hereafter.
Another approach is to use a stress layer. In this case regular flat geometry MLL is manufactured. Subsequently an additional stress layer is deposited on one side of the MLL. Depending on the stress layer material either the side facing the beam or the opposite one. This leads to a bending of the lens structure and leads to nonparallel interfaces; instead the interfaces are gradually *tilted* as a function of the position of the radius. This method has been proposed by Sven Niese [NKK+14b]. This type will be called *stress-wedged* hereafter, if a distinction to gradient-wedged MLL is necessary.
A scheme of the transition from a flat to a stress-wedged geometry is is shown in Figure 4.11. The stress-wedged approach has been used for the fabrication of wedged MLL during the work on this thesis. For MLLs with a section thickness of $\approx 10\,\mu m$ a stress layer thickness of in the order of 200 nm SiO_2 has to be deposited using ion beam sputter deposition (IBSD) in order to achieve the desired bending of the structure [GBLL06]. The additional layer has compressive stress of $\approx$ 900 MPa. With different thicknesses of the stress layer the lamella will inherit a different bending; therefore a flat MLL can be used to manufacture lenses optimized for different photon energies. Mechanically this currently requires an MLL attached to a substrate; otherwise the bending would occur along the width of the lens. Therefore, this type of geometry cannot be achieved with the coating detached from the substrate. The precise thickness of the stress layer has to be determined numerically in advance of a deposition; these calculations are not part of this thesis.

Radial thickness gradient

Due to the type of substrate movement, which is dominated by the constant spin frequency and results in a rotationally symmetrical distribution of layer thicknesses on the substrate. For a constant angular motion different radii on the substrate spend different times above the magnetron in the particle stream and therefore the resulting layer thickness differs. The result is a radial decrease of the deposition thickness.
As compared to gradient-wedged MLL this gradient has no significant impact on the diffraction properties of the lens. For a given design the focal length f of a lens is approximately a quadratic function of the thicknesses [Mas94]:

$$f = 2dr_n r_n/\lambda \tag{4.5}$$

dr_n is the zone width of nth zone and r_n the respective radius according to the zone plate law.

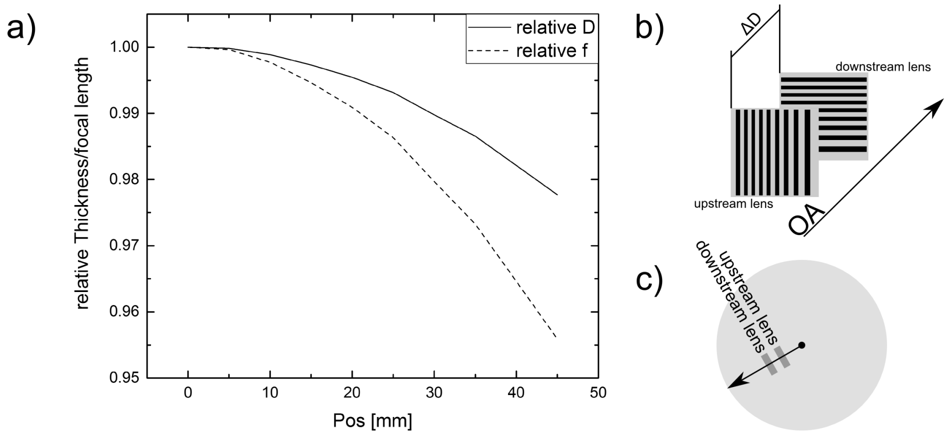

Figure 4.12: a) Measured relative periodic thickness and corresponding relative focal length as a function of the radius of a deposition.
b) Scheme of crossed lenses.
c) Extraction positions of upstream and downstream lens.

An example of a measured radial dependency of the thickness is shown in Figure 4.12 a). This has to be considered for the assembly of crossed lenses for point focusing. Crossed lenses have to be paired together to feature a common focal plane. Assuming a fixed MLL design with a fixed focal length at a specific photon energy a scaling of all period thicknesses results in a change of the focal length: the focal length is a quadratic function of the thickness [Mas94]. Figure 4.12 a) also shows the corresponding calculation.
For the mounting of two perpendicular lenses as shown in Figure 4.12 b) it has to be defined, which relative distance of the two lenses d_r can be achieved practically. The relative distance of the lenses can be offset by the differing focal lengths arising from the different thickness. The upstream lens has to feature a somewhat longer focal length, than the downstream lens. An upstream lens is therefore extracted from a position on the substrate with a smaller radius and an downstream lens from a position with a larger radius as shown in Figure 4.12 c).
The optimum section thickness of an Mo/Si MLL is $t_{opt} \approx 7\,\mu\text{m}$ for best performance at a

photon energy of 12 keV. A relative distance of 30 µm between the entry planes of the MLLs has shown to be a reasonable choice to prevent crashing the structures during assembly and manipulation. This would leave $\Delta D \approx 23\,\mu\mathrm{m}$ of physical space between the MLL lamellae.

5 Experiments with Synchrotron Radiation

Focusing hard X-rays into small dimensions is the ultimate goal of MLL fabrication. In order to achieve the best possible focusing performance the major requirements for the X-ray source are monochromaticity and low emittance [YC13]. Currently this is only given at a few third generation synchrotron radiation facilities worldwide.

In section 4 the manufacturing has been discussed; the used methods give information about the overall quality of the deposited stack and the MLL itself. Currently it is assumed, that most manufacturing errors can be identified using laboratory equipment [Chu15]. However, during the work on this thesis many insights came from synchrotron radiation experiments and some measurements can only be performed there. Results coming from experiments with synchrotron radiation are *the* relevant figure of merit for the quality of an MLL. The main driver for development of MLL in the scientific community and obvious field of application has been the use for focusing hard X-rays from a synchrotron radiation source to small beam sizes [MSV+04, KYW+08, YRS+11]. This is especially evident through the review articles [YCBC14, CBC+16]. Another significant application is full field imaging using MLL as objective lenses, for which the development is masterminded by Sven Niese and Jürgen Gluch at AXO Dresden GmbH and Fraunhofer IKTS [NKK+14a, NBD+16].

Opportunities to measure and conduct experiments at a synchrotron radiation facility are usually limited by a periodical application process for beam time [DES17, ESR17]. This mode results in a limited number of opportunities with usually limited length of the assigned time slots for experiments for external users. The feedback time for improvements based on those experiments is therefore relatively long.

In this section the experiments at synchrotron radiation facilities will be presented and discussed. This includes experiments at beamlines with an undulator as insertion device as well as a bending magnet to probe the focusing properties and the diffraction properties. In Table 2.2 the synchrotron radiation facilities, their location, the beamline used and the respective bending magnet or insertion device have been listed. A setup for the measurements of diffraction patterns of a single MLL is shown in Figure 5.1 a). Focusing is made by a setup as shown in Figure 5.1 b). In order to obtain information about the sample and the wavefield at the position of the sample the method of ptychography is used. In ptychography a reconstruction is calculated based on far field diffraction patterns collected from a raster scan of a sample with overlapping illuminations. It allows to obtain high resolution data of the sample as well as the illumination, which is very valuable in order to understand the focusing properties of optics. The reconstructed wave field can be propagated in order to obtain a caustic of the beam. Ptychography has been in used for optics characterization and is also widespread for sample measurements [TDB+09, KGSL+10, HHP+11, DVC+17].

Parts of the results and discussions in this section have been published in several journals and reports [KBN+14b, KMN+14, KKC+15, MKC+15, KMG+17, KMF+17].
Parts of the experiments at the ESRF have been pursued in the scope of an LTP (Long Term Project) together with the group of Jozef Kečkeš of the Erich Schmid Institute of Materials Science at the Montanuniversität Leoben, Austria. In this LTP the development of MLLs is aimed directly at the application as focusing optics for the analysis of residual stress in hard coatings using nanodiffraction experiments in particular in in-situ environments with unprecedented resolutions.

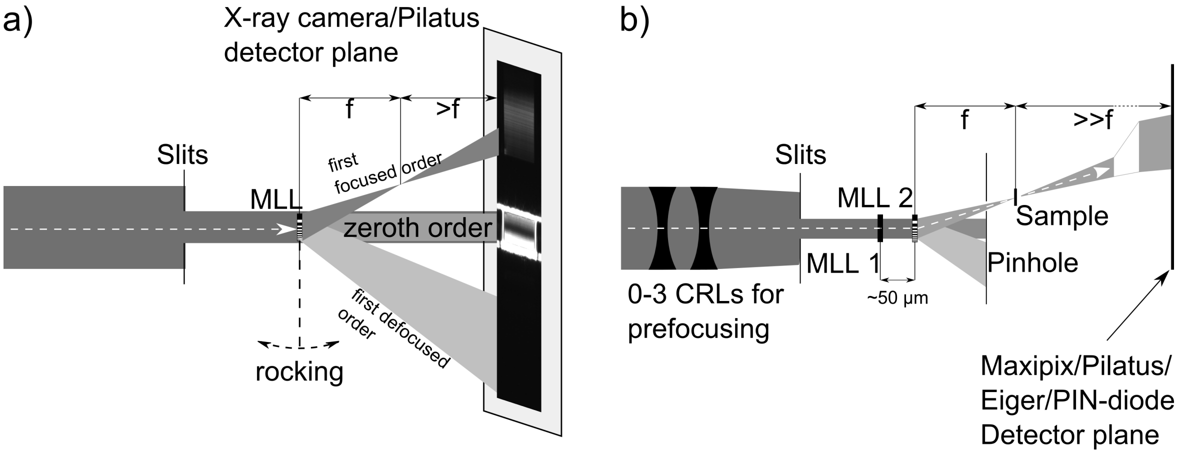

Figure 5.1: a) Scheme of the setup to measure diffraction patterns and of a single MLL. No sample is present in the beam.
b) Crossed MLLs in a point focusing arrangement. This setup is used to perform efficiency measurements, diffraction experiments and STXM including Ptychography.
Based on Figure 4 in [KMG+17].

5.1 Comparing flat and wedged Multilayer Laue Lenses

With the method described in section 4.2 the making of tilted and wedged lenses made from the same deposition is possible. A direct comparison of the properties of such lenses is of particular interest to find general limitations and challenges as well as to verify properties of this geometry and the manufacturing approach.
The lenses for this experiment were made according to the design DDD9@15_50 (see Table 2.1). The goal of this experiment was to find the differences in diffraction properties between otherwise identical flat and wedged lenses. Experiments were conducted at the ESRF beamline ID13 and the general setup is shown in Figure 5.1 a). Slits have been positioned in such a way that they block most of the flat field outside the aperture of the lens for rocking measurements.
Figure 5.2 shows the detector signals for a) a flat and b) a wedged lens for a series of angles as appearing on the PCO-4000; OptiquePeter (PCO) high resolution camera. The images acquired by the camera are dominated by the absorption and diffraction of the incoming beam in the structures. Differences between these images are defined by different diffraction

taking place in the lens. The zero angle is defined arbitrarily at an angle being approximately between the diffraction of first focused and first defocused orders. For clarity only the first focusing order is shown in the upper part of the images.

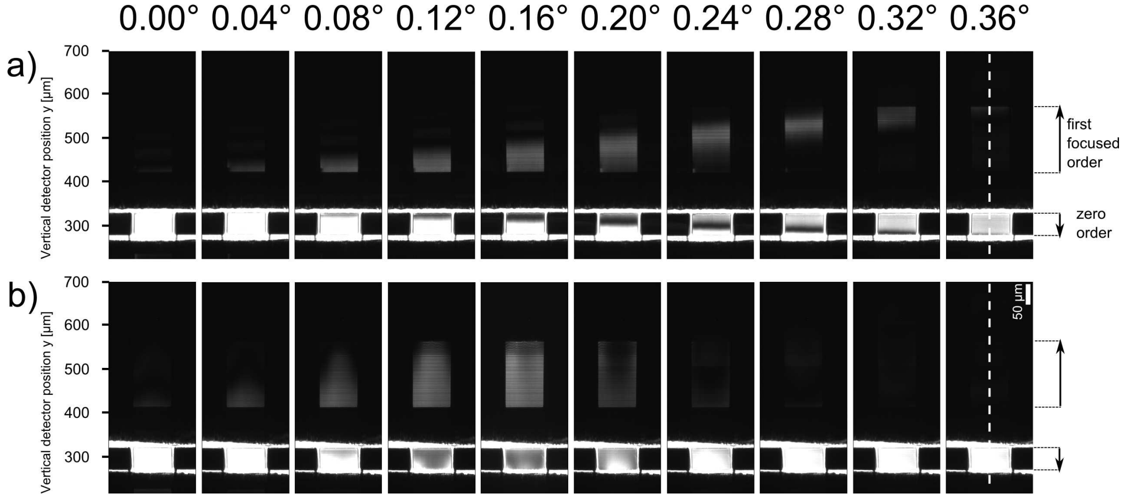

Figure 5.2: Detector signal of the absorption and diffraction of a) a flat and b) a wedged MLL for tilting angles 0° to 0.36°. The stress-wedged lens has an almost uniformly illuminated first diffraction order for an angle of 0.16 °; for the flat lens only one part of the lens is diffracting significantly at one angle. The arrows indicate the direction of the radius according to the zone plate law.
Figure 5 from [KMG+17].

For the flat lens a band of lower intensity is noticed in the zeroth order region (i.e. transmission image of the lens). This dark band is a result of the Bragg diffraction and it moves along the lens aperture, if the rocking angle is changed. Correspondingly, a bright band depicting the diffracted intensity can be seen in the region of first order diffraction.

For the tilting series of a wedged lens from the same deposition a different behavior is observed. Here one distinct angle shows a significantly reduced transmission through the lens aperture, while the area of the diffracted beams becomes uniformly illuminated. The only exception is the part of the aperture with the thin layers, which suffers from a significant layer placement error as discussed in Figure 4.4.

Figures 5.3 a) and b) show the image of the PCO for both, flat and wedged MLL in Bragg condition. In order to identify the difference in diffraction properties between the lenses more quantitatively, the original diffraction images having the same acquisition time are evaluated. The dark current is estimated by taking an image without any X-ray beam on the scintillator. Assuming that this image should correspond to a zero signal, this signal is subtracted from the acquired original diffraction images.

The measured intensity as a function of the position on the detector is shown in in Figure 5.3 c). The graph shows the diffracted intensity being more evenly distributed and having the larger values in case of the wedged lens. It still seems to show an area roughly in the middle of the lens, where the intensity in the diffracted area is the highest and thus the diffraction efficiency of the represented lens area is the largest. A fully uniform distribution would be expected for a perfectly made MLL [KIT+08]. The wedged MLL shows

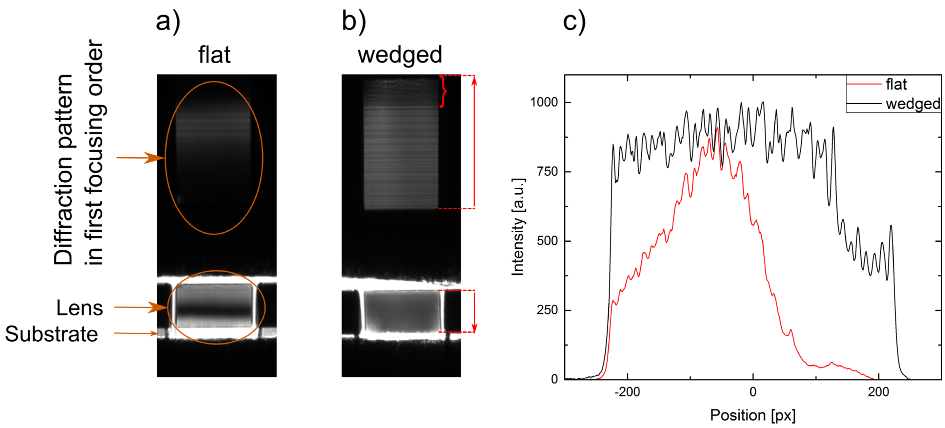

Figure 5.3: a) and b) show the comparison between the flat and the wedged MLL tilted. The arrows indicate the direction of the radius acording to the zone plate law. Figure 1 from [KMN+14].
c) Normalized intensity of the first focused order for the highest intensities in the diffraction pattern, respectively.

similar characteristics as the flat lens in particular in terms of local drops in the diffracted intensity. This is caused by the diffraction properties which are specific for this particular deposition [AKB15]. This confirms, that the overall diffraction properties defined by the deposition are not changed, if a lens is wedged using a stress layer.

For further analysis an additional representation has been chosen to discuss the properties of the lenses. Figure 5.4 shows the intensity on the PCO as a function of the rocking angle. This kind of representation has been used for MLLs first in [KIT+08]. It is shown for one flat and both wedged lenses, which have been used for focusing later on. This representation is suited to show, which part of the lens contributes at a particular rocking angle to the each diffraction order. This simplifies the analysis, how well the lens has been wedged or if there are kinks present in the lens [KKC+15]. This representation is used for several discussions in the experimental section of this thesis.

In this graph the maximum of the fulfilled Bragg condition changes nearly linearly as a function of the angle but with a different apparent slope, which is consistent with other measurements [MKC+15]. The detector is placed in a close adjacency to the lenses with a distance of 25 mm. Therefore, due to the small magnification it is significantly different for the first focused and defocused orders in case of the flat MLL. This is consistent with the intersect theorem. This difference is reduced with an increase of the detector distance as the magnifications of both orders converge.

The slope for the wedged lens is much steeper and almost vertical for the first focused order as compared to the flat lens i.e. almost all of the lens diffracts at once. Ideally a perfectly vertical stripe could be measured [MPA+15]. These properties of a wedged MLL result in a more evenly distributed efficiency as compared to the tilted lens. This increases the effective aperture of the lens and thus potentially allows achieving smaller focal spot sizes [KMS+06]. The slope is not perfectly vertical; however, the difference as compared to the flat lens is

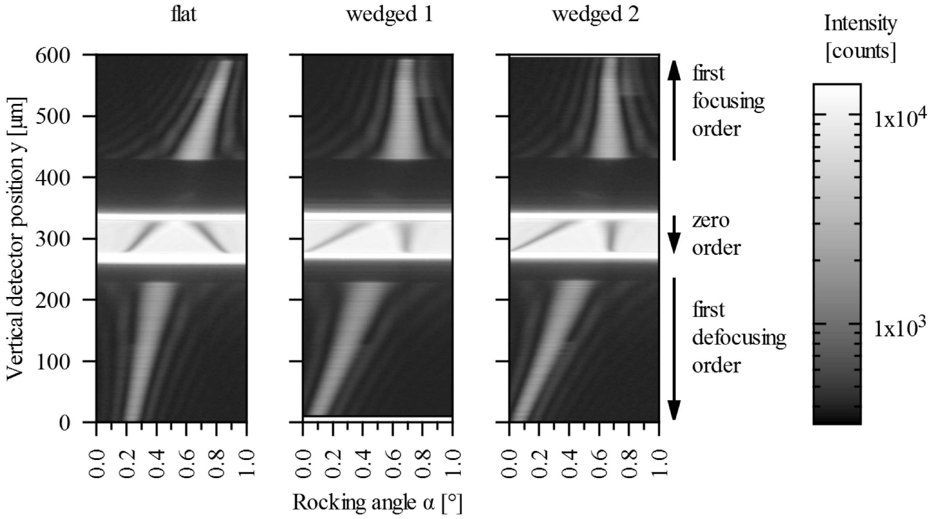

Figure 5.4: Comparison between one flat the two wedged MLLs, which have been used for the focusing experiments. Figure 6 from [KMG+17].

significant. This corresponds to the expected behavior for wedged lenses at their optimum energy [YMM+07, KMS+06]. These measurements show that the process of adding a stress layer to a flat MLL can be used to successfully manufacture a wedged lens in terms of diffraction properties.

The kink is due to the significant layer placement error. Corresponding to this the diffraction pattern for this particular d-spacing will appear at a different position relative to the rest of the lens. This is also the reason, why a wedged MLL can be used for one energy only achieving its optimal performance (see Figure 3.12 and [CLQ+08, MPA+15, KMG+17]).

The flawed part of the aperture will be blanked by the slits in most of the subsequent experiments.

5.2 Crossed flat and wedged multilayer Laue lenses

The additional SiO_2 stress-layer has been deposited onto several lenses and the bending effect has been measured using the Xradia NanoXCT-100 at Fraunhofer IKTS [NKK+14b]. The measured bending of the lenses has been larger than expected and the optimal energy according to the wedging would be 10.5 keV instead of the previously designated 15 keV. The synchrotron radiation experiments have therefore been performed at 10.5 keV. At this energy the focal lengths as well as the working distance for focusing experiments – compared to the design energy – is shortened by about 30 % to 6.65 mm and 2.2 mm, respectively.

Five individual lenses have been prepared for these synchrotron radiation experiments; two pairs for the assembly of two point focusing MLLs and one as a reference.

In this section the focusing measurements of the two pairs of MLLs, one flat and one wedged, are discussed. These are the lenses, which have been characterized individually in the previous section. This section shows the challenges of crossed lenses as well as the impact of a

significant layer placement error on the diffraction properties and focusing capabilities. The pair of flat lenses has been used to test the deposition on aberrations originating from the deposition. It has been bonded onto a single sample holder [KBN+14a, NKK+14a].
Due to the layer placement error identified and discussed earlier, it was expected to be necessary to use a smaller part of the aperture of the lens, where the layer placement error would not reduce the focal quality significantly. As all lenses were made from the same deposition they would show the same or at least similar beam degrading effects. Therefore, it was meaningful to use and test areas representing the same radii on both of the crossed lenses. Due to this reduced effective aperture of the lens the diffraction limit of the focal spot size would increase and the total flux would decrease.
In order to study the aberrations of the MLLs, the illuminated area of the aperture of the lens was varied in position and size using the beam defining slits. By comparing the reconstructed foci and the propagated focal series obtained at different positions using a small size, local defects within the multilayer can be identified and localized. The comparison of the reconstructed foci obtained at different sizes at the same central position indicates, how global aberrations affect the shape of the focus.
The best reconstructed focal spot in terms of spot size and intensity of the side lobes is shown in Figure 5.5. The FWHM of the central peaks is 33 nm and 28 nm in the horizontal and vertical plane, respectively.

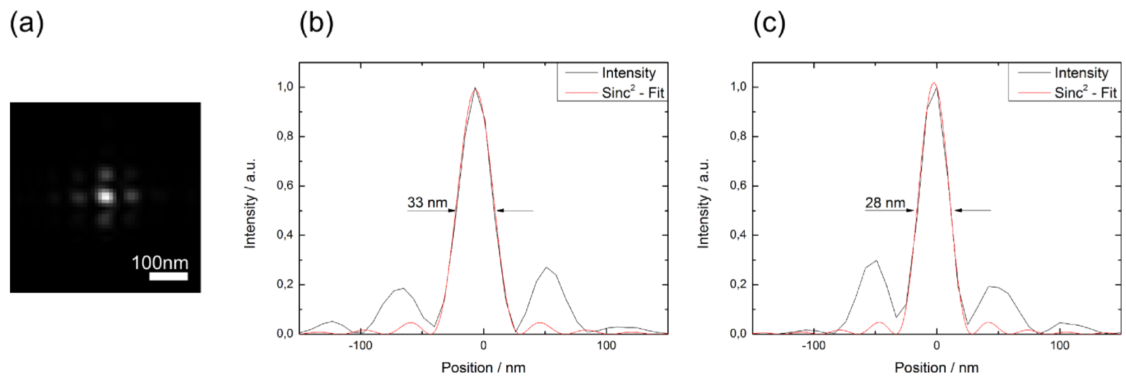

Figure 5.5: a) Best quality reconstructed focal spot for the pair of flat MLLs.
b) Vertical line profile through focus.
c) Horizontal line profile through focus.
Figure 7 from [KMG+17].

According to the measurements from the crossed flat lenses the areas of the aperture without significant aberrations were known and the crossed wedged lenses were studied with these preknowledge. For a central position on the aperture the slit edge length has been varied from 35 µm down to 15 µm. The reconstructed focal intensities and the estimated focal spot sizes are shown in Figure 5.6.
It is evident, that the size of the central peak decreases for larger apertures up to an aperture side length of 25 µm. Simultaneously the increased intensity in the side lobes especially in the upper right quadrant can be noticed. For aperture edge lengths above 25 µm the size of the central peak starts to increase additionally. This is as the additionally illuminated

parts of the aperture do not contribute to the central beam feature anymore due to the layer placement error.
Wrong layer thicknesses will wrong diffraction angles; therefore the respective parts “focus” to a different focal plane. Depending on the type of layer placement error the focal spot can be smeared, the intensity of the side lobes can increase or multiple focal spots can emerge. Some beam features may be found in a significant distance to the main peak and is thus will not contribute to the reduction of the focal spot size but to increasing aberrations. Based on this, an alignment, i.e. the selection of the illuminated area of the lens, with a good balance between focal spot size, aberrations and decrease of flux has to be done.

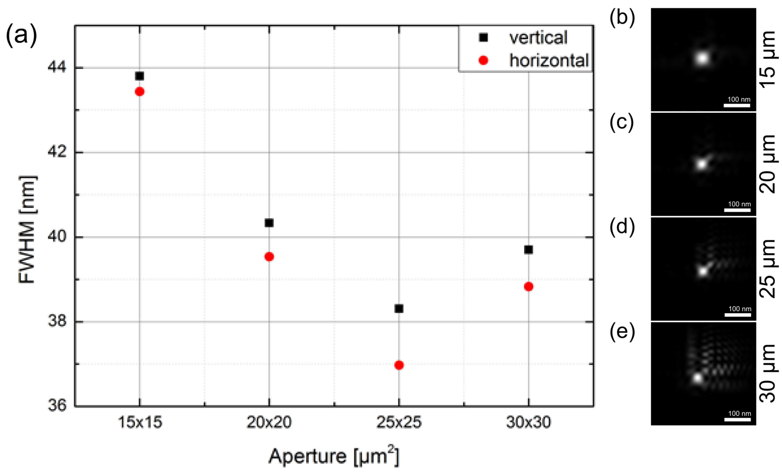

Figure 5.6: a) FWHM of reconstructions for different illuminated lens apertures of wedged MLLs.
b)-e) Intensities of the reconstructed focal spots for the different illuminated of wedged MLLs.
Based on Figure 10 from [KMG+17].

The focal spot with the least aberrations has been obtained for an edge length of 15 µm (values according to the motor encoders of the slits) in both, vertical and horizontal, directions. The reconstructed intensity distribution and the profiles are shown in Figure 5.7.

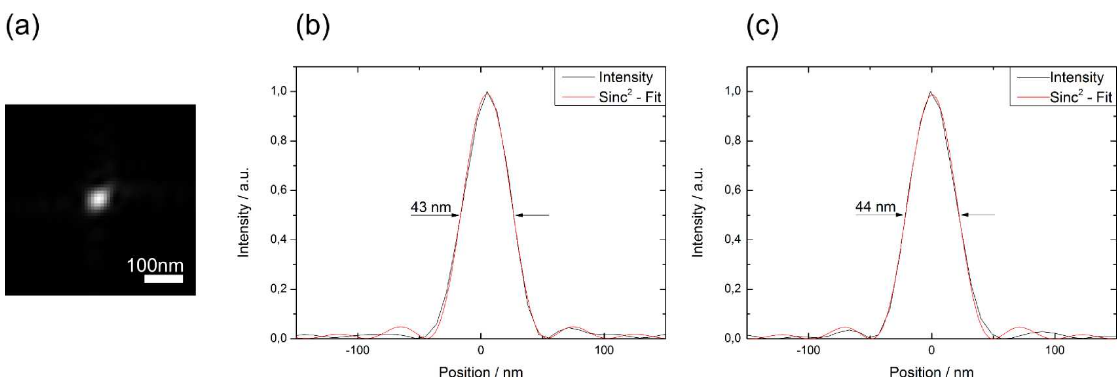

Figure 5.7: a) Best quality reconstructed focal spot for the pair of wedged MLLs.
b) Vertical line profile through focus.
c) Horizontal line profile through focus.
Figure 8 from [KMG+17].

Following the previous experiments the aperture size of 15 µm and position with the least intense side lobes were used in order to obtain measurements as aberration free as possible. Figure 5.8 shows the STXM and ptychography measurements made with the focus with the slit size of 15 µm. The sample is a Siemens star (NTT-AT ATN/XRESO-50HC) and made out of 500 nm thick tantalum. The measurements in Figure 5.8 a) and b) have been made with switched fast and slow axes to examine the stability of the setup for both cases. The smallest features with 50 nm lines and spaces are resolved. Furthermore, the contrast of the material is fully represented by the drop in intensity and almost no smearing is noticed. The measured reduction in intensity is very similar to the expected loss in intensity of 15.8 % [HGD93].

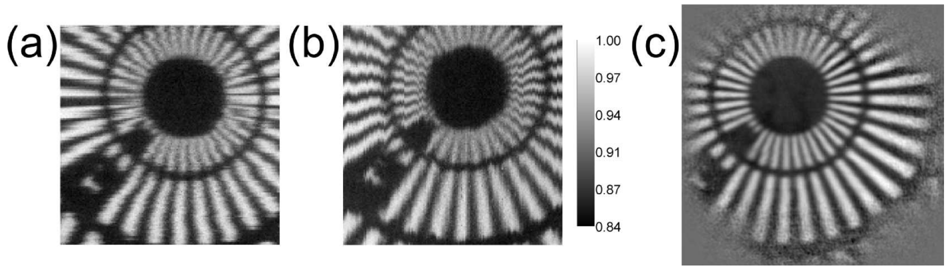

Figure 5.8: a) and b) show the STXM measurements with a PIN diode as a detector.
c) Reconstructed phase image of the Siemens star test pattern.
Figure 11 from [KKC+15].

Efficiencies of both crossed flat and wedged MLLs have been measured. Therefore the flux of the focused beam coming through the slits, the MLLs and the pinhole is measured. The reference flux is measured with only the slits in place while MLLs and OSA have been moved out of the beam. Results are shown in Table 5.1. The individual efficiency is calculated by the geometrical mean of the combined efficiency under the assumption, that both MLL in the pair have identical efficiencies. Individual efficiencies cannot be measured with this method. The measured efficiencies are very close to the calculated ones by the two beam approximation of 49 % (see [YCBC14] and section 3). It can therefore be assumed, that the MLL are near their possible optimum and do not suffer any significant loss of efficiency due to absorption of the stress layer or sectioning or deposition effects such as roughness.

Table 5.1: Efficiencies of the crossed η^2 and individual η flat and wedged MLLs.

MLL Type	Section Thickness [µm]	η^2 [%]	η [%]
Flat	4.5/ 4.7	7.9	28.2
Wedged	7.0/ 8.0	19.8	44.5

5.3 Far Field Diffraction Experiments: Layer Tilt/Bending Analysis for the BNL MLL

This section describes experiments at the optics testing beamline 1-BM of the Advanced Photon Source (APS) with a lens made at BNL. It is mainly evolving around the analysis of far field diffraction patterns acquired from rocking series. The diffraction limit of the lens as well as some characteristics of the physical shape have been analyzed in particular.

Multilayer deposition corresponds to the N100 design in Table 2.1. The multilayer stack has a total thickness of more than 100 μm, which was of particular interest, as the multilayer thickness was approximately twice compared to previously reported MLL coatings [YRS+11, KBN+14a]. This was partly achieved through the use of the material combination WSi_2/Al. The spacer consists of a material combination of approximately 95 % aluminum and approximately 5 % of silicon by weight and the deposition was made in a sputter gas atmosphere with 10 % N_2/90 % Ar. While the material properties of aluminum allow for low stress multilayers [MKC+15] its X-ray optical properties are very similar to silicon (see section 4.5).

The deposition including the substrate was cut, sandwiched, polished and attached onto a diamond plate. Subsequently, it was physically polished from the opposite side to obtain the desired section thickness of approximately 10 μm. The result of this procedure is a lens element, which has a length of approximately 2.7 mm. A more detailed description of the process is given in [YCBC14] and an earlier stage development of the sectioning method is discussed in [KMS+06]. Parts of this section have been published in [MKC+15] and [KKC+15].

Quality control after the sectioning process was done with SEM measurements. However, SEM is well suited to detect a layer placement error and large defects but comes to its limits to detect some types of manufacturing errors, such as specific types of deformations of the multilayer stack, small kinks, twisting and warping. In order to allow for an analysis of these challenges a method has been developed, which uses the far field diffraction effects of the lens.

In a first step the transmission through the lens was measured with the AndorNeo high resolution CMOS camera. This camera is similar to the one discussed in Figure 5.1 a). A radiograph image for a fixed rocking angle is shown in Figure 5.9 as seen with the Andor Neo high resolution X-ray camera. Similar to previous measurements dark areas in the transmission image represent parts of the lens with Bragg diffraction. For a perfect lens it is expected, that this area is a dark band parallel to the layer interfaces. If this is not the case the lens can be expected to be deformed. For a situation where two period thicknesses along the radius direction fulfill the Bragg condition at once, it can be assumed, that this is due to a kink in the lens.

Both phenomena are visible in the radiography shown in Figure 5.9 and give information about the overall structure of the lens: On the left side two distinct parts of the lens are in Bragg condition and from the left to the right it is evident, that the Bragg condition is not consistently at one radius. It has to be kept in mind, that the area needed for focusing is only slightly wider than the stack height. Therefore, it would be sufficient to have one single part of the lens being without a counterproductive physical deformation.

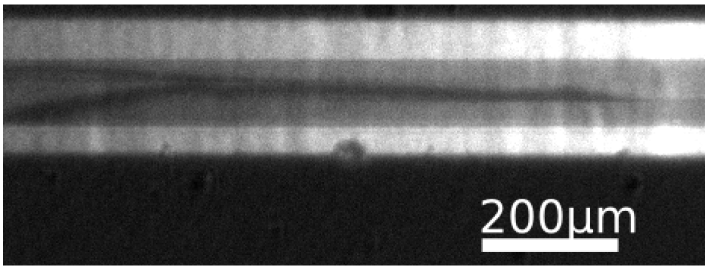

Figure 5.9: Radiograph of the lens. The apparent lower transmission area in the lens represents missing intensity diverted by the Bragg diffraction. Part of Figure 1 in [KKC+15].

Further measurements were done using a Pilatus 100 k pixel detector in a distance of 90 cm from the lens. This detector allows acquiring far field diffraction images with virtually no noise.
Again the resulting stack of images is shown in the representation of intensity as a function of the rocking angle. An equivalent representation of the local diffraction efficiency can be calculated by CWT and is shown in Figure 5.10 a). This representation allows interpreting part of the physical character of the lens. Figures 5.10 b) and c) show the diffraction intensity distribution based on measured data and physical shape of the lens for two positions on the lens with distinct features.

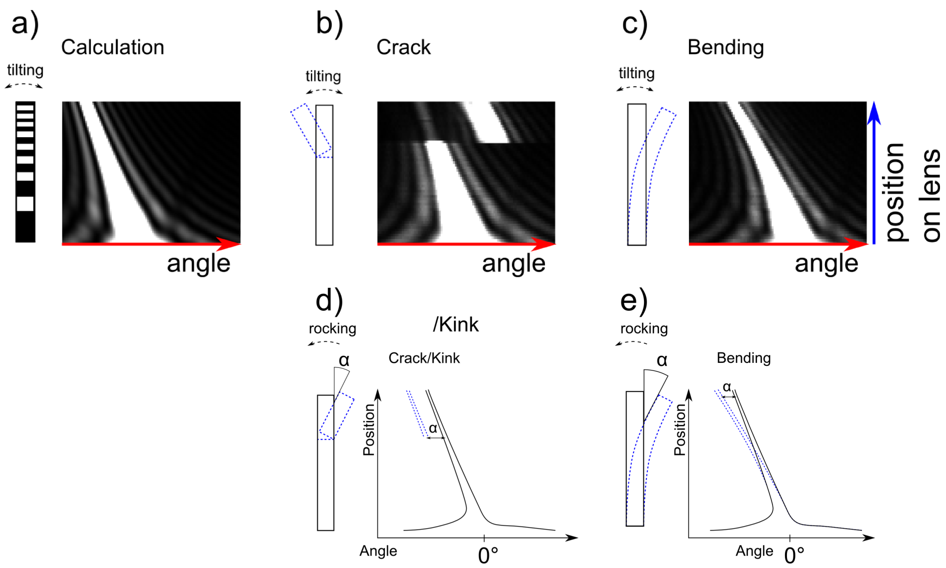

Figure 5.10: Intensity as function of the tilting angle compared for different types of problems in the lens. a) Calculated diffraction efficiency as a function of the tilting angle.
b) Measured bent MLL.
c) Measured MLL with kink.
d) Calculation of angular displacement for a crack.
e) Calculation of angular displacement for a bend lens.
a) - c) Based on data from Figure 3 in [KKC+15].

Based on these images several physical properties of the lens can be determined; the diffraction patterns are compared with calculations of the diffraction properties of the lens. Each part of the lens is defined by its position along the deposition, its radius and the section thickness. Therefore, the designated rocking curve can be matched to a certain radius and position on the lens in accordance with the limitations stated above. The assumption is, that the center of this rocking peak is determined by the local orientation of this particular part of the lens. It will change according to the relative tilting angle. Based on this assumption and the calculated diffraction pattern for the lens the relative angular shift between the calculations and the measurements can be determined. This is shown in Figure 5.10 d) and e). The solid contourplot represents calculated data, while the dashed contourplot represents a part of a contourplot deviating from the calculated properties. The angular difference is calculated from this distance of the calculated and measured data which is then assumed to be the angular displacement. One part of the lens is used as a reference, where the angle difference between measurements and calculation is defined as zero. For all other parts the relative angular shift between the measured and calculated rocking curves is calculated as a difference to the reference. The results of this method are qualitatively similar to the method discussed in [NKK+14b]; however, the approach discussed here uses calculations in order to determine the angular displacement and does not need any reference sample.
The result of this angular displacement calculation is shown in Figure 5.11. Similar to other methods it can only detect specific types of manufacturing errors, which have an impact on the diffraction properties of the lens and change the angle of the diffracted beam; in particular this is true for *bending* and *kinks*.

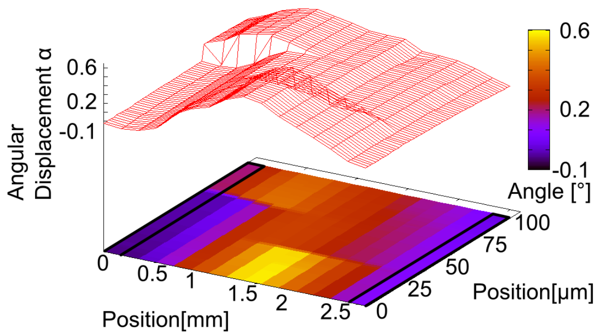

Figure 5.11: 3D representation of the angular displacement α. The boxed parts in the heatmap were used to produce the diffraction patterns shown in Figure 5.10 b) and c).
Part of Figure 5 in [KKC+15].

After these measurements and the respective analysis, the diffraction efficiency of the lens was of particular interest. For a measurement the part of the lens, where no kink was visible, has been chosen. In the representation in Figure 5.11 this is the far right part of the lens. The illumination of other parts of the lens structure was therefore blocked by slits.
It is necessary to identify the area on the detector occupied by the first diffraction orders. This can be done by the maximum intensity projection of the stack of images acquired from the rocking experiment, i.e. every pixel of an image with the same size as the detector output

represents the maximum value of that particular pixel within the image stack as shown in Figure 5.12 a) measured with the Pilatus pixel detector. A disadvantage here is, that a possible overlap of the diffraction orders cannot be identified or considered easily for the analysis. Therefore, higher orders have been ignored for the diffraction efficiency analysis due to the expected small intensity in the relevant area of the first diffraction order. Figure 5.12 b) shows the diffracted intensity as a function of the rocking angle.

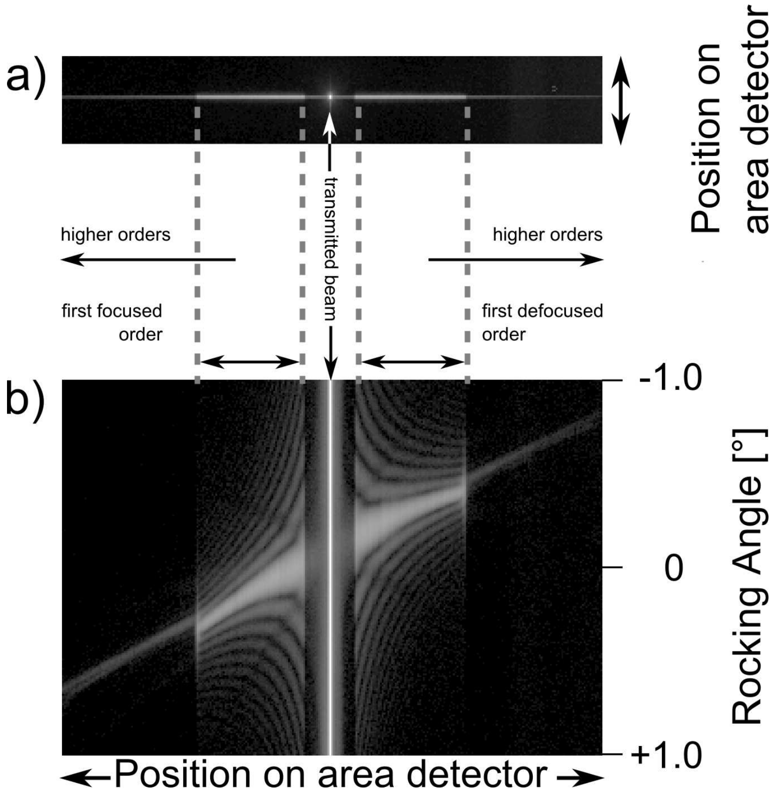

Figure 5.12: a) Maximum intensity projection of the diffraction efficiency measurement in Logarithmic scale.
b) Intensity as function of the rocking angle in Logarithmic scale.
Data has been used for Figure 2 in [MKC+15].

In a first step the projection enables to distinguish between the different diffraction orders by their area and intensity. The total diffraction efficiency of the lens is the integrated signal of the respective areas for every image in the stack divided by the direct signal on the detector without the lens, which has to be measured separately. The resulting total diffraction efficiency of the lens and the calculated diffraction efficiency is plotted in Figure 5.13. Shapes of the patterns are quite similar but not identical. The plots of the measured efficiency are not symmetrical for focused and defocused orders as it would be expected for a perfect lens. This is a result of the bending of the lens.
There might be several possible reasons for the lower total diffraction efficiency as compared to the calculated values. The calculations have been made assuming a section thickness of 9.6 µm. This value was estimated by a fringe analysis of the diffraction but only for one part of the lens [MKC+15].

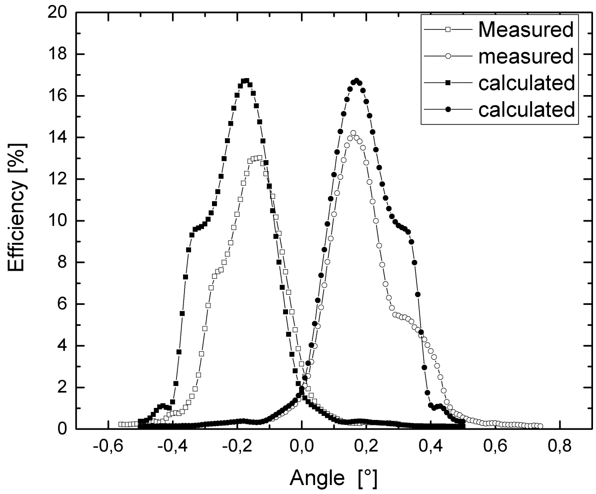

Figure 5.13: Diffraction efficiency as a function of the rocking angle. Measured efficiency and calculated efficiency are somewhat similar in terms of the shape; the expected diffractione efficiency is however somewhat larger than the calculated one. Data from Figure 3 in [MKC$^+$15].

As a complementary method a direct comparison between the measured diffraction patterns and the calculations has been used. The calculations have been made for various thicknesses up to 30 µm. The Darwin widths for each d-spacing and section thickness have been determined and were compared with the actual diffraction patterns for the whole lens. This approach resulted in approximated section thicknesses between 4 µm and 15 µm due to discontinuities and possible errors in the structure. This range of possible section thicknesses allows for a large deviation of the expected diffraction efficiency. An uncertainty in the section thickness will likely lead to a false estimation of the diffraction efficiency as the calculated diffraction efficiency can change quite significantly for small difference of the section thickness. The lens is mounted on a diamond membrane, which only absorbs $\approx 2\,\%$ of the beam, what is unlikely to represent the large deviation. A further possible reason is the difference between bulk density and the density of the deposited material [Con14, Bra17]. However, calculations have shown a rather small impact of the small changes in the density on the diffraction efficiency. Only small changes in reflectivity have also been observed for extreme UV optics by the change in density [Bra17].

In the data a “shoulder” of the efficiency is prominent for higher values of the rocking angle. The central position of the rocking curve moves along the radius different d-spacings result in different Bragg angles. In addition, the Darwin width increases for larger d-spacings, which represent the transition from kinematic to dynamical diffraction. Therefore, the “shoulder” is the result of the integration of the intensity for every angle of the rocking curve. Due to the asymmetry the integration of the local efficiencies will result in a different value as compared to a perfect lens.

5.4 Mo/C/Si/C-lens diffraction measurement

The three-material system is based on the materials molybdenum, carbon and silicon as described in section 4.1. The calculations showed efficiencies significantly exceeding the ones of material combinations using either tungsten or tungsten disilicide as the absorber for photon energies between the absorption edges of tungsten and molybdenum at approximately 10 keV and 20 keV.

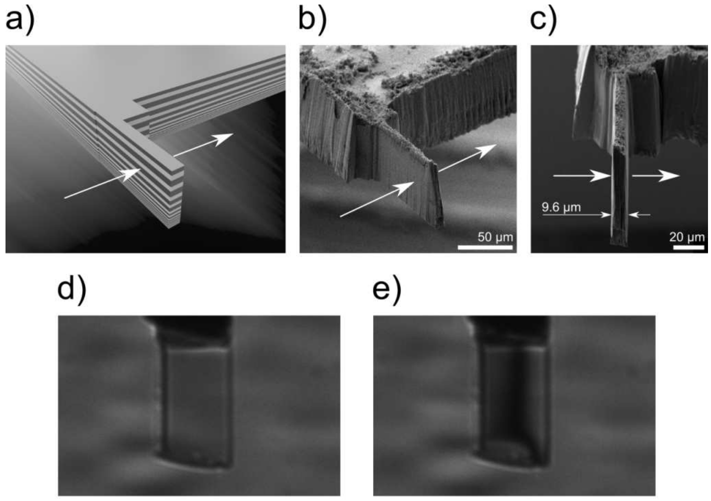

Figure 5.14: a) Scheme and b) SEM images of the lens measured at 1-BM.
c) SEM image of the lens in a side view.
d) and e) show radiographs as seen by the Andor Neo of the lens in off Bragg and Bragg condition.
Figures 2 and 4 from [KMF$^+$17].

An MLL was manufactured from a deposition according to the design DDD9@12_50 in Table 2.1. The general shape of the lens is shown in Figures 5.14 a), b) and c) with a scheme and SEM images. Due to the tip geometry is was possible to measure the section thickness of 9.6 µm directly in the SEM image. The sectioning process of this particular lens was done at the Fraunhofer IWS and the Leibniz Institut für Polymerforschung in Dresden for rough and fine sectioning using lasercutting and FIB milling, respectively.
Similar measurements have been shown in the previous section for a different lens in order to detect the structural properties of the lens as well as the diffraction efficiency. Figures 5.14 d) and e) show transmission images acquired with the AndorNeo high resolution X-ray camera for the lens in off Bragg condition and Bragg condition.
The measurement of the diffraction efficiency was made very similar to the measurements in the previous section and also at the 1-BM-B endstation of the APS. CWT calculations have been made for the design of the lens with Mo/Si as material system. The three-material system cannot be implemented straightforward into the existing CWT code, so the transition layer has been droped for the calculations.
The graphs of the diffraction efficiency as a function of the rocking angle – measured and calculated – are shown in Figure 5.15. Measurements and calculations agree well in terms of

absolute diffraction efficiency as well as in the overall shape. A small difference can be noted in the angular distance of the peaks. Overall the difference is significantly smaller, than for the measurements in the previous section.

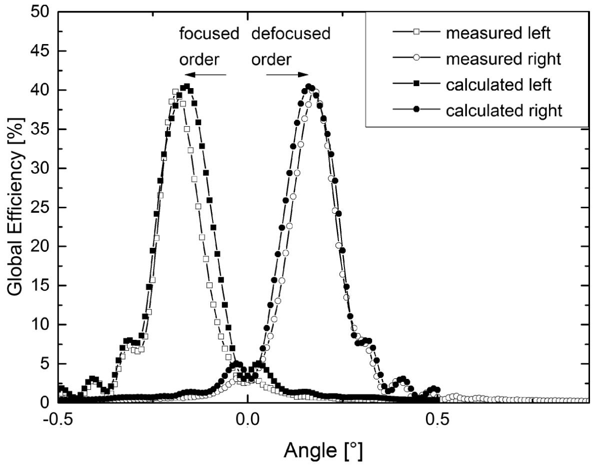

Figure 5.15: Total Diffraction efficiency for the full aperture of the MLL as a function of the rocking angle. Plotted are the efficiencies measured for the lens and efficiencies calculated using CWT. Figure 6 from [KMF+17].

5.5 Mo/C/Si/C-MLL for point focusing

Based on the design discussed in the previous section further deposition iterations have been made in order to reduce the layer placement error. Figure 5.16 shows individual MLLs from which crossed MLLs have been manufactured. They have been used for point focusing in the experiment described hereafter.

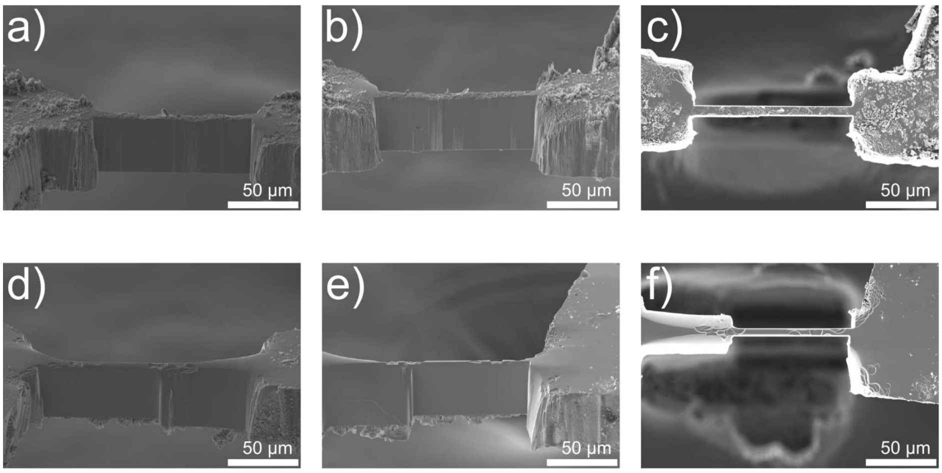

Figure 5.16: a)-c) SEM images of the first and
d)-f) the second lens, respectively, which were combined to the point focusing device.

The lenses still have some imperfections caused by the multilayer deposition or the subsequent sectioning processes, respectively. In one of the lenses a droplet is present. This has already

been identified during the FIB processing and the respective part has not been thinned down any further. The second lens suffers from a crack in about a half of the designated aperture. This part had to be discarded for further processing as well. The width of the originally designated aperture is chosen to allow some imperfections and still being able to use a significant part of the milled structure for focusing. Additionally, on one of the lenses a part of the deposition has chipped due to the large FIB milling current and roughness on the upper surface. The final section thickness of the lenses can be approximated analyzing Figures 5.16 c) and f).
The photon energy for the focusing experiment was chosen to be 12.7 keV, which is somewhat higher than compared to the design energy of the lenses; this was done due to good flux characteristics of the ESRF ID13 beamline at this energy.

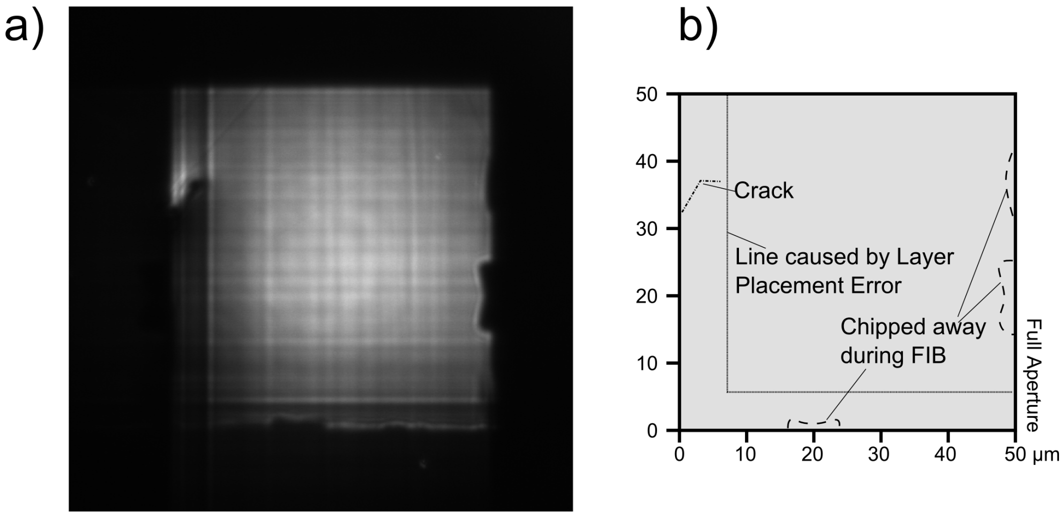

Figure 5.17: a) Diffraction pattern of full physical aperture of the crossed lenses as seen by the PCO.
b) Scheme of the prominent features of the diffraction pattern.

The diffraction images as captured by the PCO are shown in Figure 5.17. Compared to previous measurements the intensity in the far field diffraction pattern is distributed more evenly and with less dark and brighter bands in the center. However, imperfections are still present: On the right and lower side a part of the deposition chipped away during FIB milling. On the lower left side a crack is visible. On the left an lower side a line is visible, which results in a noticable change of the diffraction properties. This corresponds to the significant deviation in zone widths compared to the design in this part of the deposition, which has been measured using SEM. However the reason for this specific large and localized deviations is still under investigation. In general the intensity of the diffraction pattern is more evenly distributed, than for previous measurements (e.g. Figure 5.3) and shows the improvement of the stability of the deposition process.
Several STXM measurements were performed. The acquired far field diffraction patterns of each scan were evaluated using ptychography. As a first step a small aperture of 20 µm × 20 µm defined by the slits has been used to check the quality of the focal spots for smaller and more defined parts of the lens. After each scan, the illuminated area was moved along the diagonal

of the aperture. This approach has proven to be useful for lenses with a layer placement error, even if unidentified beforehand. It showed which part of the lens seemed to have potential for a good focal spot in terms of its shape. In addition, it gives information regarding the relative position of the focal plane in the beam propagation direction (see Figure 5.18).

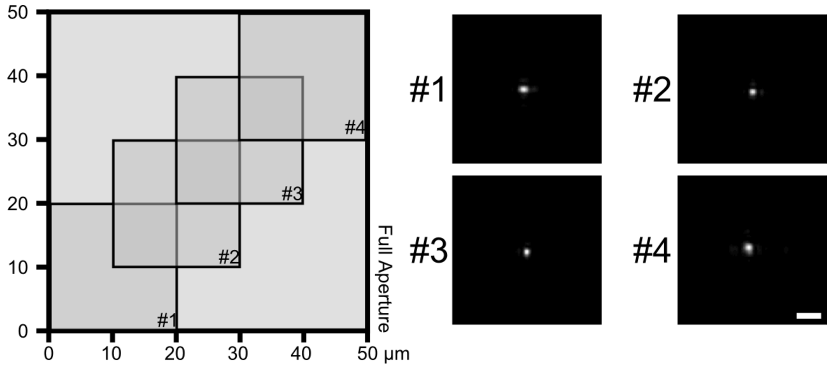

Figure 5.18: Scheme of differently positioned approximately 20 µm × 20 µm sized illuminated areas on the crossed lens aperture and respective reconstructed focal spots. The bar in the lowever right frame corresponds to 200 nm.

The estimated focal planes are all within the depth of focus and show a significant central main feature and little side lobes. This is except for the last measurement, where a part of the crack and the bright band can be found in the illuminated aperture. This part of the lens will be disregarded for the final measurements. As a second step the aperture is increased from the corner with the large zone widths, where no problems have been found. The positions and sizes and the reconstructions are shown in Figure 5.19.

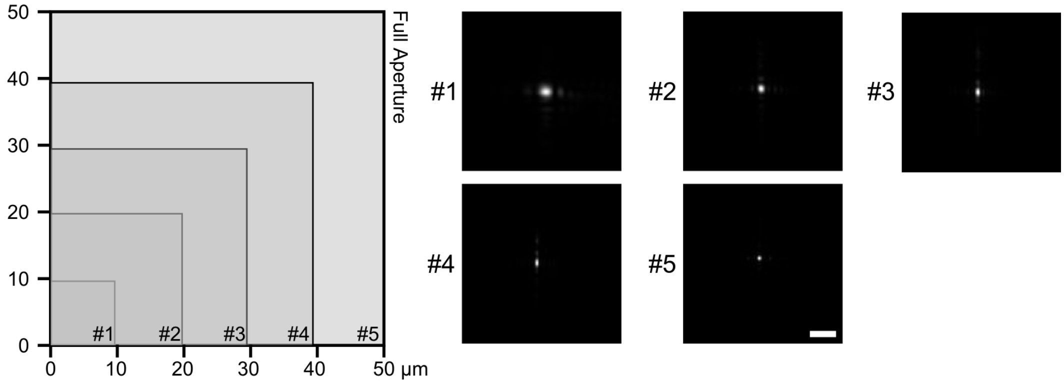

Figure 5.19: Scheme of differently sized illuminated areas on the crossed lens aperture and respective reconstructed focal spots. The bar in frame #5 corresponds to 200 nm.

The reconstructions show an astigmatism of the beam. As expected for a proper lens the focal profile width decreases with an increasing numerical aperture. The astigmatism is significant for the caustic shown in Figure 5.20. From the largest useful aperture the difference in focal planes is estimated to be ≈ 45 µm as shown in Figure 5.20. The profiles of the beams are shown in Figure 5.21. Sizes of the beams in the respective focal planes are approximately 24 nm and 22 nm, respectively. In the intermediate plane the beam has a nearly symmetrical size of approximately 45 nm × 60 nm.

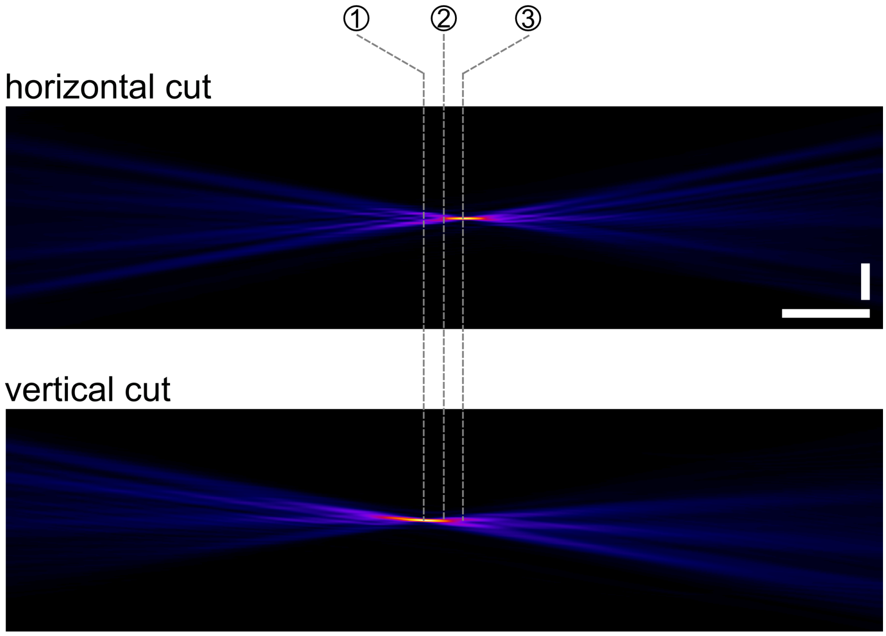

Figure 5.20: Caustics for the horizontal and vertical planes. The beam positions of the smallest profiles in horizontal and vertical directions are marked with 1 and 3, respectively. Position 2 is, where the beam appears most uniformly in both directions. The horizontally oriented bar corresponds to a propagation distance of 100 µm, the vertically oriented bar corresponds to 400 nm.

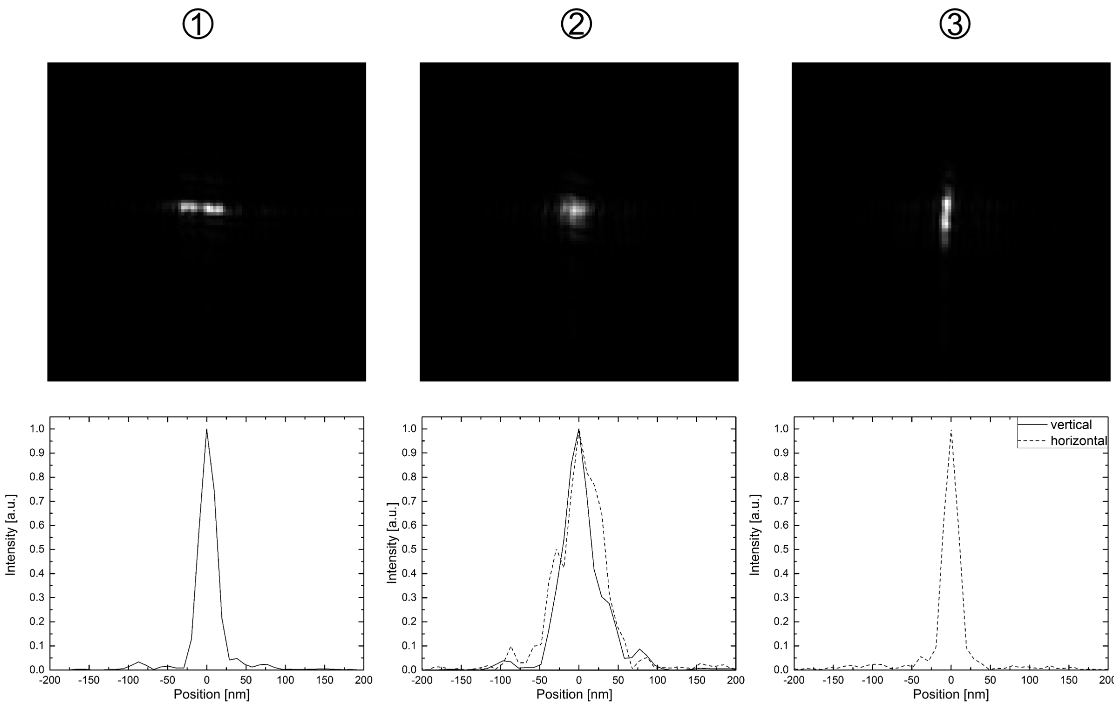

Figure 5.21: Beam intensities and line profiles in the respective focal planes and the intermediate position according to Figure 5.20. The beam widths correspond to the width of the fitted peak function.

STXM measurements have been performed in order to verify the resolution predicted by the ptychographic reconstructions. Figure 5.22 shows the results of STXM the measurements. The 50 nm lines and spaces are clearly resolved with the respective focal “lines” of the lenses. The respective perpendicular directions show a significantly worse resolution, here only 100 nm lines and spaces are resolved. The measurements have been performed with the respective fast axis to ensure the necessary stability in the scanning process. For the intermediate position the focal planes the setup still allows resolving lines and spaces significantly smaller than 100 nm.

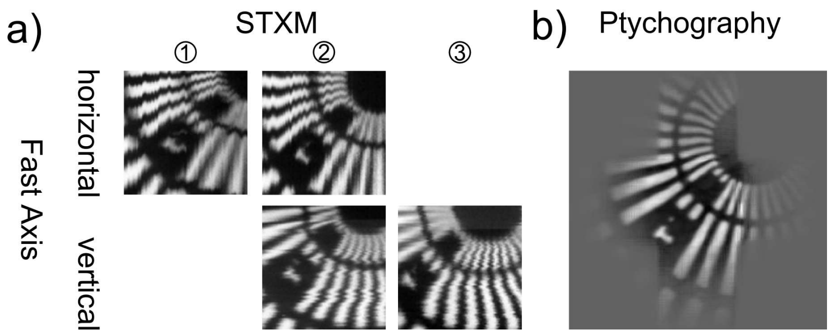

Figure 5.22: a) 1, 2 and 3 show STXM PIN diode scans for different positions of the sample in the propagation direction of the beam as indicated in Figure 5.20. The used fast axis is indicated in the left column.
b) Ptychographic reconstruction of the same position on the Siemens star.

The size of the illuminated aperture is $\approx$ 40 µm. The diffraction limited spot size of this design using the full physical aperture is 18 nm for a k-factor for a rectangular aperture of 0.88. For the aperture of 40 µm the expected diffraction limited spot size would be 22.7 nm. The measured focal spot sizes are close to this limit.

The working distance of the setup can be measured with the optical microscope of the experimental endstation. The order sorting pinhole was moved as close to the lens as possible when other orders started to pass significantly. The microscope is first focused on the pinhole and the then on the sample. The difference in position in the beam direction corresponds to the working distance; with this setup a working distance of 2.5 mm has been achieved. This is less than the nominal working distance for the ideal optic of $\approx$ 3.5 mm, most probably caused by imperfections of the pinhole; however, this is still significantly more than compared to other MLLs [YRS+11].

An efficiency measurements of the two lenses combined was made with the PIN diode. The flux passing through the lenses with adjusted slits as well as with the pinhole in place was measured and compared with the direct flux passing the adjusted slits without any additional optical elements in place. The measured combined efficiency for both lenses is 21 %. This corresponds to an average diffraction efficiency of 46 % the individual MLLs.

Based on the tilt series and the far field diffraction image the potential maximum efficiency for a wedged MLL can be estimated. This can be done by the calculation of the maximum intensity projection and comparing the intensity in the first diffraction order to the unmodified beam similar to the rocking efficiency analysis similar to the evaluation in sections 5.3

and 5.4. This would result in a potential increase of the effective intensity of 20 % − 25 % of one lens and in a total efficiency of approximately 60 %. Two lenses would thus have a total efficiency of 36 % at the energy of 12.7 keV.

6 Summary

The main goal of the work for this thesis was the development and enhancement of multilayer Laue lenses (MLLs) as hard X-ray optics for high resolution X-ray microscopy with a large flux on the sample and large working distances.
One of the major limiting factors for the manufacturing process in order to achieve large numerical apertures is the residual stress in the multilayer stack. The maximum stable multilayer thickness has been significantly increased by the use of a new material system for MLLs based on molybdenum and silicon as absorber and spacer, respectively, and carbon as the transition layer. Based on this material system MLL depositions with a thickness of 50 µm have been made. Test depositions with a larger thickness of up to approximately 90 µm have also been made. The latest flat MLL features a working distance of more than 3 mm and a measured working distance of 2 mm as well as a maximum efficiency of 45% at a photon energy of 12.7 keV for a lens. This working distance and efficiency exceed previously measured ones.
In order to achieve an artifact-free focus only a small deviation from the period thicknesses given by the zone plate law is permissible. The accuracy has been improved in order to achieve a nearly diffraction limited focal spot size as compared to previous results. The best MLLs have shown a width of their focal profiles of less than 25 nm in horizontal and vertical directions. Focusing using crossed wedged MLLs made by a stress layer deposition has been demonstrated with different pair of lenses for the first time.
In order to analyse the bending of MLLs a reference sample free method has been developed. This method used the X-ray diffraction patterns which are compared the calculated MLL properties. This allows to gather additional information of an MLL, which are not available by other methods such as SEM or TEM.
By systematic calculations using the Beam Propagation Method and other methods the tolerable layer placement error as well as the necessary accuracy for the angular alignment of two lenses has been analyzed.
Calculations of MLLs with different numerical apertures, smallest zone widths and flat, tilted and wedged geometries have been made. The expected best focal spot sizes using tilted lenses is in the order of 5 nm to 10 nm. For wedged MLL the even distribution of the diffraction efficiency is limited to zone widths above 1.5 nm to 2 nm. This will also limit the resolution, which can be achieved by wedged geometry MLLs with optimum efficiency. Based on the estimation currently the best focal size with optimal performance is expected to be around 5 nm with a wedged MLL.
However the calculations have shown, that MLLs/FZPs with small section thicknesses will always allow achieving high resolutions while sacrificing the efficiency.

The dynamic diffraction effects also limit the efficiency of tilted MLL for photon energies significantly above 25 keV. The efficiencies “saturate” due to dynamic diffraction effects. These energies, in particular, will require wedged or curved geometries in order to exploit the superior properties of MLLs.

Outlook

For smaller focal spot sizes or increased experimental capabilities there is still “Plenty of Room at the Bottom” [Fey59] and MLLs are *the* optics with further significant potential of improvement in terms of resolution, efficiency and user sample handling.
Currently one of the driving forces for improvements in synchrotron beamline setups is the possibility of in-situ measurements. These are expected to have massive impact on several fields, such as materials science and energy storage. Within the Long Term Project at ESRF an in-situ indentation device and a high temperature chamber have been discussed to be used within an MLL setup. However other applications, such as in-situ analysis of chemical reactions in charging and discharging batteries raise greatest interest. This demand requires the development of optics, which can accomodate a bulkier sample environment. Therefore working distances in the order of several 10 mm have been discussed. Based on current designs and the expected possible deposition thickness of around 100 µm a resolution in the order of 50 nm can be achieved. This would allow to use MLLs as “workhorses” at many synchrotron end stations and greatly enhance experiment capabilities.
Alternatively making MLL depositions with a thickness of 100 µm and more and simultaneously adopt a short working distance also allows to achieve resolutions in the range of 5 nm and less if deployed as wedged MLL.
In order to achieve true wavelength limited focusing with MLLs it will be necessary to find optimum parameters for the final geometry of the lens. Exploiting dynamic diffraction effects and achieve a maximum diffraction efficiency with the same lens makes it necessary to manufacture curved geometry MLLs.
Many design aspects of MLLs have already been examined and much has been already done in order to understand the impact of imperfections on the beam quality.
However some effects have not been considered yet for a deeper analysis, as they are expected to have only a small impact. For decreasing focal spot sizes and a reduced depth of focus some of them should be considered to be analyzed. Especially the difference in focal length between design and actual calculations should be examined closer to estimate the impact on resolution and efficiency. Further possible calculations include the study of deviations from the optimum shape, which are caused by imperfect FIB milling as well as the skew alignment relatively to the incoming beam. These effects are not expected to currently have a significant impact, but will be of more relavance for sub 5 nm resolution MLLs.
Furthermore it could be analyzed, how different zone widths profit from different Γ-ratios. This could lead to a further optimization of the total diffraction efficiency.
Beyond focusing applications MLLs are also of interest for full field imaging. However further work is necessary in order to achieve improved resolutions.

Bibliography

[Abb73] Ernst Abbe. Beiträge zur Theorie des Mikroskops und der mikroskopischen Wahrnehmnung. *Archiv für mikroskopische Anatomie*, 9:413–418, 1873.

[AKB15] Andrzej Andrejczuk, Jacek Krzywinski, and Saša Bajt. Influence of imperfections in a wedged multilayer laue lens for the focusing of x-rays investigated by beam propagation method. *Nuclear Instruments and Methods in Physics Research Section B: Beam Interactions with Materials and Atoms*, 2015.

[APS+16] Lucia Alianelli, Ian Pape, John P Sutter, Oliver JL Fox, Kawal JS Sawhney, and Katarzyna Korwin-Mikke. Aberration-free x-ray lenses made of silicon. In *Society of Photo-Optical Instrumentation Engineers (SPIE) Conference Series*, volume 9963, 2016.

[Att07] David Attwood. *Soft x-rays and extreme ultraviolet radiation: principles and applications*. Cambridge university press, 2007.

[BDN+00] JB Bates, NJ Dudney, B Neudecker, A Ueda, and CD Evans. Thin-film lithium and lithium-ion batteries. *Solid State Ionics*, 135(1):33–45, 2000.

[Ber08] Sylvia Berryman. Ancient atomism. *Stanford Encyclopedia of Philosophy*, 2008.

[BFvL+03] Stefan Braun, Thomas Foltyn, Ludwig van Loyen, Matthew Moss, and Andreas Leson. Multi component euv multilayer mirrors. In *Proceedings of SPIE*, volume 5037, pages 274–285, 2003.

[BKG+15] Stefan Braun, Adam Kubec, Peter Gawlitza, Maik Menzel, and Andreas Leson. Low-stress coatings for sputtered-sliced fresnel zone plates and multilayer laue lenses. In *SPIE Optics+ Optoelectronics*, pages 95100L–95100L. International Society for Optics and Photonics, 2015.

[BKM+13] Stefan Braun, Adam Kubec, Maik Menzel, Sven Niese, Peter Krüger, Frank Seiboth, Jens Patommel, and Christian Schroer. Multilayer laue lenses with focal length of 10 mm. In *Journal of Physics: Conference Series*, volume 425, page 052019. IOP Publishing, 2013.

[BMM+02] Stefan Braun, Hermann Mai, Matthew Moss, Roland Scholz, and Andreas Leson. Mo/si multilayers with different barrier layers for applications as extreme ultraviolet mirrors. *Japanese Journal of Applied Physics*, 41(6S):4074, 2002.

[Bou15] Nathalie Bouet. personal communication, SRI New York City, 2015.

[BQG86] Gerd Binnig, Calvin F Quate, and Ch Gerber. Atomic force microscope. *Physical review letters*, 56(9):930, 1986.

[Bra04] Stefan Braun. *Gefüge- und Grenzflächenbeschaffenheit von Mo/Si-Multischichten, synthetisiert mittels Puls-Laser-und Magnetron-Sputter-Deposition: Spiegel für extrem ultraviolette Strahlung.* PhD thesis, Universität Bielefeld, 2004.

[Bra17] Stefan Braun. personal communication, 2011-2017.

[Bun17] Die nächste Phase der Energiewende kann beginnen. `https://www.bmwi.de/Redaktion/DE/Dossier/energiewende.html`, 2017. Accessed: 2017-08-11.

[BW13] Max Born and Emil Wolf. *Principles of optics: electromagnetic theory of propagation, interference and diffraction of light*. Elsevier, 2013.

[CBB+09] Ray Conley, Nathalie Bouet, James Biancarosa, Qun Shen, Larry Boas, John Feraca, and Leonard Rosenbaum. The nsls-ii multilayer laue lens deposition system. In *SPIE Optical Engineering+ Applications*, pages 74480U–74480U. International Society for Optics and Photonics, 2009.

[CBC+16] Ray Conley, Nathalie Bouet, Yong S Chu, Xiaojing Huang, Hyon Chol Kang, Albert T Macrander, Jörg Maser, Evgeny Nazaretski, G Brian Stephenson, and Hanfei Yan. Multilayer laue lens: A brief history and current status. *Synchrotron Radiation News*, 29(4):16–20, 2016.

[CBZ+12] Ray Conley, Nathalie Bouet, Juan Zhou, Hanfei Yan, Yong Chu, Kenneth Lauer, Jesse Miller, Luke Chu, and Nima Jahedi. Advanced multilayer laue lens fabrication at NSLS-II. In *SPIE Optical Engineering+ Applications*, pages 850202–850202. International Society for Optics and Photonics, 2012.

[Cha00] Christopher Thomas Chantler. Detailed tabulation of atomic form factors, photoelectric absorption and scattering cross section, and mass attenuation coefficients in the vicinity of absorption edges in the soft x-ray (z= 30–36, z= 60–89, e= 0.1 kev–10 kev), addressing convergence issues of earlier work. *Journal of Physical and Chemical Reference Data*, 29(4):597–1056, 2000.

[Chu15] Yong Chu. Synchrotron Radiation Instruments Conference, New York, 2015.

[CLQ+08] Ray Conley, Chian Liu, Jun Qian, Cameron M Kewish, Albert T Macrander, Hanfei Yan, Hyon Chol Kang, Jörg Maser, and G Brian Stephenson. Wedged multilayer laue lens. *Review of Scientific Instruments*, 79(5):053104, 2008.

[Con14] Raymond Conley. personal communication, 2014.

[DES17] Proposal types at desy photon science. `https://photon-science.de/users_area/user_guide/select_the_proposal_type/index_eng.html`, 2017. Accessed: 2017-08-14.

[DSPY+17] Julio Cesar Da Silva, Alexandra Pacureanu, Yang Yang, Sylvain Bohic, Christian Morawe, Raymond Barrett, and Peter Cloetens. Efficient concentration of high-energy x-rays for diffraction-limited imaging resolution. *Optica*, 4(5):492–495, 2017.

[DVC+17] Junjing Deng, David J Vine, Si Chen, Qiaoling Jin, Youssef SG Nashed, Tom Peterka, Stefan Vogt, and Chris Jacobsen. X-ray ptychographic and fluorescence microscopy of frozen-hydrated cells using continuous scanning. *Scientific Reports*, 7, 2017.

[EDA+16] Elena Eggl, Martin Dierolf, Klaus Achterhold, Christoph Jud, Benedikt Günther, Eva Braig, Bernhard Gleich, and Franz Pfeiffer. The munich compact light source: initial performance measures. *Journal of synchrotron radiation*, 23(5):1137–1142, 2016.

[EODK15] Christian Eberl, Markus Osterhoff, Florian Döring, and Hans-Ulrich Krebs. Mzp design and fabrication for efficient hard x-ray nano-focusing and imaging. In *SPIE Optical Engineering+ Applications*, pages 958808–958808. International Society for Optics and Photonics, 2015.

[EP02] Winfried Elliger and Karlheinz Pirker. *Kantharos: griechisches Unterrichtswerk. Lese-und Arbeitsbuch.* Ernst Klett Schulbuchverlag Leipzig, 2002.

[ESR17] Apply for ESRF beamtime. `https://www.esrf.eu/UsersAndScience/UserGuide/Applying`, 2017. Accessed: 2017-08-14.

[Fey59] Richard Feynmann. Talk: Plenty of room at the bottom. `http://www.its.caltech.edu/~feynman/plenty.html`, 1959. Accessed: 2017-09-06.

[Fre96] Augustin-Jean Fresnel. Calcul de i'intensite de la lumiere au centre de l'ombre d'un ecran et d'une ouverture circulaires eclairepar un point radieux. *SPIE MILESTONE SERIES MS*, 128:3–10, 1996.

[GB65] Galileo Galilei and Hans Blumenberg. Sidereus nuncius, Nachricht von neuen Sternen. *Frankfurt am Main, Insel-Verlag*, 1965.

[GBLL06] Peter Gawlitza, Stefan Braun, Sebastian Lipfert, and Andreas Leson. Ion-beam sputter deposition of x-ray multilayer optics on large areas. In *SPIE Optics+ Photonics*, pages 63170G–63170G. International Society for Optics and Photonics, 2006.

[Goo17] Source for bibliography data: Google scholar. `http://scholar.google.de`, 2017.

[GSS+10] Gianluca Geloni, E Saldin, L Samoylova, E Schneidmiller, H Sinn, Th Tschentscher, and M Yurkov. Coherence properties of the european xfel. *New Journal of Physics*, 12(3):035021, 2010.

[GWL+14] Sophie-Charlotte Gleber, Michael Wojcik, Jie Liu, Chris Roehrig, Marvin Cummings, Joan Vila-Comamala, Kenan Li, Barry Lai, Deming Shu, and Stefan Vogt. Fresnel zone plate stacking in the intermediate field for high efficiency focusing in the hard x-ray regime. *Optics express*, 22:28142–28153, 2014.

[HCB+15] Xiaojing Huang, Raymond Conley, Nathalie Bouet, Juan Zhou, Albert Macrander, Jorg Maser, Hanfei Yan, Evgeny Nazaretski, Kenneth Lauer, Ross Harder, et al. Achieving hard x-ray nanofocusing using a wedged multilayer laue lens. *Optics Express*, 23(10):12496–12507, 2015.

[HDMB00] Thomas Holz, Rainer Dietsch, H Mai, and L Brügemann. Application of Ni/C Göbel mirrors. In *Materials Science Forum*, volume 321, pages 179–183. Trans Tech Publ, 2000.

[Hec09] Eugene Hecht. Optik. 5., verbesserte Auflage, 2009.

[hen17] X-ray interactions with matter database. `http://henke.lbl.gov/optical_constants/`, 2017. Accessed: 2017-05-02.

[HGD93] Burton L Henke, Eric M Gullikson, and John C Davis. X-ray interactions: photoabsorption, scattering, transmission, and reflection at e= 50-30,000 ev, z= 1-92. *Atomic data and nuclear data tables*, 54(2):181–342, 1993.

[HHP+11] Susanne Hönig, Robert Hoppe, Jens Patommel, Andreas Schropp, Sandra Stephan, Sebastian Schöder, Manfred Burghammer, and Christian G Schroer. Full optical characterization of coherent x-ray nanobeams by ptychographic imaging. *Optics Express*, 19(17):16324–16329, 2011.

[HSMH66] HE Hart, JB Scrandis, R Mark, and RD Hatcher. Diffraction characteristics of a linear zone plate. *JOSA*, 56(8):1018–1023, 1966.

[HW94] Stefan W Hell and Jan Wichmann. Breaking the diffraction resolution limit by stimulated emission: stimulated-emission-depletion fluorescence microscopy. *Optics letters*, 19(11):780–782, 1994.

[HYN+13] Xiaojing Huang, Hanfei Yan, Evgeny Nazaretski, Raymond Conley, Nathalie Bouet, Juan Zhou, Kenneth Lauer, Li Li, Daejin Eom, Daniel Legnini, et al. 11 nm hard x-ray focus from a large-aperture multilayer laue lens. *Scientific reports*, 3:3562, 2013.

[KA00] PJ Kelly and RD Arnell. Magnetron sputtering: a review of recent developments and applications. *Vacuum*, 56(3):159–172, 2000.

[KB48] Paul Kirkpatrick and Albert Vincio Baez. Formation of optical images by x-rays. *JOSA*, 38(9):766–774, 1948.

[KBG+16] Adam Kubec, Stefan Braun, Peter Gawlitza, Maik Menzel, Andreas Leson, Qun Shen, and Christie Nelson. Calculated efficiencies of three-material low stress coatings for diffractive x-ray transmission optics. In *AIP Conference Proceedings*, volume 1741, page 040010. AIP Publishing, 2016.

[KBN+14a] Adam Kubec, Stefan Braun, Sven Niese, Peter Krüger, Jens Patommel, Michael Hecker, Andreas Leson, and Christian G Schroer. Ptychography with multilayer laue lenses. *Journal of Synchrotron Radiation*, 21(5), 2014.

[KBN+14b] Adam Kubec, Stefan Braun, Sven Niese, J Patommel, and K Melzer. Hard x-ray focusing by multilayer laue lenses with focal lengths >10 mm. *ESRF experimental report*, 2014.

[KGSL+10] Cameron M Kewish, Manuel Guizar-Sicairos, Chian Liu, Jun Qian, Bing Shi, Christa Benson, Ali M Khounsary, Joan Vila-Comamala, Oliver Bunk, James R Fienup, et al. Reconstruction of an astigmatic hard x-ray beam and alignment of kb mirrors from ptychographic coherent diffraction data. *Optics express*, 18(22):23420–23427, 2010.

[KIT+08] Takahisa Koyama, Satoshi Ichimaru, Takuya Tsuji, Hidekazu Takano, Yasushi Kagoshima, Tadayuki Ohchi, and Hisataka Takenaka. Optical properties of mosi2/si multilayer laue lens as nanometer x-ray focusing device. *Applied Physics Express*, 1(11):117003, 2008.

[KK86] R Kosloff and D Kosloff. Absorbing boundaries for wave propagation problems. *Journal of Computational Physics*, 63(2):363–376, 1986.

[KKC+15] Adam Kubec, Naresh Kujala, Raymond Conley, Nathalie Bouet, Juan Zhou, Tim M Mooney, Deming Shu, Jeffrey Kirchman, Kurt Goetze, Jörg Maser, and Albert Macrander. Diffraction properties of multilayer laue lenses with an aperture of 102 μm and wsi 2/al bilayers. *Optics Express*, 23(21):27990–27997, 2015.

[KMF+17] Adam Kubec, Jörg Maser, Petr Formánek, Volker Franke, Stefan Braun, Peter Gawlitza, Andreas Leson, and Albert Macrander. Fabrication and efficiency measurement of a mo/c/si/c three material system multilayer laue lens. *Applied Physics Letters*, 110(11):111905, 2017.

[KMG+17] Adam Kubec, Kathleen Melzer, Jürgen Gluch, Sven Niese, Stefan Braun, Jens Patommel, M Burghammer, and A Leson. Point focusing with flat and wedged crossed multilayer laue lenses. *Journal of Synchrotron Radiation*, 24(2), 2017.

[KMN+14] Adam Kubec, Kathleen Melzer, Sven Niese, Stefan Braun, and Jens Patommel. Focusing properties of crossed wedged multilayer laue lenses. *ESRF experimental report*, 2014.

[KMS+06] HC Kang, J Maser, GB Stephenson, C Liu, R Conley, AT Macrander, and S Vogt. Nanometer linear focusing of hard x rays by a multilayer laue lens. *Physical Review Letters*, 96(12):127401, 2006.

[KN17] Peter Krüger and Sven Niese. Calculations by Sven Niese during a ESRF beam time in january 2017, 2017. Fraunhofer IKTS and AXO Dresden GmbH internal Software.

[KRM+14] Kahraman Keskinbora, Anna-Lena Robisch, Marcel Mayer, Umut T Sanli, Corinne Grévent, Christian Wolter, Markus Weigand, Adriana Szeghalmi, Mato Knez, Tim Salditt, and Gisela Schütz. Multilayer fresnel zone plates for high energy radiation resolve 21 nm features at 1.2 kev. *Optics express*, 22(15):18440–18453, 2014.

[KS95] Masaki Koike and Isao H Suzuki. Nanofabrication of multilayer zone plates by helicon plasma sputtering. *Japanese journal of applied physics*, 34(12S):6754, 1995.

[KSJ+01] L Kipp, M Skibowski, RL Johnson, R Berndt, et al. Sharper images by focusing soft x-rays with photon sieves. *Nature*, 414(6860):184, 2001.

[KSL+04] Hyon Chol Kang, Gregory B Stephenson, Chian Liu, Ray Conley, Albert T Macrander, Jorg Maser, Sasa Bajt, and Henry N Chapman. Synchrotron x-ray study of multilayers in laue geometry. In *Optical Science and Technology, the SPIE 49th Annual Meeting*, pages 127–132. International Society for Optics and Photonics, 2004.

[KSL+05] HC Kang, GB Stephenson, C Liu, R Conley, AT Macrander, J Maser, S Bajt, and HN Chapman. High-efficiency diffractive x-ray optics from sectioned multilayers. *Applied physics letters*, 86(15):151109, 2005.

[KSL+07] Hyon Chol Kang, G Brian Stephenson, Chian Liu, Ray Conley, Ruben Khachatryan, Michael Wieczorek, Albert T Macrander, Hanfei Yan, Jörg Maser, Jon Hiller, and Rachel Koritala. Sectioning of multilayers to make a multilayer laue lens. *Review of scientific instruments*, 78(4):046103, 2007.

[KTK84] K Kodate, H Takenaka, and Takeshi Kamiya. Fabrication of high numerical aperture zone plates using deep ultraviolet lithography. *Applied Optics*, 23:504–507, 1984.

[KTK+12] Takahisa Koyama, Hidekazu Takano, Shigeki Konishi, Takuya Tsuji, Hisataka Takenaka, Satoshi Ichimaru, Tadayuki Ohchi, and Yasushi Kagoshima. Circular multilayer zone plate for high-energy x-ray nano-imaging. *Review of Scientific Instruments*, 83(1):013705, 2012.

[KTT+11] T Koyama, T Tsuji, H Takano, Y Kagoshima, S Ichimaru, T Ohchi, H Takenaka, Ian McNulty, Catherine Eyberger, and Barry Lai. Development of multilayer laue lenses;(2) circular type. In *AIP Conference Proceedings*, volume 1365, pages 100–103. AIP, 2011.

[KvB01] R. Klockenkämper and A. von Bohlen. Elemental analysis of environmental samples by total reflection x-ray fluorescence: a review, 1996-07-01.

[KYW+08] Hyon Chol Kang, Hanfei Yan, Robert P Winarski, Martin V Holt, Jörg Maser, Chian Liu, Ray Conley, Stefan Vogt, Albert T Macrander, and G Brian Stephenson. Focusing of hard x-rays to 16 nanometers with a multilayer laue lens. *Applied Physics Letters*, 92:221114, 2008.

[LHW+14] Keliang Liao, Youli Hong, Qiushi Wang, Guangcai Chang, and Weifan Sheng. Analysis of tilted multilayer laue lens with stochastic layer thickness error. *Optics Communications*, 325:111–115, 2014.

[Lis17] List of light sources. `http://www.lightsources.org/regions`, 2017. Accessed: 2017-05-03.

[LM90] Paolo Luchini and Hans Motz. *Undulators and free-electron lasers*. Clarendon Press, 1990.

[Mas94] Jörg Maser. *Theoretische Beschreibung der Beugungs-und Abbildungseigenschaften hochauflösender Zonenplatten für die Röntgenmikroskopie*. PhD thesis, Universität Göttingen, 1994.

[Mas17] Jörg Maser. personal communication, 2014-2017.

[MCD+11] Francesca Mastropietro, D Carbone, A Diaz, J Eymery, Anne Sentenac, TH Metzger, Virginie Chamard, and Vincent Favre-Nicolin. Coherent x-ray wavefront reconstruction of a partially illuminated fresnel zone plate. *Optics express*, 19(20):19223–19232, 2011.

[Mes99] Dieter Meschede. *Optik, Licht und Laser*. Teubner, 1999.

[MHK+10] Hidekazu Mimura, Soichiro Handa, Takashi Kimura, Hirokatsu Yumoto, Daisuke Yamakawa, Hikaru Yokoyama, Satoshi Matsuyama, Kouji Inagaki, Kazuya Yamamura, Yasuhisa Sano, et al. Breaking the 10 nm barrier in hard-x-ray focusing. *Nature Physics*, 6(2):122–125, 2010.

[MJ51] Ora E Myers Jr. Studies of transmission zone plates. *American Journal of Physics*, 19(6):359–365, 1951.

[MKC+15] Albert T Macrander, Adam Kubec, Raymond Conley, Nathalie Bouet, Juan Zhou, Michael Wojcik, and Jorg Maser. Efficiency of a multilayer-laue-lens with a 102 μm aperture. *Applied Physics Letters*, 107(8):081904, 2015.

[Moo06] Gordon E Moore. Cramming more components onto integrated circuits, reprinted from electronics, volume 38, number 8, april 19, 1965, pp. 114 ff. *IEEE Solid-State Circuits Society Newsletter*, 20(3):33–35, 2006.

[MPA+15] Andrew J Morgan, Mauro Prasciolu, Andrzej Andrejczuk, Jacek Krzywinski, Alke Meents, David Pennicard, Heinz Graafsma, Anton Barty, Richard J Bean, Miriam Barthelmess, Dominik Oberthuer, Oleksandr Yefanov, Andrew Aquila, Henry N. Chapman, and Saša Bajt. High numerical aperture multilayer laue lenses. *Scientific reports*, 5, 2015.

[MS92] Jörg Maser and Günter Schmahl. Coupled wave description of the diffraction by zone plates with high aspect ratios. *Optics Communications*, 89(2-4):355–362, 1992.

[MSV+04] Joerg Maser, Gregory B Stephenson, Stefan Vogt, Wenbing Yun, Albert Macrander, Hyon C Kang, Chian Liu, and Ray Conley. Multilayer laue lenses as high-resolution x-ray optics. In *Optical Science and Technology, the SPIE 49th Annual Meeting*, pages 185–194. International Society for Optics and Photonics, 2004.

[MVR+17] Istvan Mohacsi, Ismo Vartiainen, Benedikt Rösner, Manuel Guizar-Sicairos, Vitaliy A Guzenko, Ian McNulty, Robert Winarski, Martin V Holt, and Christian David. Interlaced zone plate optics for hard x-ray imaging in the 10 nm range. *Scientific Reports*, 7, 2017.

[NBD+16] Sven Niese, Stefan Braun, Reiner Dietsch, Jürgen Gluch, Thomas Holz, Norman Huber, Adam Kubec, Ehrenfried Zschech, Juergen Thieme, and D Peter Siddons. A dedicated illumination for full-field x-ray microscopy with multilayer laue lenses. In *AIP Conference Proceedings*, volume 1764, page 020002. AIP Publishing, 2016.

[NBG+18] Sven Niese, Manfred Burghammer, Jürgen Gluch, Thomas Holz, Jozef Keckes, Martin Rosenthal, Juraj Todt, and Adam Kubec. Combined point and line focus experiments with multilayer laue lenses. *to be published*, 2018. in preparation.

[Nie15] Sven Niese. *Lab-based in-situ X-ray Microscopy–Methodical Developments and Applications in Materials Science and Microelectronics*. PhD thesis, Brandenburgische Technische Universität Cottbus, 2015.

[NKK+14a] Sven Niese, Peter Krüger, Adam Kubec, Stefan Braun, Jens Patommel, Christian G Schroer, Andreas Leson, and Ehrenfried Zschech. Full-field x-ray microscopy with crossed partial multilayer laue lenses. *Optics express*, 22(17):20008–20013, 2014.

[NKK+14b] Sven Niese, Peter Krüger, Adam Kubec, Roman Laas, Peter Gawlitza, Kathleen Melzer, Stefan Braun, and Ehrenfried Zschech. Fabrication of customizable wedged multilayer laue lenses by adding a stress layer. *Thin Solid Films*, 571:321–324, 2014.

[Nob14] Nobel prize in chemistry for 2014. `https://www.nobelprize.org/nobel_prizes/chemistry/laureates/2014/press.html`, 2014. Accessed: 2017-03-29.

[PKH+17] Jens Patommel, Susanne Klare, Robert Hoppe, Stephan Ritter, Dirk Samberg, Felix Wittwer, Andreas Jahn, Karola Richter, Christian Wenzel, Johann W Bartha, Maria Scholz, Ulrike Seiboth, Frank an Boesenberg, Gerald Falkenberg, and Christian G Schroer. Focusing hard x rays beyond the critical angle of total reflection by adiabatically focusing lenses. *Applied Physics Letters*, 110(10):101103, 2017.

[PLK+15] M Prasciolu, AFG Leontowich, J Krzywinski, A Andrejczuk, HN Chapman, and S Bajt. Fabrication of wedged multilayer laue lenses. *Optical Materials Express*, 5(4):748–755, 2015.

[Pra14] Mauro Prasciolu. personal communication, DESY Photon Science User Meeting 2014, Hamburg, 2014.

[PS16] Ljiljana Puskar and Ulrich Schade. The IRIS thz/infrared beamline at BESSY II. *Journal of large-scale research facilities JLSRF*, 2:95, 2016.

[RNS82] Dietbert Rudolph, Bastian Niemann, and Günter Schmahl. Status of the sputtered sliced zone plates for x-ray microscopy. In *1981 Brookhaven Conferences*, pages 103–105. International Society for Optics and Photonics, 1982.

[Rön98] Wilhelm Conrad Röntgen. Ueber eine neue Art von Strahlen. *Annalen der Physik*, 300(1):1–11, 1898.

[RS80] Dietbert Rudolph and Günter Schmahl. High power zone plates for a soft x-ray microscope. *Annals of the New York Academy of Sciences*, 342:94–104, 1980.

[Rum13] Raymond Rumpf. Beam propagation method. University Lecture, 2013.

[Sch11] Christian Schroer. Röntgenmikroskopie. University Lecture, 2011.

[Sch18] Katrin Schönemann. *Der Einfluß verschiedener Lagerlösungen auf die Gefäßfunktion von humanem Vena saphena-Gefäßsegmenten nach Kurzzeitlagerung*. PhD thesis, Technische Universität Dresden, 2018.

[SKB+14] Norbert Schell, Andrew King, Felix Beckmann, Torben Fischer, Martin Müller, and Andreas Schreyer. The high energy materials science beamline (HEMS) at PETRA III. In *Materials Science Forum*, volume 772, pages 57–61. Trans Tech Publ, 2014.

[SKP+05] Christian G Schroer, Olga Kurapova, Jens Patommel, Pit Boye, Jan Feldkamp, Bruno Lengeler, Manfred Burghammer, Christian Riekel, Laszlo Vincze, Andre van der Hart, et al. Hard x-ray nanoprobe based on refractive x-ray lenses. *Applied Physics Letters*, 87:124103, 2005.

[SKSL96] Anatoly Snigirev, Victor Kohn, Irina Snigireva, and Bruno Lengeler. A compound refractive lens for focusing high-energy x-rays. *Nature*, 384(6604):49, 1996.

[SM83] MJ Simpson and AG Michette. The effects of manufacturing inaccuracies on the imaging properties of fresnel zone plates. *Journal of Modern Optics*, 30(10):1455–1462, 1983.

[SMM+14] Bing Shi, Albert T Macrander, Jörg Maser, Raymond Conley, and Lahsen Assoufid. The effect of unequal bilayer thickness on stress in WSi2/Si multilayers for multilayer laue lens structures. In *SPIE Optical Engineering+ Applications*, pages 920708–920708. International Society for Optics and Photonics, 2014.

[Son09] G Gerald Sontey. The tension of metallic films deposited by electrolysis. *Proceedings of the Royal Society of London. Series A, Containing Papers of a Mathematical and Physical Character*, 82(553):172–175, 1909.

[SSS+17] Frank Seiboth, Andreas Schropp, Maria Scholz, Felix Wittwer, Christian Rödel, Martin Wünsche, Tobias Ullsperger, Stefan Nolte, Jussi Rahomäki, Karolis Parfeniukas, et al. Perfect x-ray focusing via fitting corrective glasses to aberrated optics. *Nature Communications*, 8:14623, 2017.

[TDB+09] Pierre Thibault, Martin Dierolf, Oliver Bunk, Andreas Menzel, and Franz Pfeiffer. Probe retrieval in ptychographic coherent diffractive imaging. *Ultramicroscopy*, 109(4):338–343, 2009.

[The17] The telescope. `https://galileo.rice.edu/sci/instruments/telescope.html`, 2017. Accessed: 2017-08-1.

[TIO+09] H Takenaka, S Ichimaru, T Ohchi, T Koyama, T Tsuji, H Takano, and Y Kagoshima. Mo/Si and MoSi2/Si nanostructures for multilayer laue lens. In *Journal of Physics: Conference Series*, volume 186, page 012074. IOP Publishing, 2009.

[VCGF+11] Joan Vila-Comamala, Sergey Gorelick, Elina Färm, Cameron M Kewish, Ana Diaz, Ray Barrett, Vitaliy A Guzenko, Mikko Ritala, and Christian David. Ultra-high resolution zone-doubled diffractive x-ray optics for the multi-kev regime. *Optics Express*, 19(1):175–184, 2011.

[VCJR+09] Joan Vila-Comamala, Konstantins Jefimovs, Jörg Raabe, Tero Pilvi, Rainer H Fink, Mathias Senoner, Andre Maaßdorf, Mikko Ritala, and Christian David. Advanced thin film technology for ultrahigh resolution x-ray microscopy. *Ultramicroscopy*, 109(11):1360–1364, 2009.

[VWB+11] Gavin BM Vaughan, Jonathan P Wright, Aleksei Bytchkov, Michel Rossat, Henri Gleyzolle, Irina Snigireva, and Anatoly Snigirev. X-ray transfocators: focusing devices based on compound refractive lenses. *Journal of synchrotron radiation*, 18(2):125–133, 2011.

[Wei17] Katja Weise. *Gezähmte Kleider, gebändigte Körper? - Kleidermoden im Museum sehend spüren. Der Einfluss von Präsentationsmitteln auf ästhetische Erfahrungen zwischen Visuellem und Hautsinnlichen.* PhD thesis, Universität Potsdam, 2017.

[Wel86] Walter Thompson Welford. *Aberrations of optical systems.* IOP Publishing Ltd, 1986.

[WH10] Christian Wagner and Noreen Harned. Euv lithography: Lithography gets extreme. *Nature Photonics*, 4(1):24–26, 2010.

[Win00] David L Windt. Stress, microstructure, and stability of Mo/Si, W/Si, and Mo/C multilayer films. *Journal of Vacuum Science & Technology A: Vacuum, Surfaces, and Films*, 18(3):980–991, 2000.

[Win07] David L Windt. Reduction of stress and roughness by reactive sputtering in w/b4c multilayer films. In *Optical Engineering+ Applications*, pages 66880R–66880R. International Society for Optics and Photonics, 2007.

[WRG+09] S Werner, S Rehbein, P Guttman, S Heim, and G Schneider. Towards stacked zone plates. In *Journal of Physics: Conference Series*, volume 186, page 012079. IOP Publishing, 2009.

[WRGS14] Stephan Werner, Stefan Rehbein, Peter Guttmann, and Gerd Schneider. Three-dimensional structured on-chip stacked zone plates for nanoscale x-ray imaging with high efficiency. *Nano Research*, 7:528–535, 2014.

[Yan93] BX Yang. Fresnel and refractive lenses for x-rays. *Nuclear Instruments and Methods in Physics Research Section A: Accelerators, Spectrometers, Detectors and Associated Equipment*, 328(3):578–587, 1993.

[Yan09] Hanfei Yan. X-ray dynamical diffraction from multilayer laue lenses with rough interfaces. *Physical Review B*, 79(16):165410, 2009.

[Yan13] Hanfei Yan. Talk at ICXOM Hamburg, 2013.

[YC13] Hanfei Yan and Yong S Chu. Optimization of multilayer laue lenses for a scanning x-ray microscope. *Journal of Synchrotron Radiation*, 20(1):89–97, 2013.

[YCBC14] Hanfei Yan, Ray Conley, Nathalie Bouet, and Yong S Chu. Hard x-ray nanofocusing by multilayer laue lenses. *Journal of Physics D: Applied Physics*, 47(26):263001, 2014.

[YCM+13] Hanfei Yan, Yong S Chu, Jörg Maser, Evgeny Nazaretski, Jungdae Kim, Hyon Chol Kang, Jeffrey J Lombardo, and Wilson KS Chiu. Quantitative x-ray phase imaging at the nanoscale by multilayer laue lenses. *Scientific Reports*, 3, 2013.

[YHB+17] Hanfei Yan, Xiaojing Huang, Nathalie Bouet, Juan Zhou, Evgeny Nazaretski, and Yong S Chu. Achieving diffraction-limited nanometer-scale x-ray point focus with two crossed multilayer laue lenses: alignment challenges. *Optics Express*, 25(21):25234–25242, 2017.

[YMK+08] Hanfei Yan, Jorg Maser, Hyon Chol Kang, Albert Macrander, and Brian Stephenson. A theoretical study of two-dimensional point focusing by two multilayer laue lenses. In *Optical Engineering+ Applications*, pages 70770Q–70770Q. International Society for Optics and Photonics, 2008.

[YMK+13] Hirokatsu Yumoto, Hidekazu Mimura, Takahisa Koyama, Satoshi Matsuyama, Kensuke Tono, Tadashi Togashi, Yuichi Inubushi, Takahiro Sato, Takashi Tanaka, Takashi Kimura, et al. Focusing of x-ray free-electron laser pulses with reflective optics. *Nature Photonics*, 7(1):43–47, 2013.

[YMM+07] Hanfei Yan, Jörg Maser, Albert Macrander, Qun Shen, Stefan Vogt, G Brian Stephenson, and Hyon Chol Kang. Takagi-taupin description of x-ray dynamical diffraction from diffractive optics with large numerical aperture. *Physical Review B*, 76(11):115438, 2007.

[YRS+11] Hanfei Yan, Volker Rose, Deming Shu, Enju Lima, Hyon Chol Kang, Ray Conley, Chian Liu, Nima Jahedi, Albert T Macrander, G Brian Stephenson, Martin Holt, Yong S Chu, Ming Lu, and Jörg Maser. Two dimensional hard x-ray nanofocusing with crossed multilayer laue lenses. *Optics Express*, 19(16):15069–15076, 2011.

[ZHLW11] Jingtao Zhu, Qiu Huang, Haichuan Li, and Zhanshan Wang. Hard x-ray micro-focus multi-thickness-ratio composite multi-layer film laue lens, 2011. China patent: CN 103151089 A.

[ZKK97] Anatoliĭ Zvezdin, Konstantinovich, and Viacheslav Alekseevich Kotov. *Modern magnetooptics and magnetooptical materials*. CRC Press, 1997.

[ZXHW15] Xiaonan Zhao, Feng Xu, Jingpei Hu, and Chinhua Wang. Broadband photon sieves imaging with wavefront coding. *Optics express*, 23(13):16812–16822, 2015.

List of publications

Papers (first author)

- Kubec, A., Melzer, K., Gluch, J., Niese, S., Braun, S., Patommel, J., Burghammer, M. and Leson, A. (2017). *Point focusing with flat and wedged crossed multilayer Laue lenses.* Journal of Synchrotron Radiation, 24(2), 413-421.

- Kubec, A., Maser, J., Formánek, P., Franke, V., Braun, S., Gawlitza, P., Leson, A. and Macrander, A. (2017). *Fabrication and efficiency measurement of a Mo/C/Si/C three material system multilayer Laue lens.* Applied Physics Letters, 110(11), 111905.

- Kubec, A., Kujala, N., Conley, R., Bouet, N., Zhou, J., Mooney, T. M., Shu, D., Kirchman, K., Maser, J. and Macrander, A. (2015). *Diffraction properties of multilayer Laue lenses with an aperture of 102 micrometer and WSi_2/Al bilayers.* Optics express, 23(21), 27990-27997.

- Kubec, A., Braun, S., Niese, S., Krüger, P., Patommel, J., Hecker, M., Leson, A. and Schroer, C. G. (2014). *Ptychography with multilayer Laue lenses.* Journal of Synchrotron Radiation 21(5).

Papers (co-author)

- Niese, S., Braun, S., Dietsch, R., Gluch, J., Holz, T., Huber, N., Kubec, A. and Zschech, E. (2016, August). *A dedicated illumination for full-field X-ray microscopy with multilayer Laue lenses.* In AIP Conference Proceedings (Vol. 1764, No. 1, p. 020002). AIP Publishing.

- Macrander, A. T., Kubec, A., Conley, R., Bouet, N., Zhou, J., Wojcik, M., and Maser, J. (2015). *Efficiency of a multilayer-Laue-lens with a 102 micrometer aperture.* Applied Physics Letters, 107(8), 081904.

- Braun, S., Kubec, A., Gawlitza, P., Menzel, M., and Leson, A. (2015, May). *Low-stress coatings for sputtered-sliced Fresnel zone plates and multilayer Laue lenses.* In SPIE Optics+ Optoelectronics (pp. 95100L-95100L). International Society for Optics and Photonics.

- Niese, S., Krüger, P., Kubec, A., Braun, S., Patommel, J., Schroer, C. G., Leson, A. and Zschech, E. (2014). *Full-field X-ray microscopy with crossed partial multilayer Laue lenses.* Optics express, 22(17), 20008-20013.

- Niese, S., Krüger, P., Kubec, A., Laas, R., Gawlitza, P., Melzer, K., Braun, S. and Zschech, E. (2014). *Fabrication of customizable wedged multilayer Laue lenses by adding a stress layer.* Thin Solid Films.

- Braun, S., Kubec, A., Menzel, M., Niese, S., Krüger, P., Seiboth, F., Patommel, J. and Schroer, C. (2013, March). *Multilayer Laue lenses with focal length of 10 mm.* In Journal of Physics: Conference Series (Vol. 425, No. 5, p. 052019). IOP Publishing.

Danksagung

Während der Arbeit an meiner Promotion haben viele direkt oder auch indirekt zum Erfolg beigetragen; gern möchte ich mich an dieser bei Allen bedanken und einige besonders hervorheben:

Prof. Dr. Christian Schroer danke ich für die Möglichkeit im Fachbereich Physik der Universität Hamburg zu promovieren. Prof. Dr. Andreas Leson danke ich für die wissenschaftliche Betreuung dieser Arbeit und die Möglichkeit meinem Interesse an Multischicht Laue Linsen am Fraunhofer IWS in Dresden nachgehen zu können.
Ein sehr großes Danke gilt auch Prof. Dr. Stefan Braun und Peter Gawlitza, die einen großen Teil der wissenschaftlich-technischen Betreuung im IWS übernommen und mit denen sich immer wieder interessante Diskussionen entwickelt haben. Weiterer besonderer Dank gilt Maik Menzel für die Betreuung der und Einweisung in die Pilotanlage und dem D8 und die vielen hilfreichen Diskussion. Jürgen Schmidt und Albert Schmidt würde ich gern für die hervorragende Arbeit in der Werkstatt und die Ideen, wie etwas mechanisch zu machen sei, danken. Auch die Mitglieder aktuellen und ehemaligen Mitglieder der Gruppe *Röntgen und EUV-Optiken* bzw. später der Abteilung *Nanoschichten* William Förster, Kathleen Melzer, Erik Pflug, Wolfgang Friedrich, Christoph Gruhne, Dr. Maximilian Rühl, Georg Dietrich, Dana Zucker und Birgit Schaub haben dazu beigetragen, dass ich am IWS eine bereichernde Zeit hatte.
Für die gute Zusammenarbeit am IWS möchte ich mich des Weiteren auch bei Volker Franke, Niels Friedrich-Schilling, André Reck, Dr. Jörg Bretschneider und Dr. Jörg Kaspar sowie dem Team der Metallografie um Andrea Ostwaldt bedanken.
Die Entwicklung und das Testen der Multischicht Laue Linsen erfolgte in enger Kooperation mit dem Fraunhofer IKTS in Dresden Klotzsche und der AXO Dresden GmbH. Hier würde ich mich gern insbesondere bei Dr. Sven Niese und Dr. Jürgen Gluch für die tolle Zusammenarbeit, die interessanten Diskussionen und die bereichernde Zeit bei den Messzeiten und den gemeinsamen Konferenzaufenthalten bedanken.
Viele Messungen erfolgten und einige Ideen entstanden auch zusammen mit dem Institut für Strukturphysik der Technischen Universität Dresden. Dort möchte ich mich insbesondere bei Dr. Jens Patommel, Dr. Frank Seiboth, Dr. Susanne Klare, Dr. Christoph Baumbach, Stephan Ritter und Dirk Samberg bedanken.
Ein großes Danke geht auch an Dr. Petr Formánek vom Leibniz Institut für Polymerforschung für die kurzfristige Aushilfe bei der Strukturierung.
Vielen Dank auch für die unermüdliche und tolle Betreuung an der ESRF ID13 an Dr. Manfred Burghammer, Dr. Martin Rosenthal, Dr. Tilman Grunewald und Michael Sztucki. An der PETRA III P06 haben uns vor allem Felix Wittwer, Martin Seyrich und Dr. Ulrike

Bösenberg großartig unterstützt.
I cannot leave the great time at the APS unmentioned. A special *thank you* goes to Dr. Jörg Maser, Dr. Albert Macrander und Ramond Conley for the interesting and enriching discussions during my stay there and also lateron. Many thanks also to Dr. Lahsen Assoufid, who made my visit at the APS possible in the first place.
Danke auch an unsere Kooperationspartner aus Leoben, insbesondere Prof. Dr. Jozef Kečkeš, Dr. Nina Schalk, Dr. Juraj Todt und Dr. Michael Tkadletz. Im Rahmen des Long Term Proposals an der ID13 konnten mit den MLLs dann endlich auch mal richtige Proben vermessen werden, und nicht immer nur ein Siemensstern.
Prof. Dr. Stefan Braun, Dr. Sven Niese, Dr. Malte Czernohorsky, Dr. Jürgen Gluch, Dr. Anja Banholzer sowie Samuel Kubec danke ich für das kritische Lesen und Kommentieren von Teilen dieser Arbeit.
Ein großes Danke geht auch an Katja Weise und Katrin Schönemann für das gemeinsame "Krabbeln" in der SLUB und die Pausentangos [Wei17, Sch18]. Die gegenseitige Motivation und die Diskussionen haben mir sehr geholfen den Faden beim Bearbeiten dieser Arbeit nicht zu verlieren.
Ein ganz besonderes Danke geht an Mari von der Erle, die mich über weite Strecken des Schreibens unermüdlich moralisch dabei unterstützt hat diese Arbeit zu verfassen.
Na závěr bych chtěl poděkovat svým rodičům, že mě podpořili – někdy i za nepříznivých okolností – jít touto cestou.

Eidesstattliche Versicherung

Hiermit erkläre ich an Eides statt, dass ich die vorliegende Dissertationsschrift selbst verfasst und keine anderen als die angegebenen Hilfsmittel und Quellen benutzt habe.

Die eingereichte schriftliche Fassung entspricht der auf dem elektronischen Speichermedium.

Die Dissertation wurde in der vorgelegten oder einer ähnlichen Form nicht schon einmal in einem früheren Promotionsverfahren angenommen und als ungenügend beurteilt.

(Adam Kubec)
Hamburg, den 10.11.2017